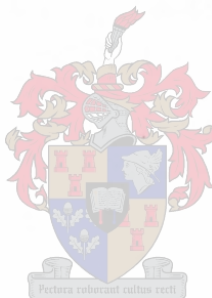


Critical evaluation of a position sensorless control technique for the reluctance synchronous machine drive

Johan L. Smuts



**Thesis presented in partial fulfilment of the requirements
for the degree of Master of Science in Electrical Engineering
at the University of Stellenbosch, South Africa**

Supervisor:

Prof. Maarten J. Kamper, University of Stellenbosch

March 2001

Declaration

I, the undersigned, hereby declare that the work contained in this thesis is my own original work and that I have not previously in its entirety or in part submitted it at any university for a degree.

Signature :

Date :

Place: Stellenbosch

Summary

The aim of this study is to critically evaluate the voltage injection position sensorless control technique as applied to the reluctance synchronous machine (RSM) drive and to implement the technique on a 5.5 kW RSM and a 110 kW RSM. The technique is evaluated by using an accurate mathematical model of the RSM in a simulation package, called Simuwin. The negative effects that cross-magnetisation and the slotted air-gap have on the technique are intensively investigated. It was showed that these effects can cause an error in the position estimation of up to 30°. The TMS320F240 DSP was used as the controller for the RSM drives to implement the position sensorless control technique. Measurements on both RSM drives confirm the simulated results.

Opsomming

Die doel van hierdie tesis is om die spannings-injeksie posisie sensorlose beheer tegniek soos toegepas op die reluktansie sinchroon masjien (RSM) aandryfstelsel, krities te evalueer en te implementeer op 'n 5.5 kW RSM en op 'n 110 kW RSM. Die tegniek is geëvalueer deur 'n akkurate wiskundige model van die RSM saam te stel en die model te gebruik in 'n simulatie pakket, genaamd Simuwin. Daar is veral klem gelê op die negatiewe invloed wat kruis-magnetisering en 'n gegleufde lug-spleet op die tegniek het. Dit is bewys dat hierdie eienskappe van die RSM 'n fout in die posisie afskatting van tot 30° kan veroorsaak. Die TMS320F240 DSP is gebruik as beheerder vir die RSM aandryfstelsels om sodoende posisie sensorlose beheer op altwee masjiene toe te pas. Metings op albei stelsels bevestig die simulaties.

Acknowledgements

I hereby thank the following people and institutes for the support in making this study possible:

- Prof. Maarten J. Kamper, my supervisor for guidance throughout the project.
- The electrical machines group for their help and friendship.
- The workshop personal for their help and friendliness.
- The FRD and The Department of Electrical Engineering at the University of Stellenbosch for their financial support.

List of Figures and Tables

Figure 1.1: Conventional (Transverse) laminated rotor.....	3
Figure 1.2: Axially laminated rotor	4
Figure 1.3: 5.5 kW RSM rotor.....	6
Figure 1.4: 110 kW RSM rotor	6
Figure 2.1: 2-pole RSM	9
Figure 2.2a: d-axis circuit model of the RSM.....	12
Figure 2.2b: q-axis circuit model of the RSM	12
Figure 2.3: Space vector diagram of the RSM.....	14
Figure 3.1: Block diagram of field orientation control of the RSM [26].....	16
Figure 3.2: Definition of vectors and angles in the RSM [6].....	19
Figure 3.3: Circuit configuration during extension of the zero crossing.	21
Figure 3.4: Induced voltage pulses in phase A	22
Figure 4.1: Block diagram of the voltage injection technique.....	26
Figure 4.2: 2-pole RSM with the synchronous rotating and high frequency voltage vectors shown	26
Figure 4.3: Coefficient ratios versus frequency of the 5.5 kW RSM	30
Figure 4.4: Coefficient ratios versus frequency of 110 kW RSM	30
Figure 4.5: Model of the RSM with L_d and L_q as constants	31
Figure 4.6: Block diagram of the voltages that supply the RSM.....	32
Figure 4.7: Phase difference between θ_h and I_{sh}^2 with $\theta_r = 0^\circ$ (5.5 kW RSM).....	33
Figure 4.8: Phase difference between θ_h and I_{sh}^2 with $\theta_r = 45^\circ$ (5.5 kW RSM).....	33
Figure 4.9: Phase difference between θ_h and I_{sh}^2 with $\theta_r = 0^\circ$ (110 kW RSM).....	34
Figure 4.10: d-axis flux-linkage versus d-axis current (5.5 kW RSM) [27].....	35
Figure 4.11: q-axis flux-linkage versus q-axis current (5.5 kW RSM) [27].....	35
Figure 4.12: Block diagram of the RSM taking saturation and cross magnetisation into account.....	36
Figure 4.13: Comparison between I_{sh}^2 and θ_h with $\theta_r = 0^\circ$ (5.5 kW RSM).....	37
Figure 4.14: Comparison between I_{sh}^2 and θ_h with $\theta_r = 90^\circ$ (5.5 kW RSM).....	37
Figure 4.15: Comparison between the effects of cross magnetisation and saturation with $I_d = 2$ A and $I_q = 3$ A (5.5 kW RSM).....	38

Figure 4.16: Comparison between the effect of cross magnetisation and saturation with $I_d = 5$ A and $I_q = 3$ A (5.5 kW RSM).....	39
Figure 4.17: Comparison between the effect of cross magnetisation and saturation with $I_d = 10$ A and $I_q = 3$ A (5.5 kW RSM).....	39
Figure 4.18: Block diagram of equations (4.18), (4.20) and (4.21)	40
Figure 4.19: I_{sh}^2 plotted to compare saturation and cross magnetisation with $I_d = 50$ A and $I_q = 50$ A.....	41
Figure 4.20: I_{sh}^2 plotted to compare saturation and cross magnetisation with $I_d = 125$ A and $I_q = 50$ A.....	41
Figure 4.21: d-axis flux-linkage versus rotor position ($I_d=9$ A; $I_q=3$ A)	42
Figure 4.22: q-axis flux linkage versus rotor position ($I_d=9$ A; $I_q=3$ A).....	42
Figure 4.23: $\frac{\partial \lambda_d}{\partial \theta}$ versus rotor position ($I_d=9$ A; $I_q=3$ A).....	43
Figure 4.24: $\frac{\partial \lambda_q}{\partial \theta}$ versus rotor position ($I_d=9$ A; $I_q=3$ A).....	44
Figure 4.25: Block diagram taking a slotted air-gap into account	44
Figure 4.26: Comparing I_{sh}^2 for a slotted and smooth air-gap with $\theta = 0^\circ$	45
Figure 4.27: Comparing I_{sh}^2 for a slotted and smooth air-gap with $\theta = 10^\circ$	45
Figure 4.28: Comparing I_{sh}^2 for a slotted and non-slotted air-gap with $\theta = 20^\circ$	46
Figure 5.1: System Block diagram.....	47
Figure 5.2: 110 kW RSM experimental set-up	48
Figure 5.3: 5.5 kW RSM (left front)	48
Figure 5.4: Block diagram of the current measurement.....	49
Figure 5.5: Block diagram of the Position Estimator.	50
Figure 5.7: Circuit diagram for determining $i_{\alpha h}$ and $i_{\beta h}$	52
Figure 5.8: Circuit diagram for determining I_{sh}^2	52
Figure 5.9: DSP Controller Block diagram.....	53
Figure 5.10: Memory Map	54
Figure 5.11: Block diagram of the Constant current angle controller.	55
Figure 5.12: Block diagram of constant d-axis current control.	56
Figure 5.13: Simulation block diagram of the inverter.....	57
Figure 5.14: Simulation done with a 60 μ s sample period.	57

Figure 5.15: Simulation done with a 200 μ s sample period.	58
Figure 5.16: Block diagram of the protection interface	58
Table 6.1: Measured torque, with constant d-axis current control.....	60
Table 6.2: Measured torque with constant current angle control.....	60
Figure 6.1a: Measured torque with constant current angle control.....	61
Figure 6.1b: Measured torque with constant d-axis current control	61
Figure 6.2: Resolver and estimated position of the 5.5 kW RSM accelerating from standstill.....	62
Figure 6.3: Estimated and resolver's position with $I_d = 1$ A.....	63
Figure 6.4: Estimated and resolver's position with $I_d = 3$ A.....	63
Figure 6.5: Estimated and resolver position with $I_d = 7$ A and I_q low	64
Figure 6.6 : Constant d-axis current control ($\theta_{estimated}$ and i_a are shown). The grid intervals for the current signal is 2 A/div	65
Figure 6.7 : Constant current angle control ($\theta_{estimated}$ and i_a are shown)). The grid intervals for the current signal is 0.5 A/div	65
Figure 6.8 : The estimated and resolver positions with position sensorless constant current angle control of the 110 kW RSM	66

List of major symbols

L_d, L_q	d-axis and q-axis inductances, H
θ, θ_r	angle between the rotor's q-axis and the phase A magnetic axis, rad
θ_h	angle between the high frequency voltage vector and the phase A magnetic axis, rad
$\overline{\lambda_l}$	stator leakage flux-linkage vector, Wb-turn \angle rad
$\overline{\lambda_m}$	air-gap flux-linkage vector, Wb-turn \angle rad
$\overline{\lambda_s}$	stator flux-linkage vector, Wb-turn \angle rad
λ_d, λ_q	d-axis and q-axis flux-linkages, Wb-turn
$\overline{v_s}$	stator voltage vector, V \angle rad
v_a, v_b, v_c	stator phase voltages, V
v_d, v_q	d-axis and q-axis voltages, V
$\overline{v_{sh}}$	high frequency voltage vector, V \angle rad
v_{ah}, v_{bh}, v_{ch}	phase voltages of the high frequency voltage vector, V
v_{dh}, v_{qh}	d-axis and q-axis voltages of the high frequency voltages vector, V
$\overline{i_s}$	current vector, A \angle rad
i_a, i_b, i_c	phase currents, A
i_d, i_q	d-axis and q-axis currents, A
$\overline{i_{sh}}$	high frequency current vector, A \angle rad
i_{ah}, i_{bh}, i_{ch}	phase currents of the high frequency current vector, A
i_{dh}, i_{qh}	d-axis and q-axis currents of the high frequency current vector, A
r_s	stator resistance, Ω
ω	electrical angular velocity, rad.s ⁻¹
ω_m	mechanical speed, rad.s ⁻¹
P	power, kW
T	torque, N-m
ϕ	current angle (angle between d-axis and current vector), rad
i_α, i_β	alfa and beta components of the current vector, A

List of major abbreviations

ac	alternating current
dc	direct current
kVA	kilo volt ampere
kW	kilowatt
PM	permanent magnet
IM	induction machine
RSM	reluctance synchronous machine
VSI	voltage source inverter
FEM	finite element method
MMF	magnetomotive force
PWM	pulse width modulation
CRPWM	current regulated pulse width modulation
DSP	digital signal processor
DAC	digital to analogue converter
EPLD	erasable programmable logic device
IC	integrated circuit
ADC	analogue to digital converter
IGBT	isolated gate bipolar transistor
ZOH	zero order hold

Contents

List of Figures and Tables	vi
List of major symbols	ix
List of major abbreviations.....	x
1 Introduction	1
1.1 Different RSM rotor structures	3
1.2 Problem statement.....	4
1.3 Approach to problem	5
1.4 Layout of the thesis.....	7
2 Mathematical model of the RSM	8
2.1 Transforming the abc-variables of RSM into dq0 variables [3]	10
2.2 Electromagnetic torque production [1]	14
3 Various techniques of position sensorless control.....	16
3.1 Current Angle Calculation of the RSM	17
3.1.1 Derivation of the current angle [6].....	18
3.1.2 Comments on the current-angle-calculation technique.....	20
3.2 Modifying the PWM switching strategy.....	20
3.2.1 Comments on this modified-PWM technique on a RSM drive	22
3.3 Sensorless control technique using induced third harmonic voltage.....	23
3.3.1 Comments on the induced third harmonic voltage technique.....	24
4 Voltage Injection Position Sensorless Control Technique.....	25
4.1 Explanation of the voltage injection technique.....	25
4.2 Simulations of the voltage injection method	31
4.2.1 Simulations with L_d and L_q as constants.....	31
4.2.2 Simulations taking into account saturation and cross magnetisation.....	34
4.2.3 Simulations taking into account the slotted air-gap	42
4.3 Summary	46

5	Implementation of the Voltage Injection Technique.	47
5.1	Current Measurement and Position Estimation	49
5.1.1	Current Measurement.....	49
5.1.2	Position Estimation	50
a)	Bandpass (BP) Filter.....	51
b)	Determine the I_{sh}^2 -signal.....	52
5.2	DSP Control Card	53
5.2.1	Resolver circuitry	53
5.2.2	Programming the DSP	54
5.2.3	DACs, ADC and the PWM output.....	54
5.2.4	Control strategies	55
5.2.5	Synchronous sampling	56
5.3	Protection Interface Card	58
6	Practical evaluation of the voltage injection position sensorless control technique.....	59
6.1	Practical evaluation on the 5.5 kW RSM drive	59
6.1.1	Standstill tests	60
6.1.2	Acceleration from standstill	62
6.1.3	The effect of cross magnetisation	62
6.1.4	The effect of a slotted air-gap	64
6.1.5	Position sensorless control using two different control strategies	65
6.2	Practical evaluation of the 110 kW RSM drive	66
7	Conclusions and recommendations	67
7.1	Conclusions.....	67
7.2	Recommendations.....	68
8	References	69

Chapter 1

1 Introduction

At present there is still a need for new and better electrical machine configurations, with low rotor losses, relative cheap in price and with higher efficiency. A lot of research and development were done in the past few decades in the sought for better electrical machines and electrical machine drives.

Brushless permanent magnet electrical machines were developed over the last 2 decades for variable speed drive applications. Permanent magnets, with very high energy densities ($\sim 35 \text{ J/cm}^3$), were produced and used in these brushless machines to obtain very high torque-densities, low loss/torque and high kW/kVA ratios. However permanent magnet machines have their disadvantages, like demagnetisation of the magnets, limited operating temperatures and the high cost of the magnets.

Although the induction machine drive is widely used it also has its disadvantages. Vector control of induction machines has fast speed dynamics therefore it is used for variable speed applications. The induction machine, as an ac machine, is relative cheap, but it requires a more complex control strategy that is also much more parameter dependent. Also where a large torque at low speeds is required, the induction machine's rotor causes a cooling problem because of the large rotor losses.

The search for a low cost, rugged and low rotor loss machine led to the development of the switched reluctance machine, which compared very good with the vector controlled induction machine. However, this machine also has a lot of disadvantages like, torque pulsations, acoustic noise and low kW/kVA ratios. The performance of these machines was improved with the addition of permanent magnets on the rotor and by bipolar multiphase control, but it didn't surpass the PM brushless machine.

So the need for better line-started and inverter-fed machines is still there. The goals to meet are:

- high torque density

- low torque ripple and noise
- low loss/torque
- high kW/kVA
- fast torque and speed dynamics
- wide speed range
- efficient field weakening (constant power)
- rugged and cheap
- controller simplicity

The Reluctance Synchronous Machine (RSM) has a good torque-density and efficiency, a simple vector control strategy and low manufacturing cost. Therefore, the RSM is a very good contestant in meeting the above mentioned goals. World wide there is a renewal interest in the design and performance of this machine, especially in comparison with the workhorse of the industry, the induction machine.

Comparative studies between the IM and RSM have been done and gave the following results:

- In [15] it is showed that the torque of the RSM is higher than the IM if it is designed for the same copper losses – these machines were below 1kW. With the use of a standard 5.5kW IM stator frame, and a RSM rotor, [13] and [14] showed that the torque of the RSM is the same as with the IM rotor. However, the RSM stator currents are 1.2 times that of the IM with the total copper losses 30% less than the IM. This RSM rotor was not optimised in the design.
- A fully (rotor and stator) optimised RSM was designed by Kamper [16]. The outer diameter and the copper losses, the same as for a standard 5.5 kW IM, was taken as parameters in the design. The Finite Element Method (FEM) was used to optimise the design of the stator and the rotor. It was found that at rated speed of 1500 rpm the RSM delivers 9 kW continuous power, compared to the 5.5 kW continuous power of the IM.

- A very good comparative study between the RSM and the IM was done by JJ Germishuysen [1]. A 110 kW IM was used, and for the RSM the IM's rotor was removed and replaced by an optimum designed RSM rotor. The same inverter was used for both the IM and the RSM, and a 600 kW dynamometer was used as load. It was proved that the torque of the RSM compares very well with the IM up to rated speed (1500 rpm). The efficiency of the RSM is even better than the IM up to a speed of 2500 rpm. The only drawback was the low power factor. It must further be mentioned that the stator of the RSM was not optimised. It would in fact be a very interesting experiment to do the same comparative tests with an optimum designed RSM stator and rotor.

1.1 Different RSM rotor structures

Lawrenson in the UK and Honsinger in the USA developed, in the 1960's, RSMs that were comparable to the same performance level as the IM. A big drawback of these machines, was their relative low specific torque production when line-started or controlled open loop. To overcome this problem the saliency (ratio of L_d over L_q) must be maximised and closed loop inverter fed vector control must be applied to these machines. The conventional laminated rotors (Figure 1.1) have medium saliencies ($L_d/L_q \approx 7$). To improve the L_d/L_q ratio the axially laminated rotor (Figure 1.2) was developed. As shown in the picture, laminations are bent into U or V shapes and packed onto the rotor, with insulation material between these laminations. With this configuration very good L_d/L_q ratios of up to 16 were obtained. However, the axially laminated rotor is expensive to manufacture. The conventional laminated rotor structure was used in this study, because it is not so expensive and its saliency is not to low.

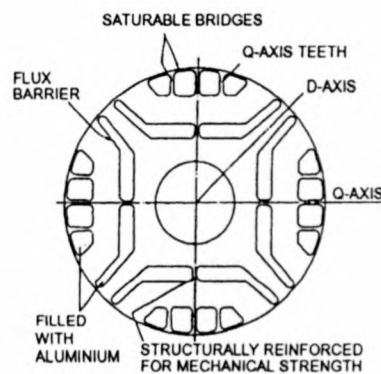


Figure 1.1: Conventional (Transverse) laminated rotor

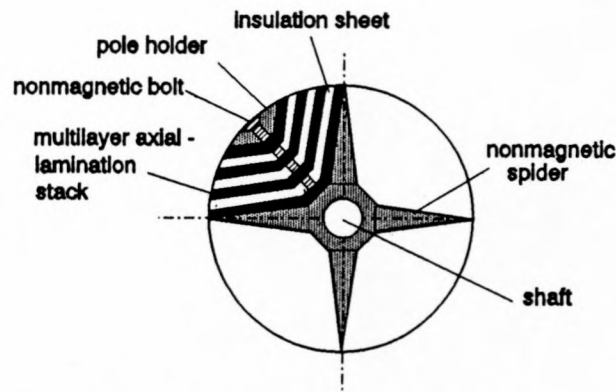


Figure 1.2: Axially laminated rotor

1.2 Problem statement

In the past dc electrical machines were almost the only machines used for variable speed drive operation. Because ac machines, such as the IM and the RSM, are much cheaper, more reliable and almost maintenance free, there is a need for variable speed drives using these machines. Power electronic converters also become cheaper, and that makes the ac machine drive a very competitive contestant to the conventional dc machine drive. For a synchronous machine like the RSM, the current and rotor position are measured and fed back to the controller in a closed-loop drive system. This ensures that the amplitude and the angle, with respect to the rotor, of the current vector are controlled, from there the term '**vector control**'. Thus, to implement vector control, the position of the rotor is needed. This means that a position sensor such as a resolver must be mounted on the machine for position feedback. The resolver and its circuitry is expensive, so there is a definite need to control the RSM without a position sensor.

Quite a lot of research [4]-[11] has been done on position sensorless control of the RSM, but all with limited success. Most of the techniques used gave good results at non-zero speeds, but there is still a problem in estimating the position of the rotor at standstill and very low speeds. Therefore, a position sensorless control technique for controlling the RSM at zero and low speeds is investigated and implemented.

1.3 Approach to problem

The RSM's rotor is a salient pole rotor, which means that the L_d and L_q inductances have different values. The FEM is used to calculate the values of L_d and L_q as functions of the d- and q-axis currents of the machine. These data is used to compose mathematical models of the RSM that take the effects of saturation, cross-magnetisation and a slotted air-gap into account. With the use of these mathematical models simulations are done to investigate a position sensorless control technique, namely the high frequency voltage injection technique. This technique consists of applying high frequency voltage signals to the stator of the RSM, and by measuring the high frequency currents, the position of the rotor can be estimated.

The technique is implemented on two different RSM drives to evaluate the proposed method and to see if there is a correlation between the measured and simulated results.

The first machine is the 5.5 kW RSM rotor that was inserted into a standard 5.5 kW IM stator frame. The rotor was designed by A Mackay [13]. The rotor is unskewed and is not optimum designed. Because of the slotted air-gap and the unskewed rotor this RSM has a high flux-linkage ripple. This feature of the machine is investigated to see what effect it has on the rotor position estimation.

The second machine is a 110 kW RSM designed by JJ Germishuysen [1]. This machine's rotor is indeed optimised in its design, but the stator is that of a conventional 110 kW IM. This RSM was designed for traction applications.

Figures 1.3 and 1.4 show the laminations of each machine. The scaling of the two pictures are the same and are half the real size of the rotors.

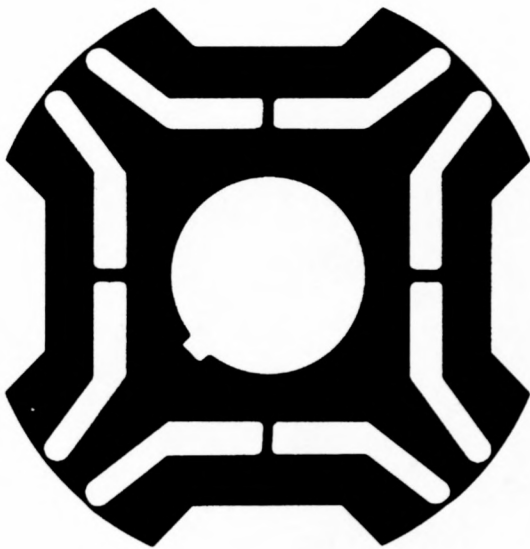


Figure 1.3: 5.5 kW RSM rotor.

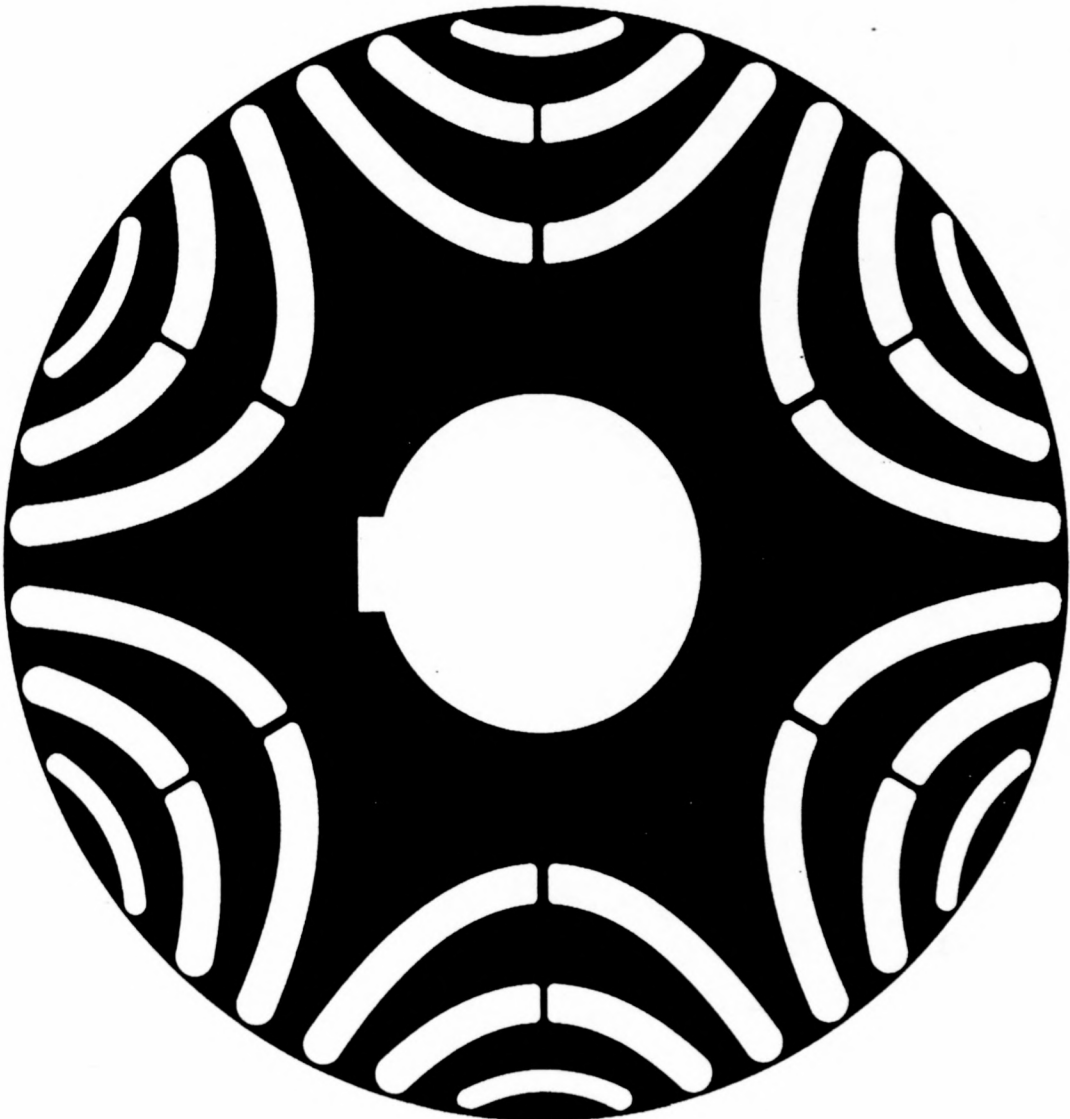


Figure 1.4: 110 kW RSM rotor

1.4 Layout of the thesis

The layout of the remainder of this thesis can be summarised as follows:

- Chapter 2: The mathematical model of the RSM, in dq values, is derived, with the use of the Park transformation. Calculations for power and produced torque are also discussed.
- Chapter 3: Three different position sensorless control techniques of the RSM is investigated, looking at the advantages and the disadvantages of each of these techniques.
- Chapter 4: The mathematical model of the RSM is expanded to take the effects of cross magnetisation and the slotted air-gap into account. Simulations are done to investigate the influence of these effects on the position estimation.
- Chapter 5: All the hardware, like the DSP controller, position estimation card and the inverters, that were used to implement the position sensorless control technique, are discussed in detail.
- Chapter 6: The technique is evaluated in this chapter by showing measured results of the estimated and actual rotor position.
- Chapter 7: In this chapter conclusions are given and recommendations are made for further research.

Chapter 2

2 Mathematical model of the RSM

The RSM has a standard, non-salient stator with three-phase windings and an unexcited rotor with magnetic asymmetry. There are no field nor cage windings on the rotor. Thus, the only circuits that have to be considered in the analysis of the RSM are the three stator phase windings. Each of these phase circuits has its own resistance, self-inductance and mutual inductances with respect to the other phase circuits. This means that the analysis of such a machine can be done with the solution of a set of simultaneous differential voltage equations. This is easier said than done, because a set of three differential voltage equations has to be solved of which the self- and mutual inductances change with rotor position. To make the solution easier, a linear transformation, known as the dq0 transformation, of all the variables are done. With this transformation the instantaneous stator currents, stator voltages and stator fluxes are transformed into variables that are referenced to the rotor, meaning that these variables become dc quantities in the steady state. These transformed variables are the variables of dq electrical circuits that rotate synchronously with the rotor. For example, the stator currents i_a , i_b and i_c are transformed into *direct-axis current* i_d and *quadrature-axis current* i_q and the *zero-sequence current* i_0 . This transformation ensures a set of only two simultaneous differential voltage equations with inductances that are constant. The transformation is a very straightforward calculation, involving only the quantities to be transformed and the electrical angle θ , that is the angle between the rotor q-axis and the stator phase-a magnetic axis as shown in Figure 2.1.

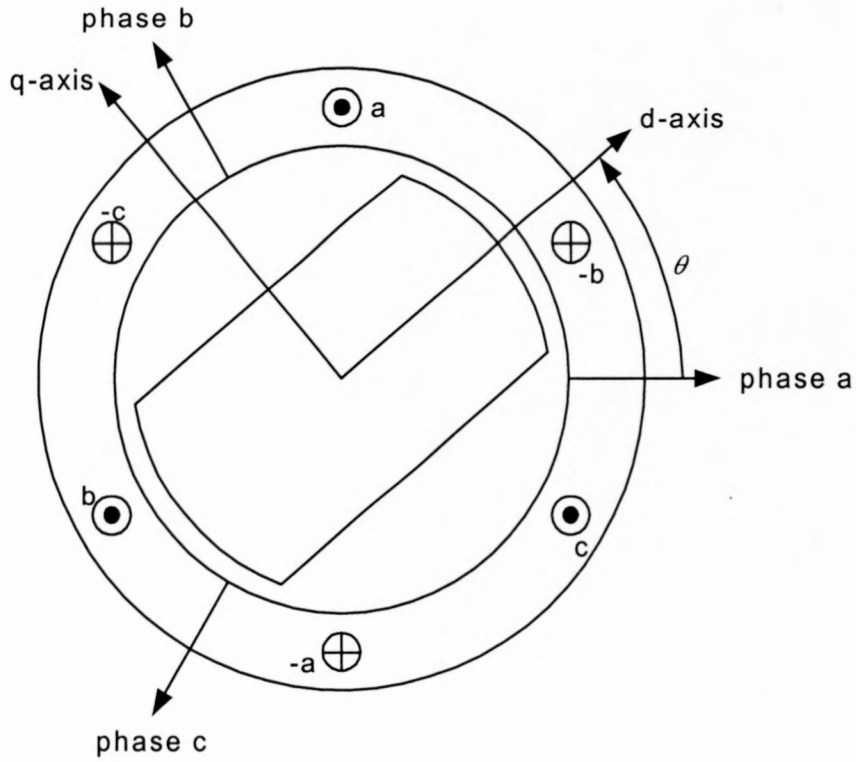


Figure 2.1: 2-pole RSM

The dq0 transformation (or Park transformation) given in matrix format is [3]

$$\begin{bmatrix} S_d \\ S_q \\ S_0 \end{bmatrix} = \frac{2}{3} \begin{bmatrix} \cos \theta & \cos(\theta - 120^\circ) & \cos(\theta + 120^\circ) \\ \sin \theta & \sin(\theta - 120^\circ) & \sin(\theta + 120^\circ) \\ \frac{1}{2} & \frac{1}{2} & \frac{1}{2} \end{bmatrix} \begin{bmatrix} S_a \\ S_b \\ S_c \end{bmatrix} \quad (2.1)$$

where S_a , S_b and S_c represent stator quantities and S_d , S_q and S_0 are the transformed quantities revolving at rotor speed.

The inverse transformation given in matrix format is

$$\begin{bmatrix} S_a \\ S_b \\ S_c \end{bmatrix} = \begin{bmatrix} \cos \theta & \sin \theta & 1 \\ \cos(\theta - 120^\circ) & \sin(\theta - 120^\circ) & 1 \\ \cos(\theta + 120^\circ) & \sin(\theta + 120^\circ) & 1 \end{bmatrix} \begin{bmatrix} S_d \\ S_q \\ S_0 \end{bmatrix}. \quad (2.2)$$

2.1 Transforming the abc-variables of RSM into dq0 variables [3]

The following flux-linkage equations are that of a synchronous machine, but with the field current taken as zero, as for the RSM. The flux-current equations in phase variables are

$$\begin{bmatrix} \lambda_a \\ \lambda_b \\ \lambda_c \end{bmatrix} = \begin{bmatrix} L_{aa} & L_{ab} & L_{ac} \\ L_{ba} & L_{bb} & L_{bc} \\ L_{ca} & L_{cb} & L_{cc} \end{bmatrix} \begin{bmatrix} i_a \\ i_b \\ i_c \end{bmatrix}. \quad (2.3)$$

For the purpose of this analysis two assumptions are made:

- 1) The air-gap permeance has a constant component, and a smaller component that varies cosinusoidally with the rotor angle measured from the d-axis.
- 2) The effect of space harmonics in the air-gap flux is ignored.

With these assumptions, dq0 machine analysis can be done with excellent results in a wide range of applications.

The machine phase inductances can be written in terms of the electrical angle, θ , because of assumption one made above. For the stator self-inductances

$$L_{aa} = L_{ls} + L_A - L_B \cos 2\theta, \quad (2.4)$$

$$L_{bb} = L_{ls} + L_A - L_B \cos(2\theta + 120^\circ), \quad (2.5)$$

$$L_{cc} = L_{ls} + L_A - L_B \cos(2\theta - 120^\circ), \quad (2.6)$$

and for the stator-stator mutual inductances

$$L_{ab} = L_{ba} = -\frac{1}{2}L_A - L_B \cos(2\theta - 120^\circ), \quad (2.7)$$

$$L_{ac} = L_{ca} = -\frac{1}{2}L_A - L_B \cos(2\theta + 120^\circ), \quad (2.8)$$

$$L_{bc} = L_{cb} = -\frac{1}{2}L_A - L_B \cos 2\theta \quad (2.9)$$

where L_A is the component of self inductance due to the space-fundamental air-gap flux, L_{ls} is the additional component due to the stator leakage flux and L_B is the coefficient of the cosinusoidal component, that is mentioned in assumption (1).

According to equations (2.4)-(2.9) the effect of saliency can be seen in the self- and mutual inductance terms and it is dependent on 2θ (two times the electrical angle). If one looks at the geometry of a 2 pole RSM (Figure 2.1) it is quite obvious to see this relationship as the second 180° is a mirror image of the first 180° , from there the 2θ term.

The flux-linkage equations (2.3) can be simplified by applying the dq0 transformation. Applying the dq0 transformation to both the flux-linkages and the currents of equation (2.3), zero-sequence components appear. However, because only balanced 3-phase systems are considered, these components are zero. After some mathematical manipulations the results are

$$\lambda_d = L_d i_d \quad (2.10)$$

$$\text{and} \quad \lambda_q = L_q i_q \quad (2.11)$$

where

$$L_d = L_{ls} + \frac{3}{2}(L_A + L_B) \quad (2.12)$$

$$\text{and} \quad L_q = L_{ls} + \frac{3}{2}(L_A - L_B) . \quad (2.13)$$

The quantities L_d and L_q are the *direct-axis* and *quadrature-axis inductances*, respectively. Notice that the flux-current equations (2.10) and (2.11) no longer contain inductances that are functions of the rotor position as was the case for the inductances in equations (2.4)-(2.9). This shows how useful the dq0 transformation actually is.

Considering the voltage equations of the RSM in the abc co-ordinate system

$$v_a = r_s i_a + \frac{d\lambda_a}{dt}, \quad (2.14)$$

$$v_b = r_s i_b + \frac{d\lambda_b}{dt} \quad (2.15)$$

$$\text{and } v_c = r_s i_c + \frac{d\lambda_c}{dt}. \quad (2.16)$$

After the dq0 transformation

$$v_d = r_s i_d + \frac{d\lambda_d}{dt} - \omega \lambda_q \quad (2.17)$$

$$\text{and } v_q = r_s i_q + \frac{d\lambda_q}{dt} + \omega \lambda_d \quad (2.18)$$

where $\omega = \frac{d\theta}{dt}$ [3].

With these equations, the analysis of the RSM can be done. In the steady state the values of the dq variables are dc quantities. Figures 2.2a and 2.2b show the electric circuit model of the RSM as defined by equations (2.17) and (2.18).

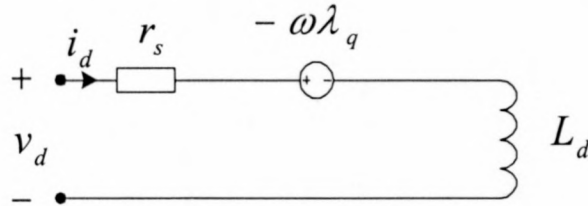


Figure 2.2a: d-axis circuit model of the RSM

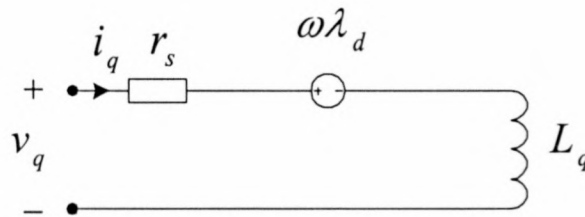


Figure 2.2b: q-axis circuit model of the RSM

To conclude the mathematical model of the RSM, equations for power and torque are needed. In phase quantities the instantaneous power is given by

$$P_s = v_a i_a + v_b i_b + v_c i_c. \quad (2.19)$$

To calculate the instantaneous power in the dq0 reference frame, Figures 2.2a and 2.2b can be used. The developed power of the d-axis circuit (Figure 2.2a) is calculated by multiplying the current, i_d , with the voltage source, $-\omega \lambda_q$. The same is done to calculate the developed power of the q-axis circuit. Therefore

$$P_d = \frac{3}{2} (-i_d \omega \lambda_q + i_q \omega \lambda_d). \quad (2.20)$$

To calculate the developed torque use

$$P_d = \omega_m T_d, \quad (2.21)$$

where ω_m is the mechanical speed of the rotor in rad/s. The relationship between the electrical speed and the mechanical speed is

$$\omega_m = \frac{\omega}{(\text{poles} / 2)} \quad (2.22)$$

where ω is the electrical speed. By substituting equations (2.21) and (2.22) into equation (2.20), [3]

$$T = \frac{3}{2} \frac{\text{poles}}{2} (\lambda_d i_q - \lambda_q i_d). \quad (2.23)$$

Note that this torque equation assumes that with constant current there is no variation of the d- and q-axis flux linkages with rotor position.

2.2 Electromagnetic torque production [1]

When the RSM rotor is unaligned with the stator MMF wave, the rotor will experience a reluctance torque in the direction to align the rotor's d-axis with the resultant MMF wave. The rotor wants to align with the stator MMF to maximise the magnetic stored energy, or else to minimise the reluctance of the magnetic circuit. This minimum reluctance flux path is through the d-axis. The current space vector angle ϕ , shown in Figure 2.3, is the angle through which the rotor has to move to achieve a minimum reluctance flux path.

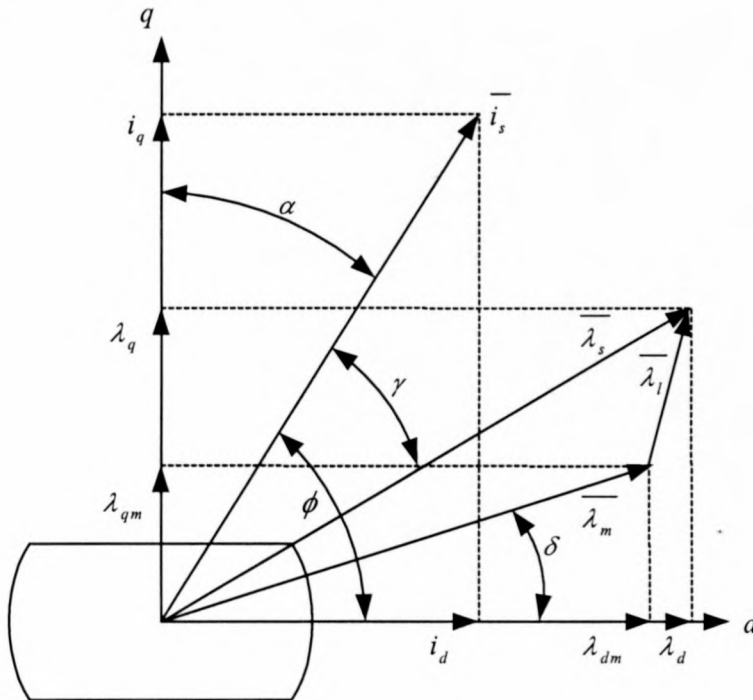


Figure 2.3: Space vector diagram of the RSM

To implement vector control on the RSM, the current angle ϕ has to be controlled in order to control the torque. To generate maximum torque/ampere, this angle has to be theoretical 45° . However, because of saturation and cross magnetisation this angle was found to be round about 65° for transverse laminated rotor RSMs. The angles γ and δ in Figure 2.3 are the torque angle and the air-gap flux linkage space vector angle respectively. The angle α is the angle between the q-axis and the current space vector \bar{i}_s . The stator flux linkage vector, $\bar{\lambda}_s$, is the vector sum of the air-gap flux-linkage vector, $\bar{\lambda}_m$, and the stator leakage flux linkage vector, $\bar{\lambda}_l$.

The torque of the RSM is given by equation (2.23), but can also be determined using the fundamental current and the flux linkage space vectors. The magnitude of the torque produced by the machine is proportional to the cross product between $\overline{\lambda_s}$ and $\overline{i_s}$. Therefore

$$T = \left\| k \overline{\lambda_s} \times \overline{i_s} \right\| \text{ (also given by [4])}$$

where k is a constant. If the cross product between the air-gap flux vector, $\overline{\lambda_m}$, and the current vector, $\overline{i_s}$, is calculated, it gives the same result. This is because the torque is independent of the leakage flux.

Chapter 3

3 Various techniques of position sensorless control.

The RSM can be ensured to operate at maximum torque per ampere if it is controlled by the field orientation method. To implement this method the stator voltage vector has to be synchronised with the rotor, therefore the precise position of the rotor is needed. Position sensors like absolute encoders and resolvers can be used for this. These sensors, however, are relative expensive and fragile or unreliable, and can prevent this motor being used in a hostile environment. Several techniques for controlling the RSM without a sensor are proposed in the literature and some of these is discussed in this chapter. Figure 3.1 shows a block diagram of an inverter-fed RSM controller with position feedback.

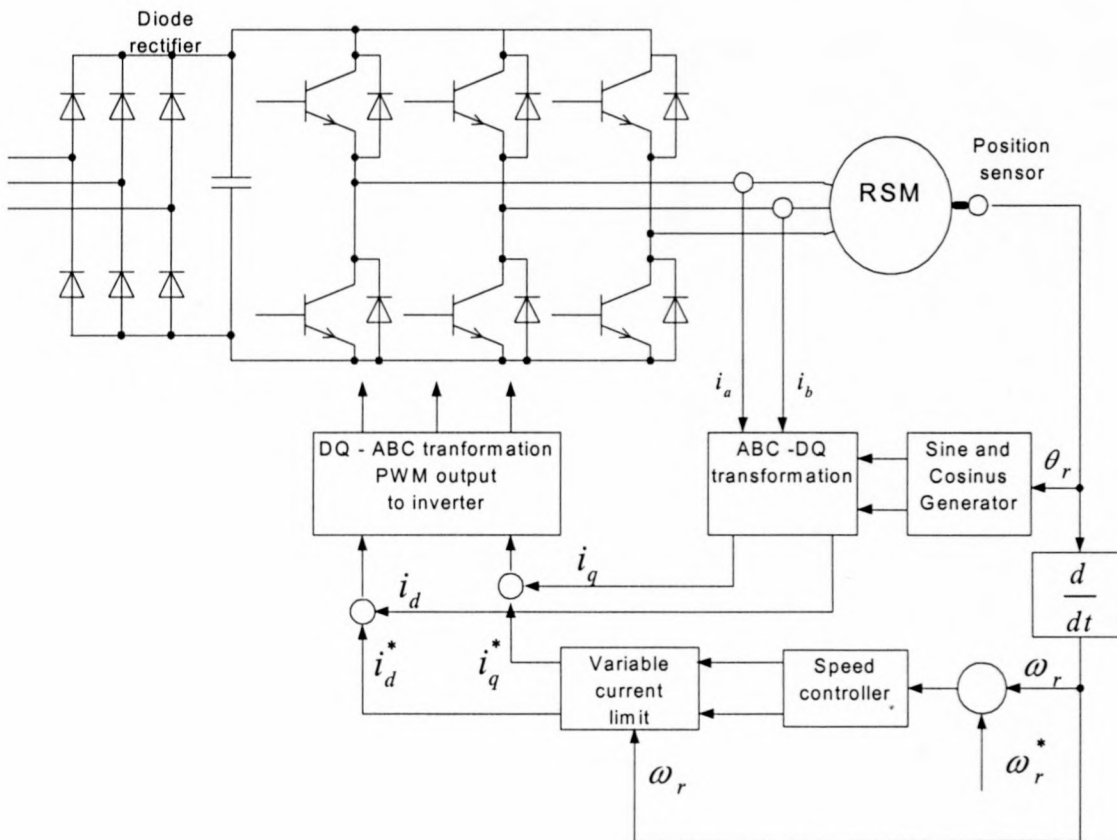


Figure 3.1: Block diagram of field orientation control of the RSM [26].

The techniques for estimating the rotor position can be divided into three categories:

- No additional signal needed
- Introducing modification of the PWM strategy
- The injection of additional high frequency signals in the control loop

The implementation and evaluation of the injection technique is the focus of this thesis and is therefore not discussed in this chapter, but separately in Chapters 4-6. A few variations of the first two techniques will be investigated and discussed in this chapter.

3.1 Current Angle Calculation of the RSM

The current-angle-calculation position sensorless control technique was implemented by S. Bolognani [6]. The technique is based on the direct control of the current angle, that is the angle between the current vector and the rotor's d-axis (see Figure 3.2). The current angle is calculated on-line, using the motor's dynamic voltage equations.

The machine current, the modulus and the angle are the two variables that are controlled. The d-axis current is kept constant, while the q-axis current determines the torque command. This means that for a specific torque command the current references i_d and i_q are known. Hence, the current angle reference can be calculated. The current angle reference is compared with the estimated current angle, based on voltage and current measurements. From this the error between the desired current angle and the estimated current angle is calculated. The measured currents are transformed to the dq0 reference frame and are then compared with the desired i_d and i_q current references. From this the error between the amplitude of the desired and measured currents is calculated. The amplitude and angle errors are transformed to the abc reference frame and are then fed to the voltage source inverter (VSI), which feeds the RSM.

3.1.1 Derivation of the current angle [6]

According to Equations (2.17) and (2.18), the voltage equations of the RSM in the dq reference frame are

$$v_d = r_s i_d + \frac{d\lambda_d}{dt} - \omega_m \lambda_q \quad (3.1)$$

$$\text{and} \quad v_q = r_s i_q + \frac{d\lambda_q}{dt} + \omega_m \lambda_d \quad (3.2)$$

where $\omega_m = \omega - \frac{d\phi}{dt}$ (see Figure 3.2).

Because of cross-magnetisation, where $\lambda_d = f(i_d, i_q)$ and $\lambda_q = f(i_q, i_d)$, equations (3.1) and (3.2) become

$$v_d = r_s i_d + \frac{\partial \lambda_d}{\partial i_d} \frac{di_d}{dt} + \frac{\partial \lambda_d}{\partial i_q} \frac{di_q}{dt} - \omega_m \lambda_q \quad (3.3)$$

$$v_q = r_s i_q + \frac{\partial \lambda_q}{\partial i_q} \frac{di_q}{dt} + \frac{\partial \lambda_q}{\partial i_d} \frac{di_d}{dt} + \omega_m \lambda_d. \quad (3.4)$$

Defining the differential inductances as follows:

$$L_d^\partial(i_d, i_q) = \frac{\partial \lambda_d}{\partial i_d} \quad (i_q = \text{constant}) \quad (3.5)$$

$$L_q^\partial(i_d, i_q) = \frac{\partial \lambda_q}{\partial i_q} \quad (i_d = \text{constant}) \quad (3.6)$$

$$M_{dq}^\partial(i_d, i_q) = \frac{\partial \lambda_q}{\partial i_d} = \frac{\partial \lambda_d}{\partial i_q} \quad (3.7)$$

Substituting equations (3.5)-(3.7) and equations (2.10) and (2.11) into equations (3.3) and (3.4), the voltage equations become

$$v_d = r_s i_d + L_d^\partial \frac{di_d}{dt} + M_{dq}^\partial \frac{di_q}{dt} - \omega_m L_q i_q \quad (3.8)$$

$$\text{and} \quad v_q = r_s i_q + L_q^{\partial} \frac{di_q}{dt} + M_{dq}^{\partial} \frac{di_d}{dt} + \omega_m L_d i_d. \quad (3.9)$$

With referring to Figure 3.2 the d and q-axis voltage and currents are given as

$$v_d = |\bar{v}| \cos(\phi + \alpha) \quad (3.10)$$

$$\text{and} \quad v_q = |\bar{v}| \sin(\phi + \alpha) \quad (3.11)$$

$$\text{and} \quad i_d = |\bar{i}| \sin \phi \quad (3.12)$$

$$\text{and} \quad i_q = |\bar{i}| \cos \phi. \quad (3.13)$$

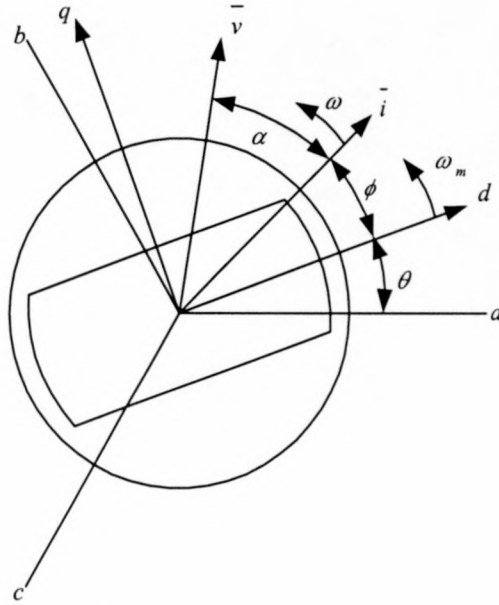


Figure 3.2: Definition of vectors and angles in the RSM [6]

By substituting equations (3.10)-(3.13) into (3.8) and (3.9) two equations for calculating the current angle is generated. Any one of these can be used [6],

$$\tan \phi = \frac{v \cos \alpha - r_s i - L_d^{\partial} \frac{di}{dt} - M_{dq}^{\partial} i \frac{d\phi}{dt}}{v \sin \alpha - \omega_m L_q i + M_{dq}^{\partial} \frac{di}{dt} - L_d^{\partial} i \frac{d\phi}{dt}} \quad (3.14)$$

$$\text{or } \tan \phi = \frac{-v \sin \alpha + \omega_m L_d i + M_{dq}^{\partial} \frac{di}{dt} + L_q^{\partial} i \frac{d\phi}{dt}}{v \cos \alpha - r_s i - L_q^{\partial} \frac{di}{dt} + M_{dq}^{\partial} i \frac{d\phi}{dt}} \quad (3.15)$$

where $v = |\vec{v}|$ and $i = |\vec{i}|$.

These equations can be simplified if the motor dynamics are slow (therefore $\omega = \omega_m$), without significant errors. Equations (3.14) and (3.15) reduce then to [6]:

$$\tan \phi = \frac{v \cos \alpha - r_s i}{v \sin \alpha - \omega L_q i} \quad (3.16)$$

$$\tan \phi = \frac{-v \sin \alpha + \omega L_d i}{v \cos \alpha - r_s i} \quad (3.17)$$

3.1.2 Comments on the current-angle-calculation technique

In [6], a sensitivity study of this technique was done and it was found that the accuracy of the algorithm decreases as the speed decreases. Therefore this technique is not suitable for very low speed operation. The calculation of the current angle is also dependent on the values of L_d and L_q , which means that saturation and cross magnetisation will influence the accuracy of the estimated angle. Further is this technique also temperature dependent.

3.2 Modifying the PWM switching strategy

This technique, hereafter called the “modified PWM” position sensorless control technique, was proposed by MS Arefeen, M Ehsani and TA Lipo [7]. The technique determines the position of the rotor only at the zero crossing of the phase currents. The position between these zero crossings is estimated by applying extrapolation.

The rotor position information, embedded in the RSM’s mutual inductance equations (3.18)-(3.20), is obtained by employing a special switching technique. The mutual inductances of the RSM is given by

$$L_{ab} = L_{ba} = -\frac{1}{2} L_A - L_B \cos(2\theta - \frac{2\pi}{3}), \quad (3.18)$$

$$L_{ac} = L_{ca} = -\frac{1}{2}L_A - L_B \cos(2\theta + \frac{2\pi}{3}) \quad (3.19)$$

$$\text{and } L_{bc} = L_{cb} = -\frac{1}{2}L_A - L_B \cos 2\theta. \quad (3.20)$$

In the implementation of the modified-PWM technique, [7] uses the standard current regulated PWM control for the drive. With this strategy the individual switches are turned on or off in order to follow the desired reference. With the modified PWM switching technique, both switches of a phase are turned off when that phase current is going through zero. The other two phases are excited in series by turning on alternate pairs of switches.

Figure 3.3 shows an example of the case where the current in phase A goes through zero and both switches are opened. The top switch of phase B and the bottom switch of phase C are closed. The zero crossing of phase A will be extended for a short interval and a constant current reference will be applied to phases B and C. Although the current in phase A will be zero, a voltage will be induced in phase A because of the current flowing in phases B and C.

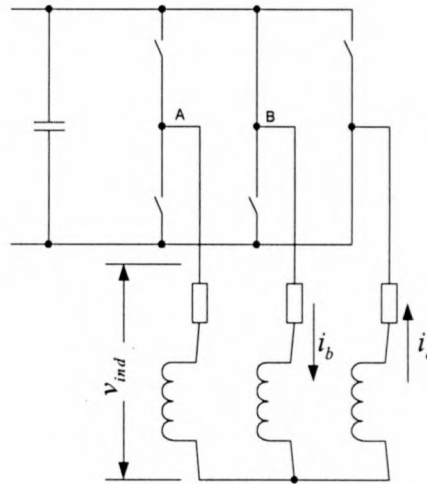


Figure 3.3: Circuit configuration during extension of the zero crossing.

From equation (2.14) with $i_a = 0$, the induced voltage are given by

$$v_{ind} = \frac{d}{dt}(L_{ab}i_b + L_{ac}i_c). \quad (3.21)$$

Because phases B and C are effectively in series

$$i_b = -i_c \quad \text{and} \quad \frac{di_b}{dt} = -\frac{di_c}{dt}. \quad (3.22)$$

Equation (3.21) thus becomes

$$v_{ind} = (L_{ab} - L_{ac}) \frac{di_b}{dt} + i_b \frac{d(L_{ab} - L_{ac})}{dt}. \quad (3.23)$$

Using equations (3.18) and (3.19) the induced voltage can be written as [7]

$$v_{ind} = K_1 \sin(2\theta_r) + K_2 \cos(2\theta_r) \quad (3.24)$$

where

$$K_1 = -(2L_B \sin \frac{2\pi}{3}) \frac{di_b}{dt} \quad (3.25)$$

$$\text{and} \quad K_2 = (4L_B \omega_r \sin \frac{2\pi}{3}) i_b. \quad (3.26)$$

According to equation (3.24) the rotor position is encoded into the amplitude of the induced voltage pulses. Figure 3.4 shows an example of the induced voltage pulses in phase A due to the current in phases B and C. Thus, by measuring the amplitude of these voltage pulses, the position can be estimated by means of a look-up table that can be composed with the use of equation (3.24).

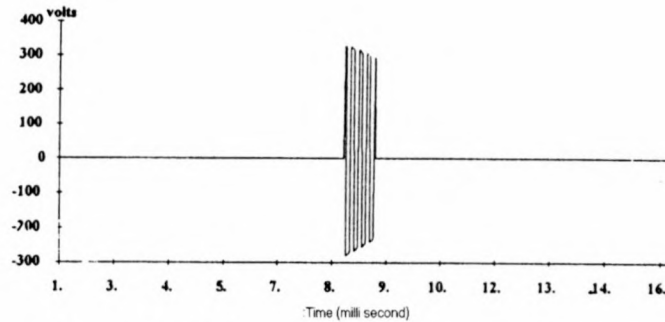


Figure 3.4: Induced voltage pulses in phase A

3.2.1 Comments on this modified-PWM technique on a RSM drive

The modified-PWM technique was implemented by [7] and was evaluated at a constant speed of 1000 rpm. It performed well under these constant speed conditions. This technique does not function very well when the machine is accelerating,

therefore it would best be suited for constant speed applications. However, a big advantage is that this technique can be used at very low speeds. This technique can also be used at zero speed because the phase currents are anyway zero at standstill. This argument is only valid if no torque is produced at the standstill position. It has to be said that this technique is also parameter dependent, such as the L_d and L_q inductances that influence the values of L_B in equations (3.25) and (3.26).

3.3 Sensorless control technique using induced third harmonic voltage

This technique was implemented by L Kreindler, A Testa and TA Lipo [8]. The RSM can be controlled sensorless if the position of the fundamental component of the air-gap flux is known. This fundamental component can be located by measuring the induced third harmonic voltage in the stator. The authors of this paper proved that the resultant component of the air-gap flux, when the machine is saturated, includes all the odd harmonic components such as the third harmonic.

Due to the star-connection and the neutral not connected, no third harmonic currents will flow in the phases and there will be no third harmonic voltage drops across the stator phase impedances. Thus, it can be taken that the third harmonic voltage component in the stator is in phase with the air-gap voltage component under any load conditions.

By measuring and summing the 3-phase voltages the resultant contains mainly a third harmonic voltage. To detect the position and speed of the magnetic flux, the zero crossing of the third harmonic voltage is used. The flux position can now be determined because there is a constant phase shift of $(\pi/2)$ radians between the flux position and the third harmonic component. The authors also proposed two different techniques for the detection of the position between the zero crossings. This is not discussed here furthermore.

3.3.1 Comments on the induced third harmonic voltage technique

This technique does not make use of integration, therefore problems like offsets and noise are avoided. Since the technique requires induced third harmonic voltages, low-speed operation can be a problem, but the technique gave good results at high and medium speeds. It is not always possible to implement this technique because there must be access to the neutral point of the motor.

Chapter 4

4 Voltage Injection Position Sensorless Control Technique

In this chapter the voltage injection technique is discussed in detail. The technique is explained in section 4.1 by means of mathematical manipulation of the voltage equations of the RSM. In section 4.2 these voltage equations are put in block diagram format to simulate the technique.

4.1 Explanation of the voltage injection technique

The voltage injection technique as investigated and implemented by A. Consoli [10] is discussed in this section. This technique is suitable for low and zero speed position sensorless operation of the RSM. This technique consist of applying a high frequency voltage vector to the stator windings, and then by means of the appropriate demodulation of the measured stator currents, the rotor position is estimated. A high frequency voltage vector of about 600 Hz is applied to the stator, in addition to the normal working voltage. This causes a high frequency current vector, $\overline{i_{sh}}$, in the stator windings. If one takes into account the fact that the RSM is a salient pole machine, there has to be a difference in impedance seen by the 600 Hz voltage vector. This means that the measured high frequency current vector, $\overline{i_{sh}}$, will depend on the rotor's position. Also, if one takes a look at the self and mutual inductances (equations (2.4) – (2.9)) of the RSM, it can be seen that all these inductances depend on the position of the rotor.

Figure 4.1 shows how the normal working voltages (v_a, v_b, v_c) and the high frequency voltages (v_{ah}, v_{bh}, v_{ch}) are added and fed to the RSM by means of a 3-phase inverter. The two phase currents (i_a, i_b) are measured, filtered and fed to the current controller and the rotor position estimator. All the components in the block diagram are discussed in detail in Chapter 5.

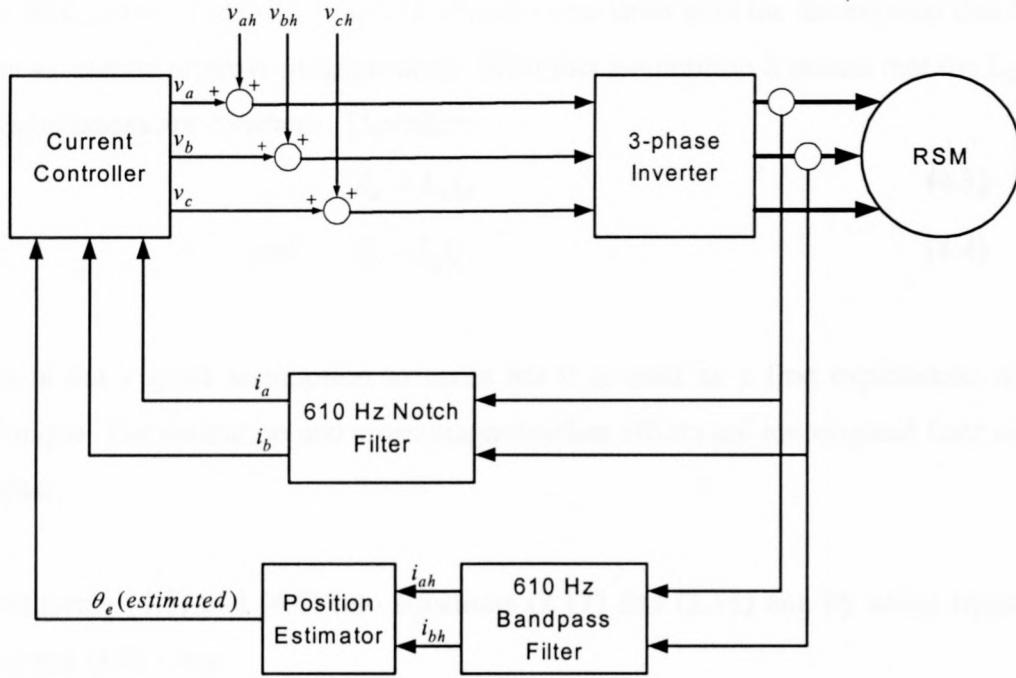


Figure 4.1: Block diagram of the voltage injection technique

Figure 4.2 shows the synchronous rotating voltage vector ($\overline{v_s}$) and the asynchronous, high frequency rotating voltage vector ($\overline{v_{sh}}$). It can easily be seen in Figure 4.2 that the angle of the high frequency voltage component with respect to the rotor is $\theta_h - \theta_r$. Therefore $\overline{v_{sh}}$ can be expressed in the dq co-ordinate system as

$$V_{qh} = |\overline{v_{sh}}| \cos(\theta_h - \theta_r) \quad (4.1)$$

$$\text{and } V_{dh} = |\overline{v_{sh}}| \sin(\theta_h - \theta_r). \quad (4.2)$$

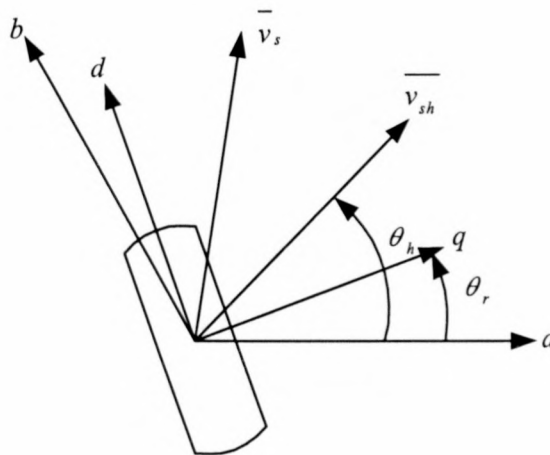


Figure 4.2: 2-pole RSM with the synchronous rotating and high frequency voltage vectors shown

The voltage equations (2.17) and (2.18) are considered with the assumption that there is no saturation or cross-magnetisation. With this assumption it means that the L_d and L_q inductances are constants. Therefore

$$\lambda_d = L_d i_d \quad (4.3)$$

$$\text{and} \quad \lambda_q = L_q i_q. \quad (4.4)$$

This is not a good assumption to make but it is used as a first explanation of the technique. The saturation and cross-magnetisation effects are investigated later in this chapter.

Substituting (4.3) and (4.4) into equations (2.17) and (2.18) and by using equations (4.1) and (4.2) gives

$$V_{sh} \cos(\theta_h - \theta_r) = r_s i_{qh} + \omega_r L_d i_{dh} + L_q \frac{di_{qh}}{dt} \quad (4.5)$$

$$\text{and} \quad V_{sh} \sin(\theta_h - \theta_r) = r_s i_{dh} - \omega_r L_q i_{qh} + L_d \frac{di_{dh}}{dt} \quad (4.6)$$

where $V_{sh} = \sqrt{v_{sh}^2}$.

Assume that the rotor speed is zero and that $\theta_{h0} = 0$, then it can be shown from equations (4.5) and (4.6) that [10]

$$i_{qh} = e^{-\frac{r_s}{L_q}t} + V_{sh} \frac{r_s}{r_s^2 + \omega_h^2 L_q^2} \cos(\omega_h t - \theta_{r0}) + V_{sh} \frac{\omega_h L_q}{r_s^2 + \omega_h^2 L_q^2} \sin(\omega_h t - \theta_{r0}), \quad (4.7)$$

$$i_{dh} = e^{-\frac{r_s}{L_d}t} + V_{sh} \frac{\omega_h L_d}{r_s^2 + \omega_h^2 L_q^2} \cos(\omega_h t - \theta_{r0}) - V_{sh} \frac{r_s}{r_s^2 + \omega_h^2 L_q^2} \sin(\omega_h t - \theta_{r0}), \quad (4.8)$$

where θ_{h0} is the position of the voltage vector at $t = 0$,

θ_{r0} is the position of the rotor at $t = 0$

and ω_h is the speed of the voltage vector in rad/s.

In the steady state the square of the current amplitude can be expressed from equations (4.7) and (4.8) as [10]

$$\begin{aligned}
 I_{sh}^2 &= i_{dh}^2 + i_{qh}^2 \\
 &= R_1 \sin^2(\omega_h t - \theta_{r0}) + R_2 \cos^2(\omega_h t - \theta_{r0}) + R_3 \sin 2(\omega_h t - \theta_{r0}), \quad (4.9)
 \end{aligned}$$

where

$$R_1 = V_{sh}^2 \left(\frac{r_s^2}{(r_s^2 + \omega_h^2 L_d^2)^2} + \frac{\omega_h^2 L_q^2}{(r_s^2 + \omega_h^2 L_q^2)^2} \right) [A^2], \quad (4.10)$$

$$R_2 = V_{sh}^2 \left(\frac{r_s^2}{(r_s^2 + \omega_h^2 L_q^2)^2} + \frac{\omega_h^2 L_d^2}{(r_s^2 + \omega_h^2 L_d^2)^2} \right) [A^2], \quad (4.11)$$

$$R_3 = V_{sh}^2 \left(\frac{r_s \omega_h L_q}{(r_s^2 + \omega_h^2 L_q^2)^2} - \frac{r_s \omega_h L_d}{(r_s^2 + \omega_h^2 L_d^2)^2} \right) [A^2] \quad (4.12)$$

and $I_{sh} = \sqrt{i_{sh}^2}$.

As is clear, the three coefficients (R_1, R_2 and R_3) of equation (4.9) are functions of the machine parameters and the voltage and frequency of the high frequency voltage. It can be shown that at high frequencies, for the 5.5 kW RSM and the RSM [10] used, R_2 and R_3 becomes insignificant compared to R_1 . In that case, thus, equation (4.9) becomes

$$I_{sh}^2 = R_1 \sin^2(\omega_h t - \theta_{r0}). \quad (4.13)$$

This result implies that I_{sh}^2 will be a minimum when the high frequency voltage vector is aligned with the q-axis and a maximum when the high frequency voltage vector is aligned with the d-axis of the RSM. The latter can be explained from Figure 4.2 and equation (4.13). Figure 4.2 shows that θ_r is the angle between the phase-a axis and the q-axis. Thus if the high frequency voltage vector angle, $\theta_h = \omega_h t$, equals $\theta_r = \theta_{r0}$, equation (4.13) shows that I_{sh}^2 will then be a minimum. If the high frequency voltage vector is aligned with the d-axis, the angle, $\omega_h t - \theta_{r0}$, equals 90° and from equation (4.13), I_{sh}^2 will then be a maximum.

To show the frequency dependency of R_2 and R_3 and the relative sizes compared to R_1 , the parameters of the RSMs were studied and used in the analysis. The first machine is a small 5.5 kW RSM and the second one is a 110 kW RSM. The relevant

data and parameters of these machines are given in Table 4.1. The values for L_d and L_q were obtained by means of the finite element method (FEM). Figure 4.3 and Figure 4.4 show the relative sizes of these coefficients compared to R_1 , for both RSMs. Figure 4.3 shows that R_2 and R_3 are very small compared to R_1 already at low frequencies. Figure 4.4, however, shows that R_2 of the 110 kW RSM is not small compared to R_1 . This may seem to be a problem. Equation (4.9), however, shows that the signals of the first two terms are 180° out of phase. This means that only the amplitude of I_{sh}^2 will change, but not the phase angle if R_2 is not small compared to R_1 . It will be shown through simulations that there is no phase shift. Figures 4.3 and 4.4 show that the R_1 - R_3 coefficients do not change at frequencies above, say, 300 Hz. To determine the frequency of the high frequency voltage component, a frequency of above 300 Hz, thus, must be used. Ideally this frequency must be very high, thus minimising the torque ripple caused by the high frequency voltage component. The limiting factor, however, is the switching frequency of the inverter, which is 5 kHz. Standard frequencies, in the 300 Hz range, that can easily be generated by the DSP controller are 152.5 Hz, 305 Hz, 610 Hz and so on. Therefore a frequency of 610 Hz, that is about 10 times below the switching frequency, was chosen.

Rated power	5.5 kW	110 kW
Rated voltage	330 V	500 V
Pole Pairs	2	3
Rated speed	1500 Rpm	1500 Rpm
Rated torque	33 Nm	700 Nm
r_s	0.65 Ω	0.028 Ω
L_d	135 mH	7.5 mH
L_q	45 mH	6.5 mH

Table 4.1: Parameters of the two RSMs [13] and [1]

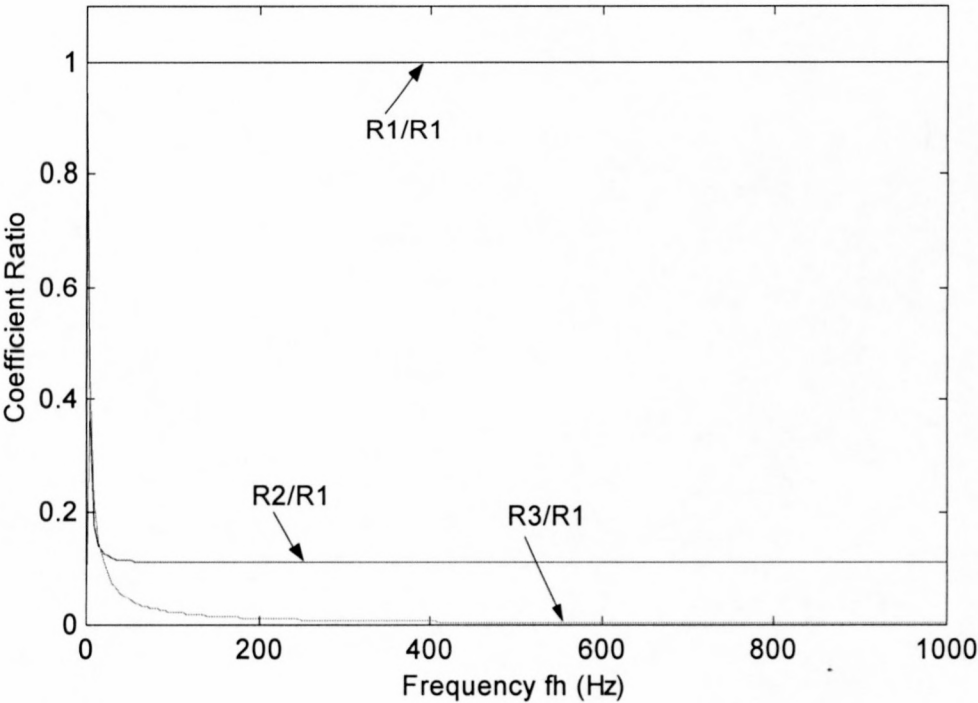


Figure 4.3: Coefficient ratios versus frequency of the 5.5 kW RSM

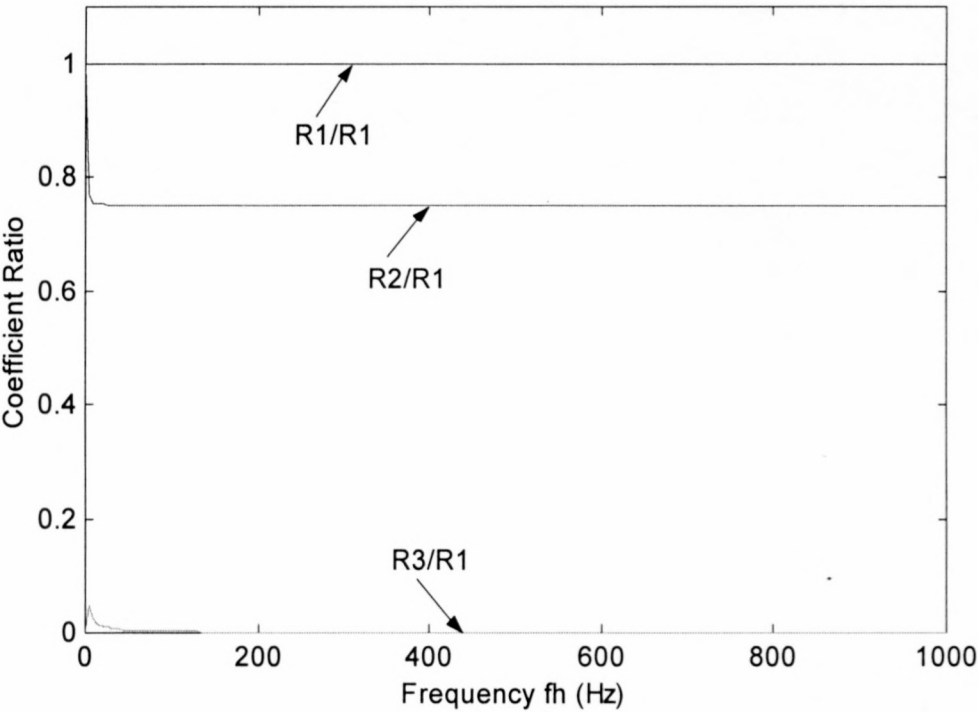


Figure 4.4: Coefficient ratios versus frequency of the 110 kW RSM

4.2 Simulations of the voltage injection method

The voltage injection method is intensively investigated in this section by making use of the mathematical model of the RSM. The voltage equations (2.17) and (2.18) of the machine are put into a block diagram format to be used in a simulation package called Simuwin. The first model of the RSM will take L_d and L_q as constants, then the next model will take saturation and cross magnetisation into account. Lastly the effect of a slotted air-gap will be investigated.

4.2.1 Simulations with L_d and L_q as constants

The voltage equations with L_d and L_q taken as constants are

$$v_d = r_s i_d + L_d \frac{di_d}{dt} - \omega L_q i_q \quad (4.14)$$

$$\text{and} \quad v_q = r_s i_q + L_q \frac{di_q}{dt} + \omega L_d i_d. \quad (4.15)$$

Figure 4.5 shows equations (4.14)-(4.15) in block diagram format.

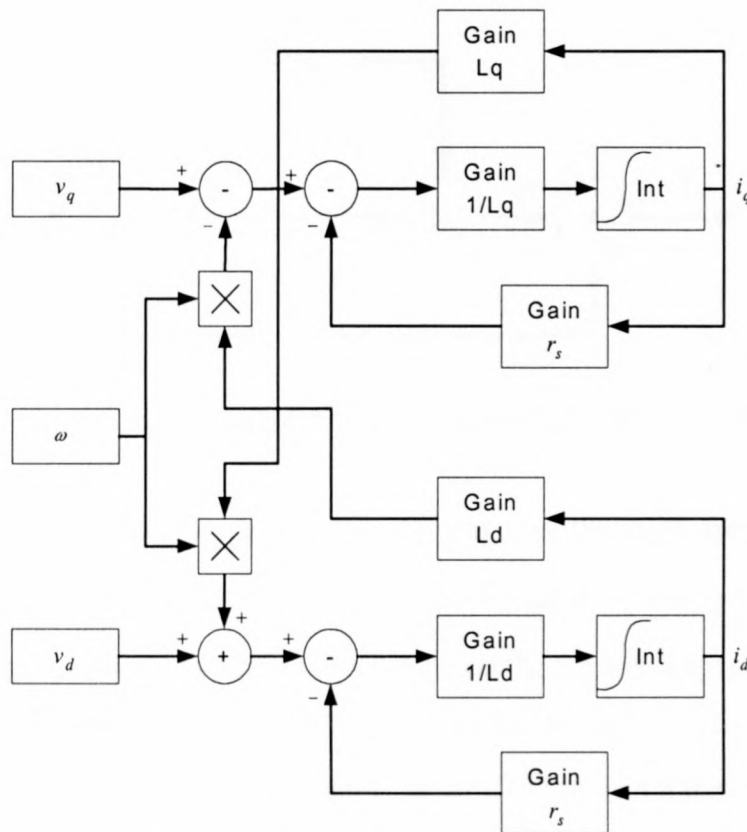


Figure 4.5: Model of the RSM with L_d and L_q as constants

The voltage supplying the RSM consists of two components. The first component is the normal power supply voltage or the working voltage of the machine. The second component is the high frequency voltage signal that is been used for the rotor position estimation. As was discussed before, this component causes a 610 Hz rotating voltage vector in the machine. Equations (4.1) and (4.2) give the dq representation of the high frequency voltage vector in the machine. The normal power supply voltage also causes a rotating voltage vector in the machine that runs synchronously with the rotor if the machine is in the steady state. Thus, under steady state conditions the dq- values of the power supply voltage are dc values. In Figure 4.6 the dq-values of the two voltage components are given in block diagram format.

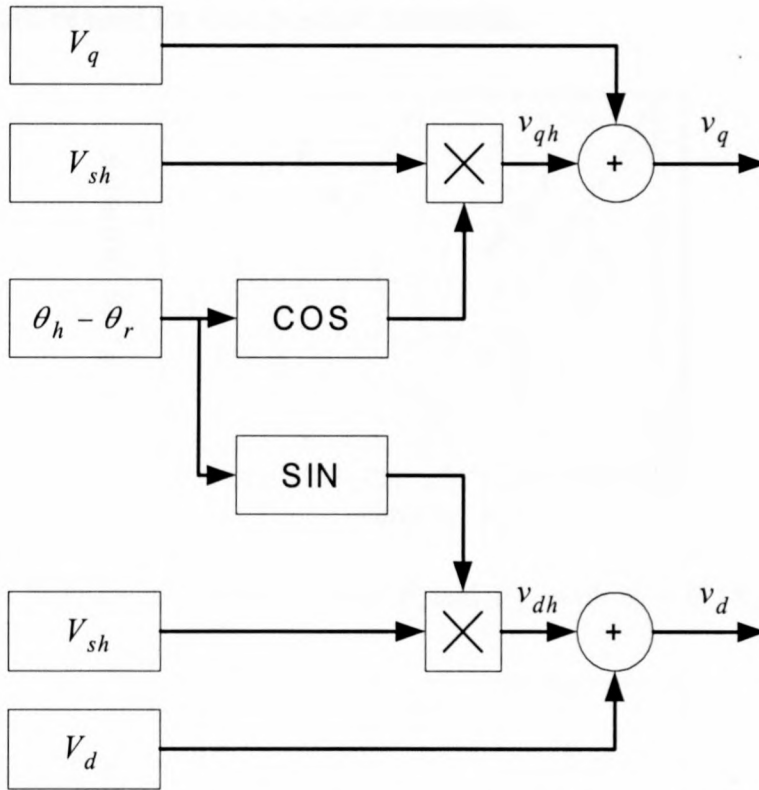


Figure 4.6: Block diagram of the voltages that supply the RSM

Assume the motor speed is zero ($\omega_m = 0$) and that the high frequency voltage component is the only voltage supplied to the RSM, that is $V_q = V_d = 0$ in Figure 4.6. Figures 4.7 and 4.8 shows two simulations done on the 5.5 kW RSM, using the block diagrams shown in Figures 4.5 and 4.6. In Figure 4.7 the rotor position is zero and it can be seen that I_{sh}^2 is a minimum when θ_h is zero. In Figure 4.8 the rotor was turned from zero and in the simulation a definite phase angle difference can be seen between

θ_h and I_{sh}^2 . To calculate the position of the rotor, this phase angle difference has to be measured. Figure 4.9 is a simulation of the 110 kW RSM, also with the rotor at zero position. It can be seen that the fluctuation of the current waveform for the 110 kW machine is much less than the fluctuation of the current waveform for the 5.5 kW machine. This can be explained by looking at Figures 4.3 and 4.4. The coefficient, R_2 is relatively much larger for the 110 kW machine than for the 5.5 kW machine, causing the larger offset of I_{sh}^2 . The latter can also be explained by equation (4.9). From the simulation results it is clear that this coefficient do not cause any phase shift in the I_{sh}^2 -signal. So, in the case where the R_2 -coefficient is relatively large, the I_{sh}^2 -signal can still be used for rotor position estimation.

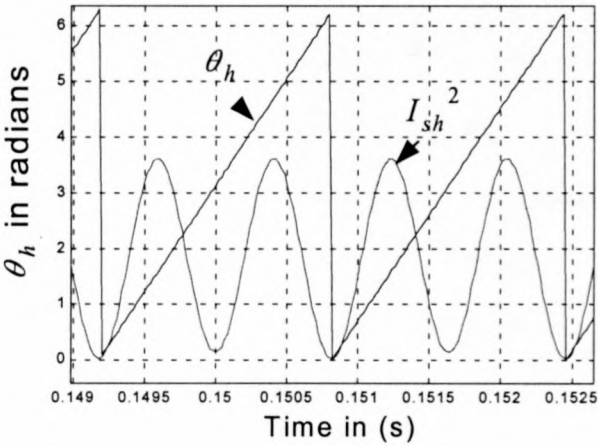


Figure 4.7: Phase difference between θ_h and I_{sh}^2 with $\theta_r = 0^\circ$ (5.5 kW RSM)

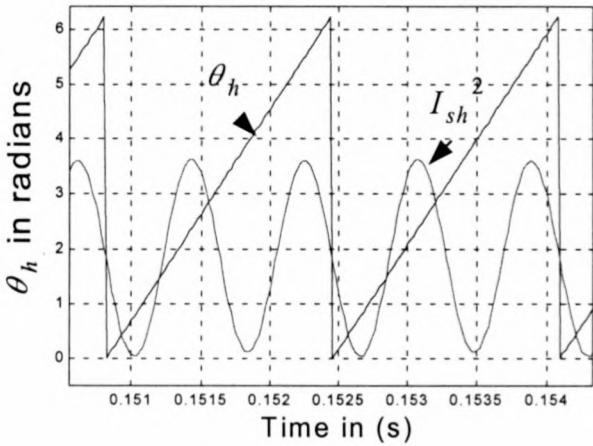


Figure 4.8: Phase difference between θ_h and I_{sh}^2 with $\theta_r = 45^\circ$ (5.5 kW RSM)

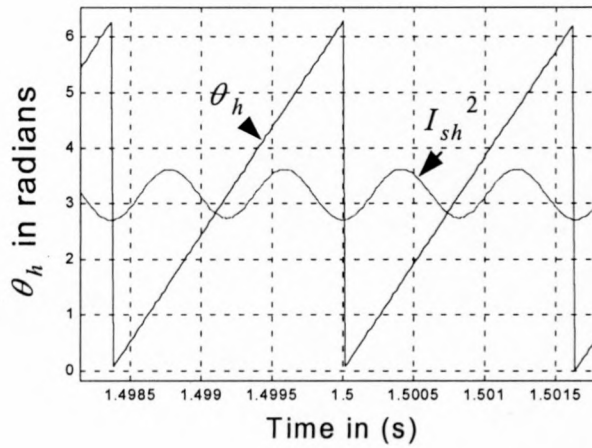


Figure 4.9: Phase difference between θ_h and I_{sh}^2 with $\theta_r = 0^\circ$ (110 kW RSM)

4.2.2 Simulations taking into account saturation and cross magnetisation

All the previous calculations and simulations were done with L_d and L_q as constants. This assumption was made to simplify the problem. However these inductances depend on the d-axis and the q-axis currents. To investigate the effects of saturation and cross magnetisation it is much easier to work with the flux-linkages of the machine (see Figures 4.10 and 4.11) than with the inductances. In Figure 4.10 it can be seen how the gradients of the curves become smaller as the current increases. This happens because the magnetic material of the machine saturates.

Cross magnetisation is defined as the magnetic coupling between the fictitious d-axis and q-axis windings of the machine. In Figure 4.10 seven different curves are drawn. Each of these curves represent a different constant i_q -value. This means that as i_q changes, so does λ_d , due to cross magnetisation. Figures 4.10 and 4.11 were obtained from finite element analysis [27].

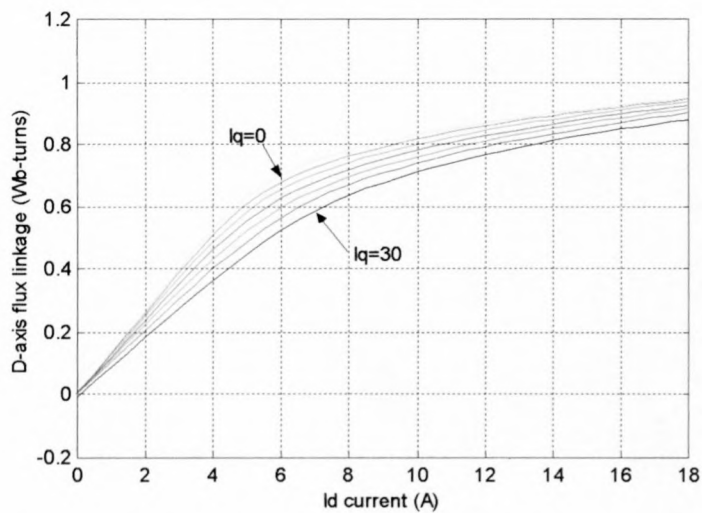


Figure 4.10: d-axis flux-linkage versus d-axis current (5.5 kW RSM) [27]

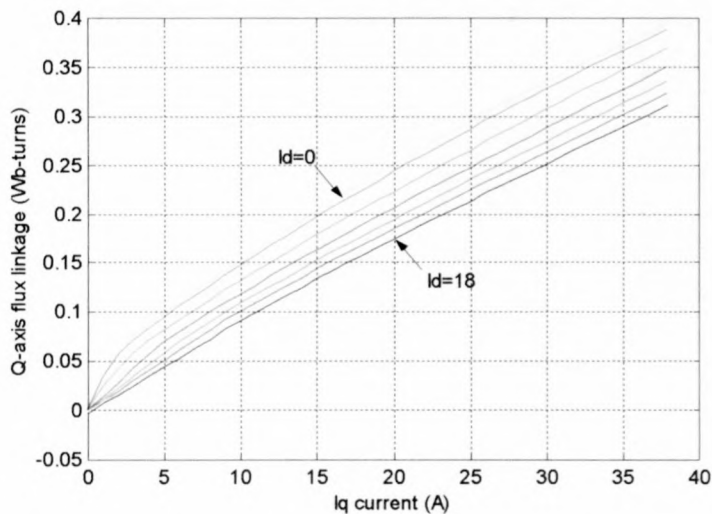


Figure 4.11: q-axis flux-linkage versus q-axis current (5.5 kW RSM) [27]

To do the analysis in terms of the flux-linkages, the voltage equations (2.17) and (2.18) are transformed into block diagram format as shown in Figure 4.12. In the block diagram, the outputs of the two integrators are equal to the flux-linkages. Considering for example λ_q , it can be seen that the block ‘ i_q Calc’ has to calculate the value of i_q with λ_q and i_d as inputs. This can be done by making use of Figure 4.11. In Figure 4.11, i_q is the independent variable and λ_q the dependent variable. ‘ i_q Calc’ is thus an inverse function of the curves of Figure 4.11. The same was done to calculate i_d , with ‘ i_d Calc’ the inverse function of the curves of Figure 4.10. Thus, ‘ i_d Calc’ calculates the value of i_d with λ_d and i_q as inputs.

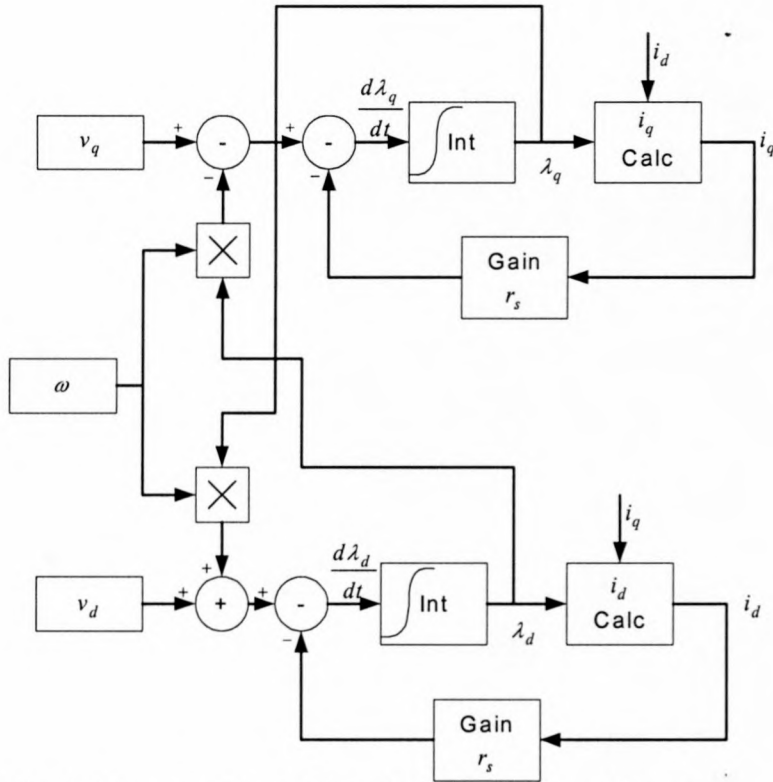


Figure 4.12: Block diagram of the RSM taking saturation and cross magnetisation into account

To ignore the effect of cross magnetisation, the i_d input of 'i_q Calc' and the i_q input of 'i_d Calc' are made zero. This means that only the ($i_q = 0$) curve in Figure 4.10 and the ($i_d = 0$) curve in Figure 4.11 are used. This implies that only the effect of saturation is investigated.

Figures 4.13 and 4.14 show simulations done to study the effect of saturation. In both figures, the simulations are done with the average dq currents equal to $I_d = I_q = 1$ A (curve A) and with $I_d = I_q = 10$ A (curve B). It can be seen that curves A and B do not have the same amplitude, but are always in phase. This implies that saturation do not cause any phase shift in the I_{sh}^2 -signal. As was explained before, the rotor position is the phase difference between a minimum point of the I_{sh}^2 -signal and the negative edge of the θ_h -signal. In Figure 4.13 the rotor position is 0° and it can be seen that the phase difference is zero. In Figure 4.14 the rotor position is 90° and a 90° phase difference between the I_{sh}^2 and the θ_h signals can be seen.

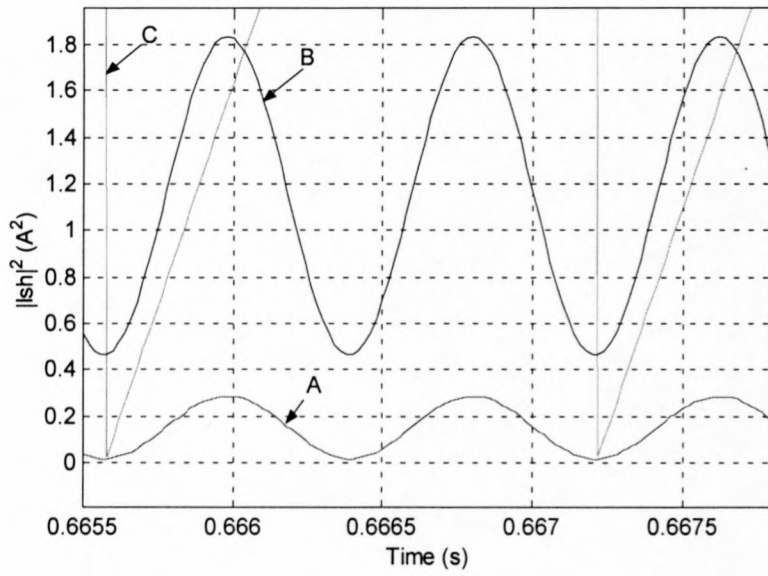


Figure 4.13: Comparison between I_{sh}^2 and θ_h with $\theta_r = 0^\circ$ (5.5 kW RSM)

$A = I_{sh}^2$ with I_d and $I_q = 1$ A; $B = I_{sh}^2$ with I_d and $I_q = 10$ A;

$C = \text{the negative edge of } \theta_h.$

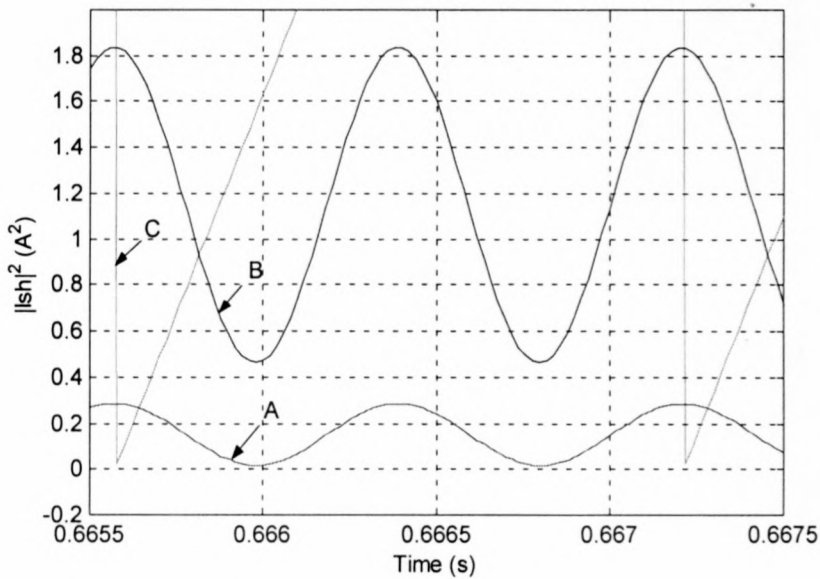


Figure 4.14: Comparison between I_{sh}^2 and θ_h with $\theta_r = 90^\circ$ (5.5 kW RSM)

$A = I_{sh}^2$ with I_d and $I_q = 1$ A; $B = I_{sh}^2$ with I_d and $I_q = 10$ A;

$C = \text{the negative edge of } \theta_h.$

To study the effect of cross magnetisation, the I_{sh}^2 signals of the machine model with cross magnetisation and the machine model without cross magnetisation are compared. It was shown in Figures 4.13 and 4.14 that the machine model without cross magnetisation (only saturation) does not cause any phase shift between I_{sh}^2 and θ_h , even if the I_d and I_q currents are large. Therefore, the error in the position estimation caused by cross magnetisation, is equal to the phase shift between these two I_{sh}^2 signals. Figures 4.15 – 4.17 show the simulation results of this study about cross magnetisation. With I_d low, the two simulations in Figure 4.15 show a very small phase shift. Figures 4.16 and 4.17 show how the phase shift becomes more as the d-axis current increases. With $I_d = 10$ A, i.e. the rated d-axis current, the phase shift is about 30° . Therefore, because of cross magnetisation an error of 30° is made in estimating the position if $I_d = 10$ A.

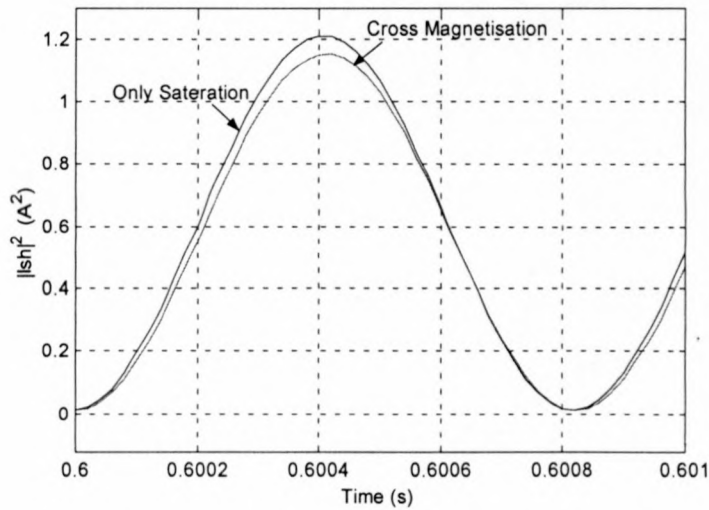


Figure 4.15: Comparison between the effects of cross magnetisation and saturation with $I_d = 2$ A and $I_q = 3$ A (5.5 kW RSM)

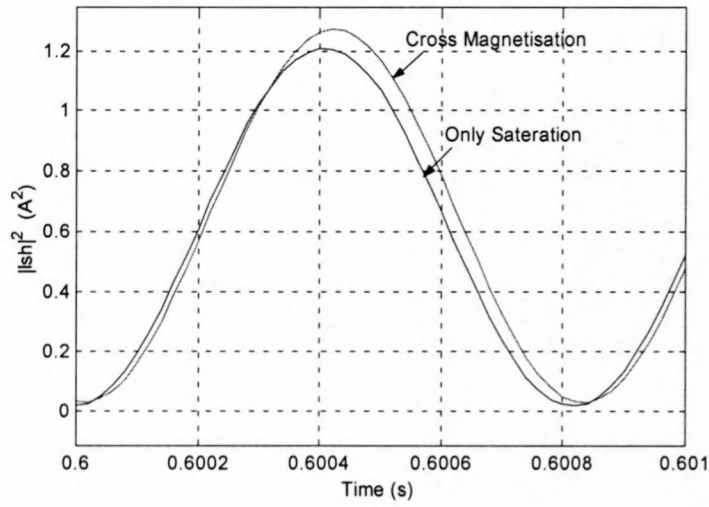


Figure 4.16: Comparison between the effect of cross magnetisation and saturation with $I_d = 5$ A and $I_q = 3$ A (5.5 kW RSM)

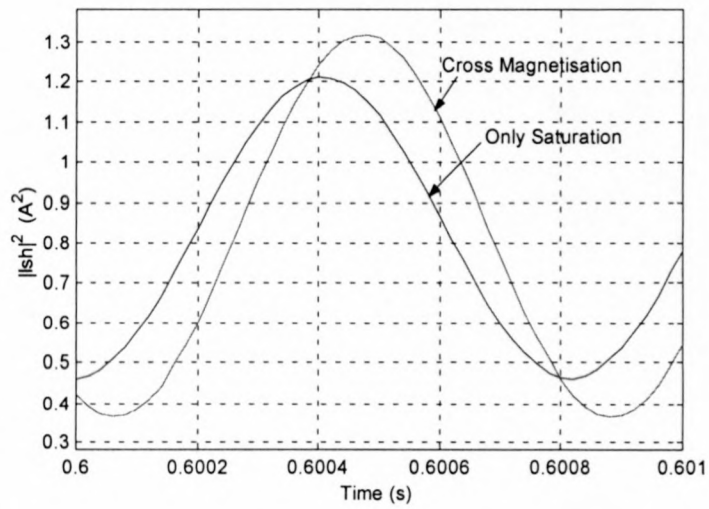


Figure 4.17: Comparison between the effect of cross magnetisation and saturation with $I_d = 10$ A and $I_q = 3$ A (5.5 kW RSM)

The above observed phase shift can be explained as follows. To account for the saturation and cross magnetisation effects in the machine, the mathematical model, as defined by equations (4.14) and (4.15), has to be changed. The flux-linkages are functions of

$$\lambda_d = f(i_d, i_q) \quad (4.16)$$

$$\text{and } \lambda_q = f(i_d, i_q). \quad (4.17)$$

Differentiation of the flux-linkages transforms the voltage equations (2.17) and (2.18) into partial differential equations. Therefore

$$v_d = r_s i_d + \frac{\partial \lambda_d}{\partial i_d} \frac{di_d}{dt} + \frac{\partial \lambda_d}{\partial i_q} \frac{di_q}{dt} - \omega \lambda_q \quad (4.18)$$

$$\text{and} \quad v_q = r_s i_q + \frac{\partial \lambda_q}{\partial i_q} \frac{di_q}{dt} + \frac{\partial \lambda_q}{\partial i_d} \frac{di_d}{dt} + \omega \lambda_d. \quad (4.19)$$

Considering only equation (4.18), the differential inductances are defined as

$$L_d^\partial = \frac{\partial \lambda_d}{\partial i_d} \quad (i_q = \text{constant}) \quad (4.20)$$

$$\text{and} \quad M_d^\partial = \frac{\partial \lambda_d}{\partial i_q}. \quad (4.21)$$

Figure 4.18 shows the block diagram format of equation (4.18). using equations (4.20) and (4.21). In the block diagram it can be seen that because of the cross magnetisation inductance M_d^∂ , i_q has an influence on the value of i_d . Because i_{qh} and i_{dh} are 90° out of phase, the cross magnetisation inductance M_d^∂ will cause a phase shift in the I_{sh}^2 -signal.

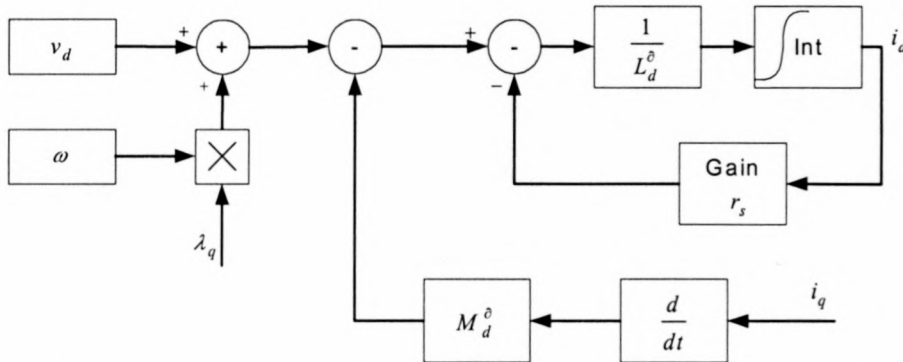


Figure 4.18: Block diagram of equations (4.18), (4.20) and (4.21)

The same simulations as on the 5.5 kW RSM were also done on the 110 kW RSM. The results are shown in Figures 4.19 and 4.20. Also with this machine the large phase shift due to cross magnetisation, can be seen.

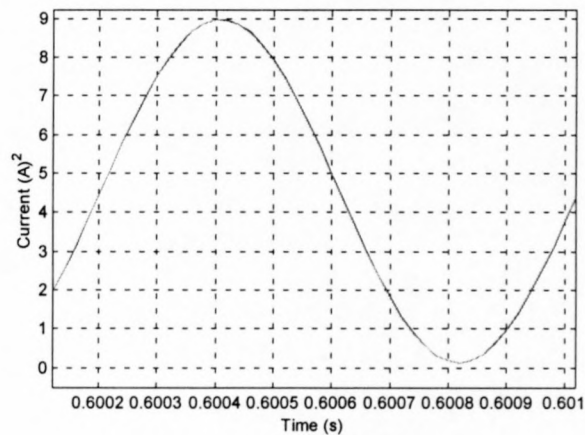


Figure 4.19: I_{sh}^2 plotted to compare saturation and cross magnetisation with $I_d = 50$
A and $I_q = 50$ A

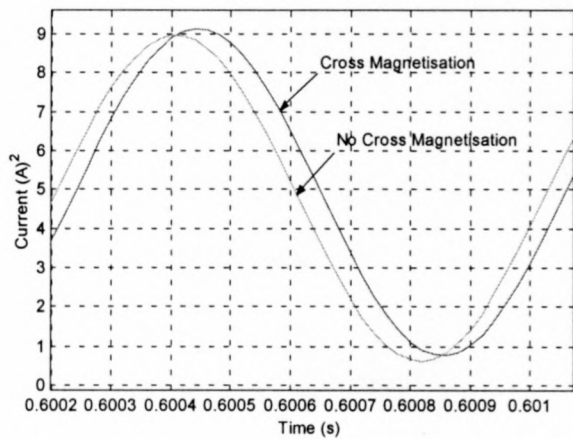


Figure 4.20: I_{sh}^2 plotted to compare saturation and cross magnetisation with $I_d = 125$
A and $I_q = 50$ A

4.2.3 Simulations taking into account the slotted air-gap

The 5.5 kW RSM is an unskewed machine, therefore there are large fluctuations in the flux linkages because of the slotted air-gap. With the FEM, simulations of the 5.5 kW machine were done to obtain data of the fluctuations of the flux linkages as the rotor rotates. With $I_d = 9$ A and $I_q = 3$ A the following results were obtained. Figure 4.21 shows the fluctuations in the d-axis flux linkage and Figure 4.22 shows the fluctuations in the q-axis flux linkage as a function of the rotor position.

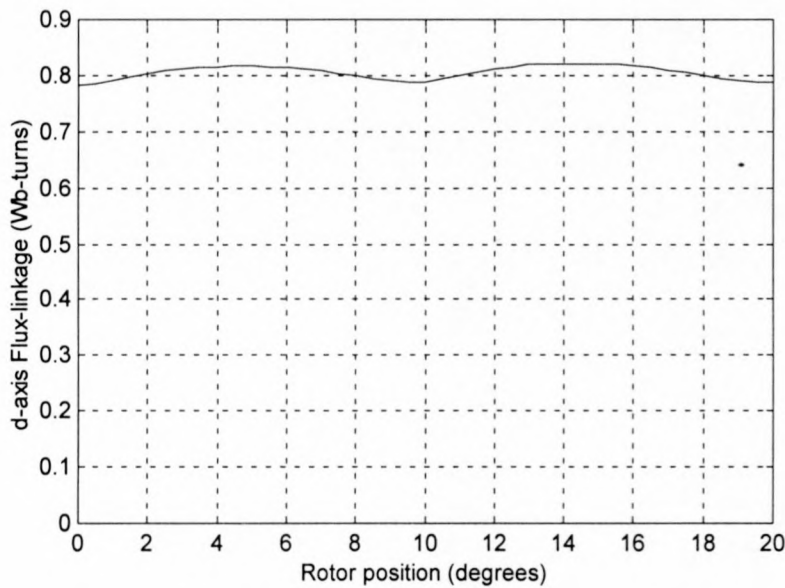


Figure 4.21: d-axis flux-linkage versus rotor position ($I_d=9$ A; $I_q=3$ A)

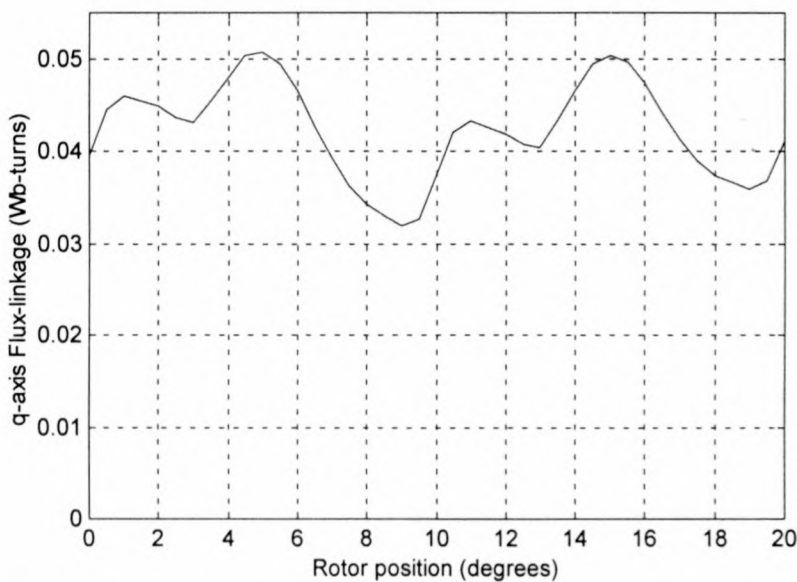


Figure 4.22: q-axis flux linkage versus rotor position ($I_d=9$ A; $I_q=3$ A)

Figures 4.21 and 4.22 showed that the flux linkages are also dependent on the rotor position. Therefore equations (4.16) and (4.17) have to be redefined as

$$\lambda_d = f(i_d, i_q, \theta) \quad (4.22)$$

$$\text{and } \lambda_q = f(i_q, i_d, \theta). \quad (4.23)$$

The voltage equations (4.18) and (4.19) then become

$$v_d = R_s i_d + \frac{\partial \lambda_d}{\partial i_d} \frac{di_d}{dt} + \frac{\partial \lambda_d}{\partial i_q} \frac{di_q}{dt} + \frac{\partial \lambda_d}{\partial \theta} \frac{d\theta}{dt} - \omega \lambda_q \quad (4.24)$$

$$\text{and } v_q = R_s i_q + \frac{\partial \lambda_q}{\partial i_q} \frac{di_q}{dt} + \frac{\partial \lambda_q}{\partial i_d} \frac{di_d}{dt} + \frac{\partial \lambda_q}{\partial \theta} \frac{d\theta}{dt} + \omega \lambda_d. \quad (4.25)$$

In equations (4.24) and (4.25) two new terms appear, $\frac{\partial \lambda_d}{\partial \theta} \frac{d\theta}{dt}$ and $\frac{\partial \lambda_q}{\partial \theta} \frac{d\theta}{dt}$, where

$\frac{d\theta}{dt} = \omega$. $\frac{\partial \lambda_d}{\partial \theta}$ is the gradient of the curve of Figure 4.21 and $\frac{\partial \lambda_q}{\partial \theta}$ is the gradient of

the curve of Figure 4.22. Thus, to investigate the effect of a slotted air-gap, the derivatives of the curves in Figures 4.21 and 4.22 have to be determined. The results are given in Figures 4.23 and 4.24.

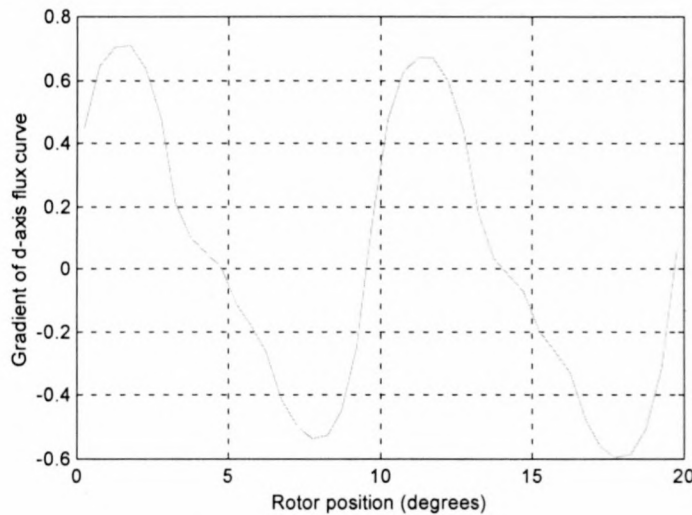


Figure 4.23: $\frac{\partial \lambda_d}{\partial \theta}$ versus rotor position ($I_d=9\text{A}$; $I_q=3\text{A}$)

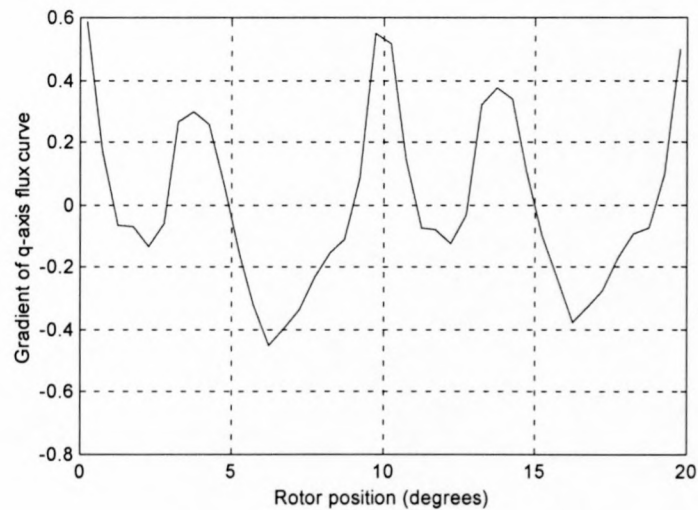


Figure 4.24: $\frac{\partial \lambda_q}{\partial \theta}$ versus rotor position ($I_d=9\text{A}$; $I_q=3\text{A}$)

Equations (4.24) and (4.25) are almost the same as equations (4.18) and (4.19) except for the two new terms $\frac{\partial \lambda_d}{\partial \theta} \frac{d\theta}{dt}$ and $\frac{\partial \lambda_q}{\partial \theta} \frac{d\theta}{dt}$. The block diagram in Figure 4.12 is a representation of equations (4.18) and (4.19). Therefore, the same block diagram can be used for equations (4.24) and (4.25), but the two new terms $\frac{\partial \lambda_d}{\partial \theta} \frac{d\theta}{dt}$ and $\frac{\partial \lambda_q}{\partial \theta} \frac{d\theta}{dt}$ must be taken into account. Figure 4.25 shows the new block diagram that takes a slotted air-gap into account.

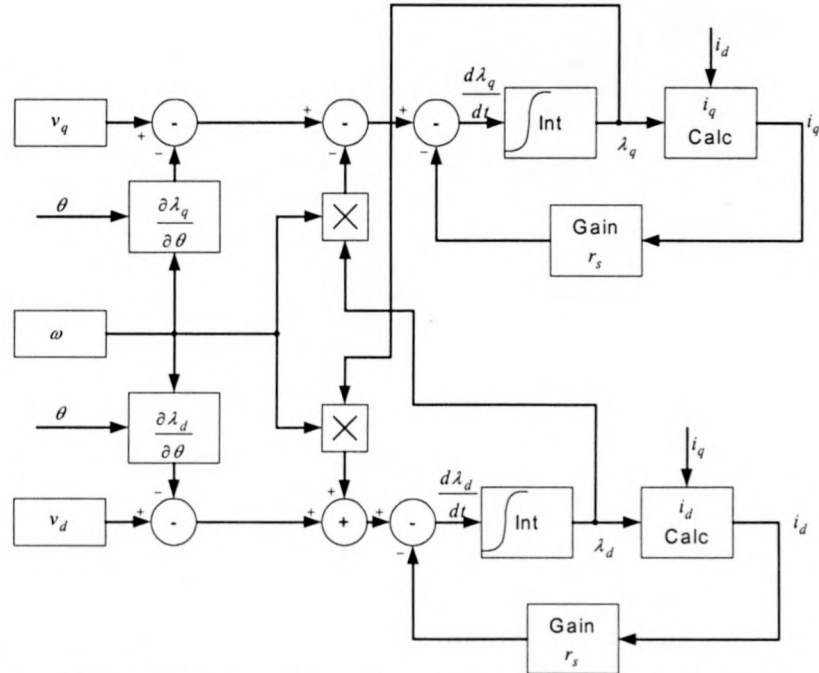


Figure 4.25: Block diagram taking a slotted air-gap into account

With the use of the block diagram of Figure 4.25 a simulation was done with the machine speed set to 150 rev/min (5 Hz). Figures 4.26 – 4.28 show how the estimated position varies as the rotor turns. With the rotor at 0° and 10° the two signals (I_{sh}^2 for a slotted and smooth air-gap) are almost in phase (within 5°). As the rotor moves to 20° a phase shift of about 15° between the two signals is observed.

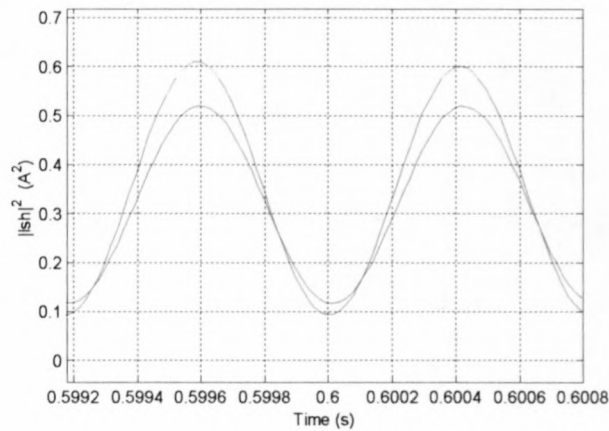


Figure 4.26: Comparing I_{sh}^2 for a slotted and smooth air-gap with $\theta = 0^\circ$
(red curve = I_{sh}^2 for slotted air-gap; blue curve = I_{sh}^2 for smooth air-gap)

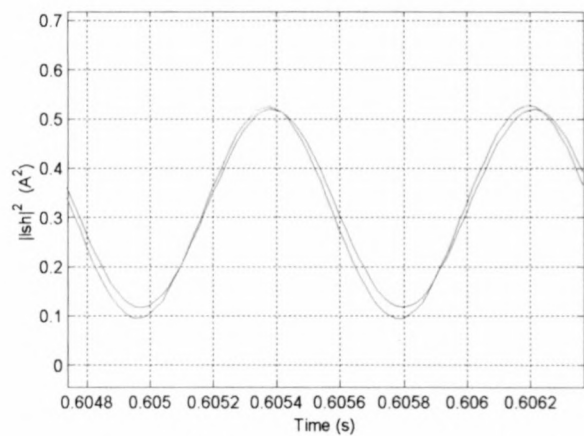


Figure 4.27: Comparing I_{sh}^2 for a slotted and smooth air-gap with $\theta = 10^\circ$
(red curve = I_{sh}^2 for slotted air-gap; blue curve = I_{sh}^2 for smooth air-gap)

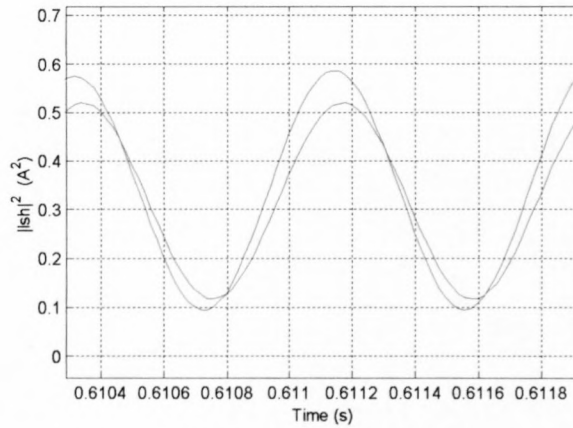


Figure 4.28: Comparing I_{sh}^2 for a slotted and non-slotted air-gap with $\theta = 20^\circ$
 (red curve = I_{sh}^2 for slotted air-gap; blue curve = I_{sh}^2 for smooth air-gap)

4.3 Summary

It was shown that saturation of the magnetic material of the RSM does not cause any error in the rotor position estimation. Sections 4.2.2 and 4.2.3, however, discussed and showed the negative effects of cross magnetisation and a slotted air-gap on the accuracy of the position estimation. In short it can be said that the error made in estimating the rotor position due to cross magnetisation and a slotted air-gap, is large when the d-axis current is large (equal to the rated d-axis current).

Chapter 5

5 Implementation of the Voltage Injection Technique.

The voltage injection technique as discussed and explained in Chapter 4, is implemented and evaluated on both RSM drive systems that were considered in this thesis. In Figure 5.1 the block diagram for both RSM drive systems is shown. Figure 5.2 shows a photo of the experimental set-up of the 110 kW RSM drive system. The two big cabinets in the background are a thyristor controlled rectifier (left) and an IGBT inverter (right). The thyristor controlled rectifier (0-900 V; 500 A) supply the dc-bus of the 630 kVA IGBT inverter, which feeds the RSM (Figure 5.2, middle). A 600 kW dynamometer (Figure 5.2, left front) was used as the mechanical load. Figure 5.3 shows the 5.5 kW RSM. For this drive system a smaller inverter (14 kVA) and a dc motor as a mechanical load, were used.

The DSP Controller of Figure 5.1 generates the PWM signals, for switching the inverter, and a high frequency position signal θ_h for the position estimation. The PWM signals are not directly fed to the inverter but through a Protection Interface Card which measures the dc-bus and the 3-phase currents. If the Protection Interface Card measures an over current or over voltage condition, the six IGBTs of the inverter are switched off. The Measurement and Position Estimation Card measures two phase currents and converts these currents to voltages that can be measured by the ADC of the DSP. This card also determines the position of the rotor.

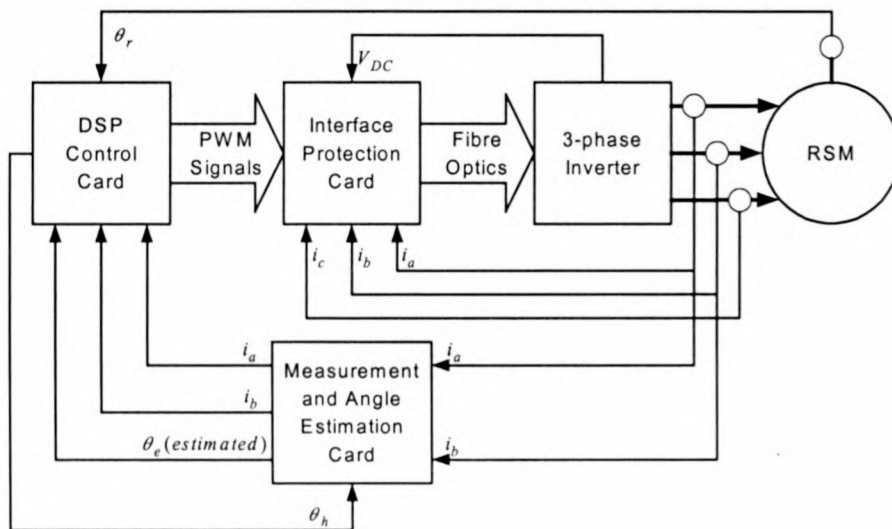


Figure 5.1: System Block diagram

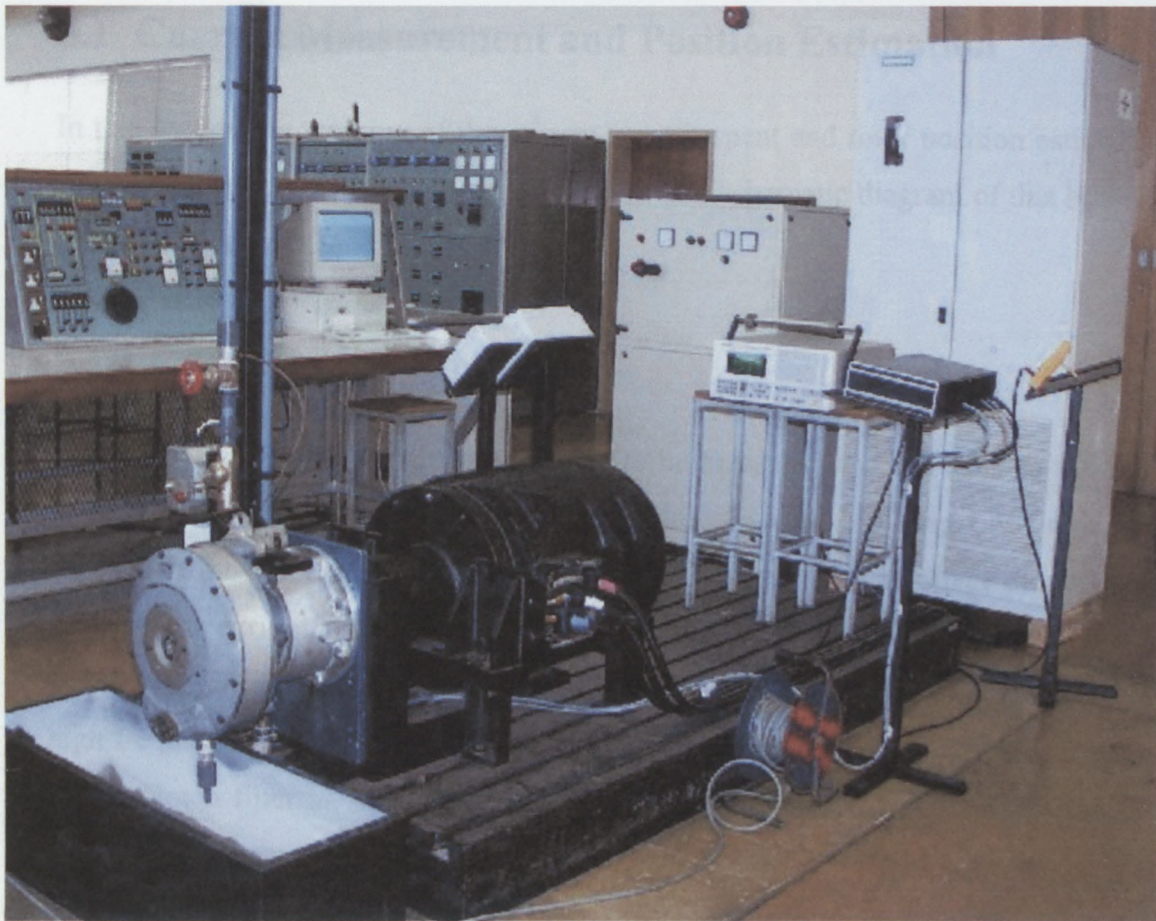


Figure 5.2: 110 kW RSM experimental set-up

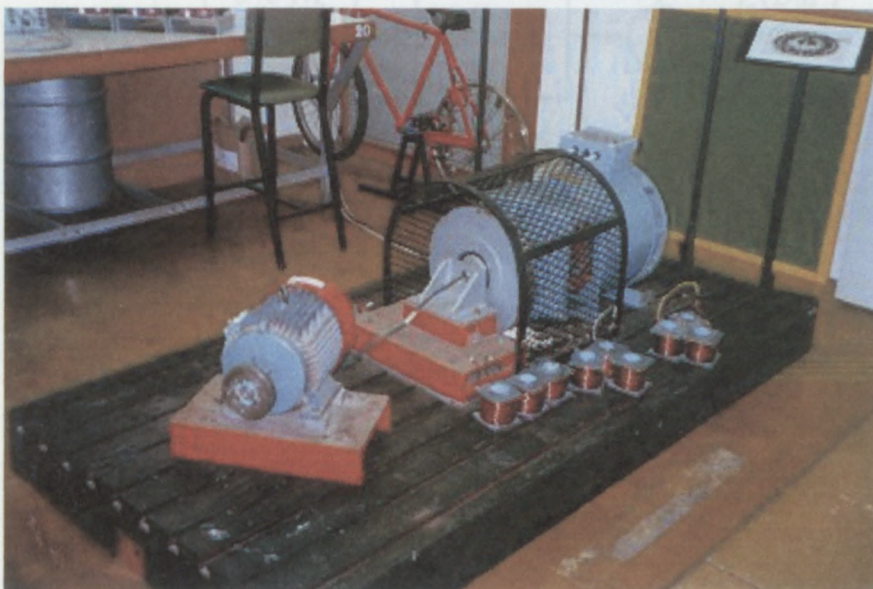


Figure 5.3: 5.5 kW RSM (left front)

5.1 Current Measurement and Position Estimation

In this section the working of the current measurement and rotor position estimation card of Figure 5.1 is described in more detail. The schematic diagram of this board is given in Appendix C.

5.1.1 Current Measurement

For vector control the phase currents have to be measured and fed back to the DSP controller. The two phase currents (i_a and i_b) are measured by using LEM modules. Each LEM module's output terminates on a resistor, presenting a voltage proportional to the phase current. This measured current also contains the 610 Hz high frequency current component that is used for position estimation. For proper vector control the high frequency component must be filtered out from the feedback loop. This is done with a Notch filter as shown in Figure 5.4. The 610 Hz Notch Filter passes all the frequencies except the 610 Hz components. Because the DSP's ADC can only handle voltages between 0 V and 5 V, the measured voltage that is in the range of -15 to $+15$ V has to be scaled to this voltage levels, with a 2.5 V offset.

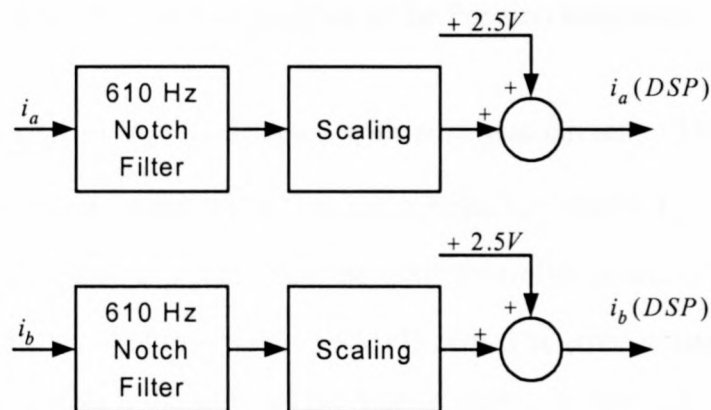


Figure 5.4: Block diagram of the current measurement

5.1.2 Position Estimation

There are three different current components flowing in the stator. These are (i) the 610 Hz high frequency component, used for rotor position estimation, (ii) the switching frequency current component due to the switching of the inverter and (iii) the fundamental torque producing current component. In the block diagram of Figure 5.5 two bandpass filters, discussed further in section 5.1.2a, are used to filter out the fundamental and switching frequency current components. This ensures that only the 610 Hz current components are fed to the next stage, where I_{sh}^2 is determined (see further section 5.1.2b.)

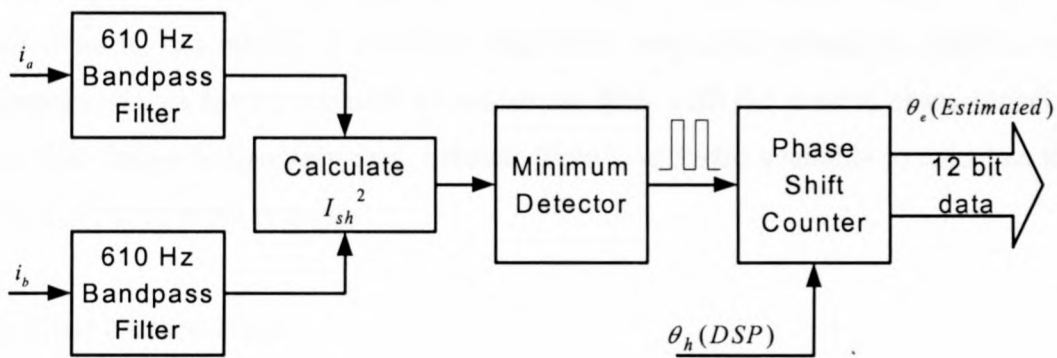


Figure 5.5: Block diagram of the Position Estimator.

The minimum point of I_{sh}^2 is detected with analogue circuitry. The output of the minimum detector is a square wave that has a negative edge if I_{sh}^2 is a minimum. This board receives also a signal from the DSP controller board, $\theta_h(DSP)$, which indicates when the angle of the voltage vector is zero. The latter is also a square wave that has a negative edge if the angle of the high frequency voltage vector goes to zero. The Phase Shift Counter calculates the phase difference between these two signals. This counter is an EPLD that is programmed to start counting at the negative edge of $\theta_h(DSP)$ and stop counting at the negative edge of I_{sh}^2 -minimum. The output of the EPLD is the rotor position in 12 bit digital format. Because the Position Estimation Card and the DSP control card were separately developed this digital value is transformed to an analogue value by a DAC and fed to the DSP controller (see Figure 5.1). It will be better to feed the 12 bit position data directly to the data bus of the DSP.

a) Bandpass (BP) Filter

The bandpass filter is the most critical part of the position estimation board. Care has to be taken to make sure that all the current components, except the 610 Hz component, are rejected. This asks for a sharp roll-off frequency. However, this sharp cut-off causes the problem of phase shift. As can be seen in Figure 5.6b, the phase angle changes very rapidly around the pass frequency (610 Hz). In the block diagram of Figure 5.5 two bandpass filters are used, one for each phase current. Because of the rapid change in phase angle, the tolerances of the electronic components can cause different phase shifts for i_a and i_b . To overcome this problem a filter IC (UAF42) was used. This IC has internal components that have very small tolerances. Only a few external resistors have to be used to realise the filter with the desired characteristics. The filter design is also very easy, because there is software available to calculate the values of the external resistors.

The Filter characteristics:

- Type: 4th order Butterworth
- Centre Frequency: 610 Hz
- Band width: 60 Hz

With these specifications the software calculates the resistor values. The gain and the phase angle versus frequency of the filter are plotted in Figure 5.6.

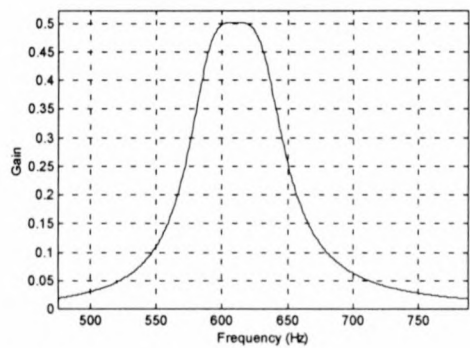


Figure 5.6a: Magnitude versus Frequency of the BP Filter.

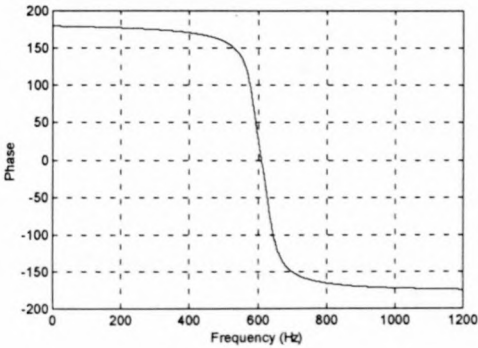


Figure 5.6b: Phase versus frequency of the BP Filter.

b) Determine the I_{sh}^2 -signal

To determine the I_{sh}^2 -signal, the abc-co-ordinate values have to be transformed into $\alpha\beta$ -co-ordinate values. The transformation is:

$$i_{\alpha h} = i_{ah}, \tag{5.1}$$

$$i_{\beta h} = \frac{2}{\sqrt{3}}i_{bh} + \frac{1}{\sqrt{3}}i_{ah} \tag{5.2}$$

$$\text{and } I_{sh}^2 = i_{\alpha h}^2 + i_{\beta h}^2 = i_{ah}^2 + i_{qh}^2. \tag{5.3}$$

$i_{\alpha h}$ and $i_{\beta h}$ are determined by using analogue components as shown in Figure 5.7. I_{sh}^2 is then determined by using two analogue multipliers and an adding operational amplifier circuit as shown in Figure 5.8.

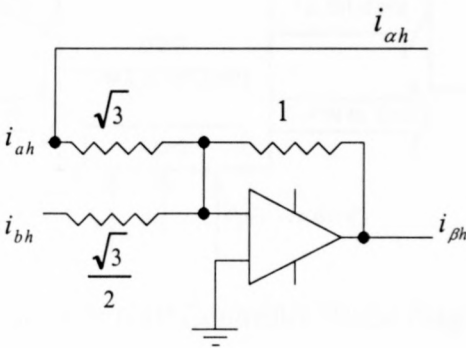


Figure 5.7: Circuit diagram for determining $i_{\alpha h}$ and $i_{\beta h}$

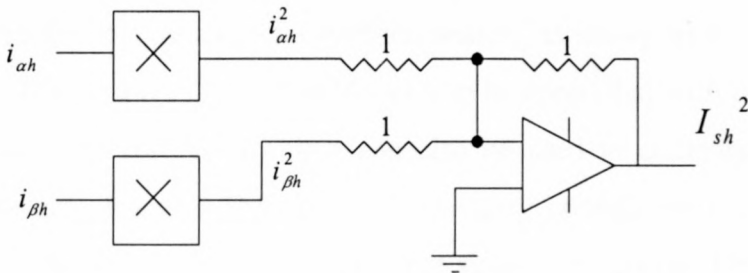


Figure 5.8: Circuit diagram for determining I_{sh}^2

5.2 DSP Control Card

A DSP Control card was developed for general purpose machine control. The TMS320F240 DSP from Texas Instruments is a device dedicated for electrical machine drive control because it has a build-in PWM generator. This DSP was chosen to serve as the main component on this card, assisted by the resolver circuitry and two DAC's. A block diagram of the DSP control card is shown in Figure 5.9 (see Appendix D for the circuit diagram).

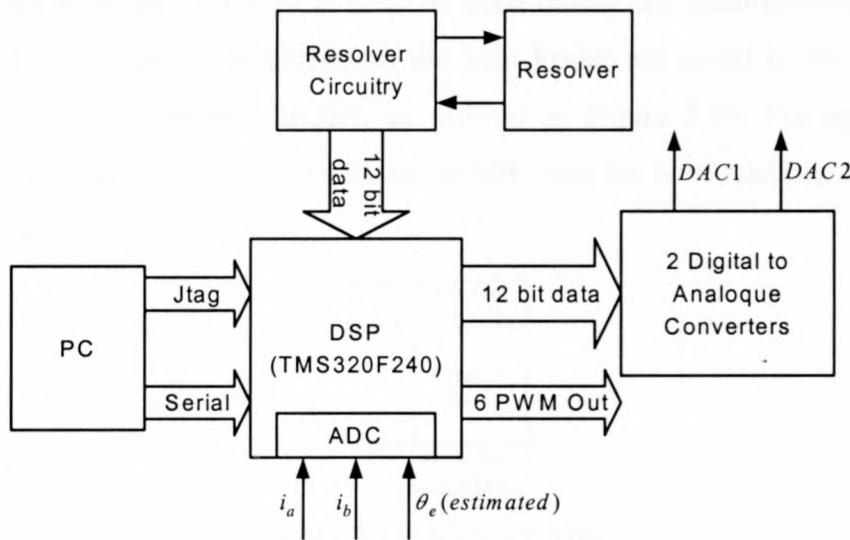


Figure 5.9: DSP Controller Block diagram.

5.2.1 Resolver circuitry

Although the system is developed and used for position sensorless control, a resolver and its circuitry are also included for position sensing as shown in the block diagram of Figure 5.9. This ensures that the RSM can also be controlled with position sensing via the resolver. The resolver's output can also be used to compare the estimated angle with the actual angle. The resolver's circuitry consists only of a sine wave oscillator and a resolver chip (RDC19220). The sine wave generated by the oscillator is fed to the resolver that is mounted on the rotor shaft. A signal is received back from the resolver that is compared with the original sine wave. With the comparison of these two signals, the resolver chip calculates the position and gives a 16 or 12 bit data output as a result. This output is fed to the data bus of the DSP.

5.2.2 Programming the DSP

Communication between the DSP and the PC is established by serial programming or by means of a JTAG communication port. To program the DSP with the JTAG an expensive interface between the DSP and the PC is needed. For serial programming only a serial cable and a serial port on the PC is needed. Therefore serial programming is much more viable. The only problem with serial programming is that there must be a communication protocol programmed into the DSP before downloading the code. This protocol is called the Serial Boot Loader and it can only be programmed with the JTAG, or it must be done during the manufacturing process. Once the DSP is serially programmed, the boot loader is saved in the top of the memory, starting at address 3E00H, as shown in Figure 5.10. For updating the program code, the DSP jumps to address 3E00H, runs the boot loader and programs the new code.

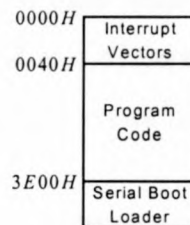


Figure 5.10: Memory Map

5.2.3 DACs, ADC and the PWM output

These are the remaining components on the DSP control board. Two 12 bit DACs are used to output the analogue quantities of digital values used in the DSP. It is now possible to display digital values in the DSP on an analogue oscilloscope. This is very useful for troubleshooting.

The TMS320F240 has two ADCs on board. These two ADCs are multiplexed with 16 IO pins on the DSP. Voltages and currents that are used in the control loop must be measured and transformed into digital quantities by the ADCs.

The DSP has three full-compare PWM units that are used for 3-phase PWM outputs. To generate the appropriate PWM outputs, the DSP is programmed for the desired switching frequency and the three reference values are programmed into three other

registers. With these three full-compare units the DSP generates the six signals for switching the inverter's switches, including the dead time between the top and bottom switches.

5.2.4 Control strategies

The RSM drive is under torque control and therefore the current of the machine has to be controlled. Two different current control strategies were used. These are explained in the following sections

a) Constant current angle control

With this type of control, maximum torque per ampere is always obtained. It has been shown that the optimum current angle for the transverse laminated RSM is about 65° . This means that the current control loop must keep the current angle (the angle between the current vector and the d-axis of the rotor) at 65° . To adjust the torque of the machine the amplitude of the current vector is changed.

To implement this control loop in the DSP (the C-code program is given in Appendix A), the rotor position, obtained from the resolver or the estimated angle, is used to generate the three reference signals, as shown in Figure 5.11. Two phase currents are measured, while the third one is calculated. These three currents are subtracted from the reference signals to get the error signals that are fed to the inverter. This control loop requires no transformations because all calculations are done in the abc-coordinate reference frame.

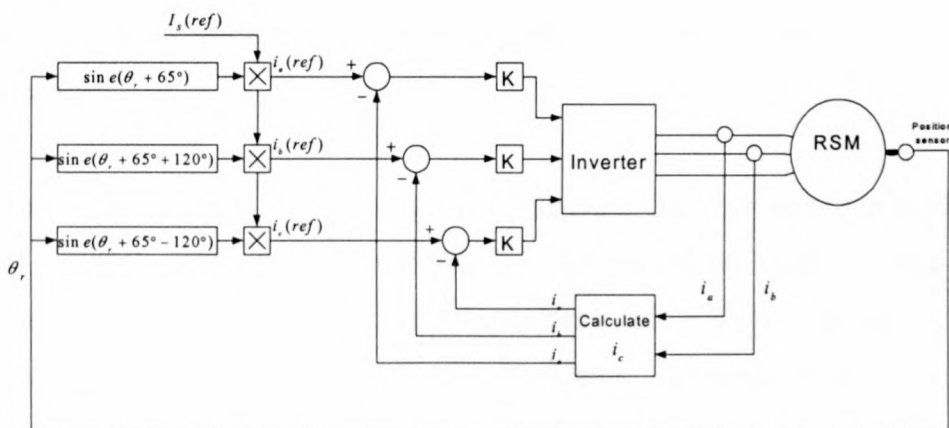


Figure 5.11: Block diagram of the Constant current angle controller.

b) Constant d-axis current control

With the constant d-axis current control, the magnetising current, i_d , is kept constant and i_q is controlled according to the torque command. With the dq reference values, $i_{d(ref)}$ and $i_{q(ref)}$, known, the measured currents have to be transformed to the dq-co-ordinate reference frame as shown in Figure 5.12. By subtracting these transformed values from the reference values, the error signals in the dq-co-ordinate reference frame are obtained. Again a transformation has to be done to generate the error signals in the abc-co-ordinate reference frame. These error signals are then fed to the inverter. The C-code DSP program is given in Appendix B.

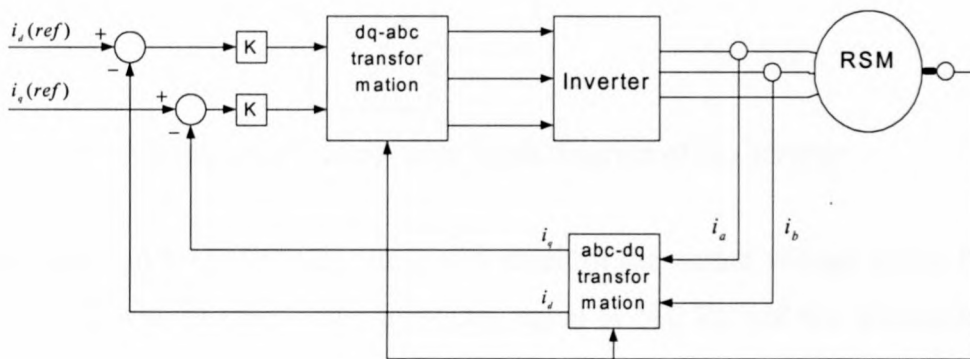


Figure 5.12: Block diagram of constant d-axis current control.

5.2.5 Synchronous sampling

In applying only the 610 Hz voltage signal to the stator of the RSM an unexpected waveform of the I_{sh}^2 -signal, what seemed to be a low frequency component together with the 610 Hz component, was experienced. However, after synchronising the sample frequency with the switching frequency, this low frequency component has disappeared.

To study this further, a simple simulation was done that represents the working of a digital controller and a single-phase inverter. The simulation block diagram is shown in Figure 5.13, and it was found that the simulation results showed the same results as was experienced in the practical situation. In Figure 5.13 a zero-order-hold (ZOH) is used to sample the sine wave reference signal. The output of the ZOH is compared with a triangular wave of which the frequency is equal to the switching frequency of

the inverter (5 kHz in this case). If the output of the comparison is positive (sine wave $>$ triangular wave), the “switch”-block in Figure 5.13 switches its output to a +400V dc supply. If the comparison is negative (sine wave $<$ triangular wave) the output is switched to a -400V dc supply. The switch thus, is a single-phase inverter with a 800V dc-bus voltage. The output of the “switch”-block is filtered by a low pass filter to reject the switching frequency and other harmonics except the fundamental.

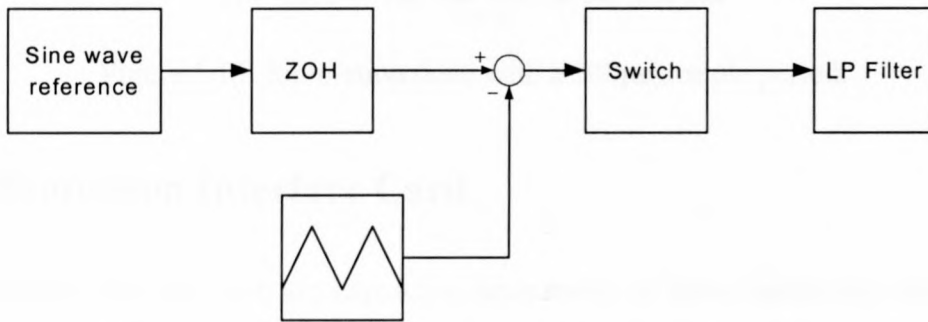


Figure 5.13: Simulation block diagram of the inverter

Figure 5.14 and 5.15 show the simulation result of the output voltage of the filter of Figure 5.13, with the sine wave frequency equal to 610 Hz and the triangular wave frequency (switching frequency) equal to 5 kHz (200 μs switching period). In Figure 5.14 the sample period of the ZOH is 60 μs and in Figure 5.15 it is 200 μs . Hence it is clear how the output becomes stable if the sample period is equal to the switching period. This shows the importance of synchronous sampling, meaning that the sample frequency must be equal to the switching frequency.

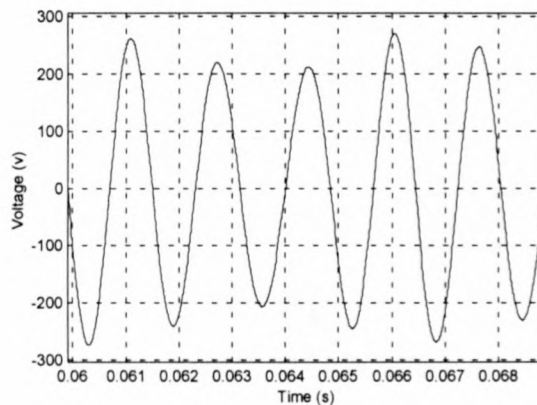


Figure 5.14: Simulation done with a 60 μs sample period.

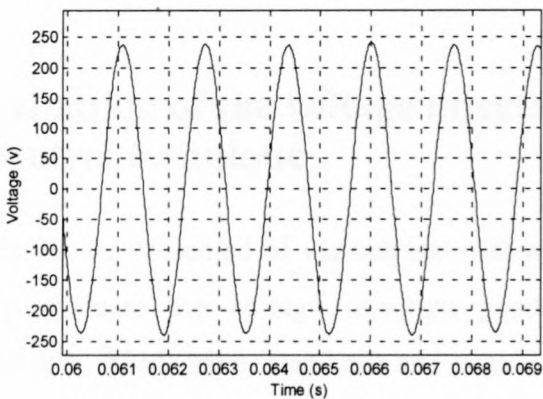


Figure 5.15: Simulation done with a 200 μ s sample period.

5.3 Protection Interface Card

The inverters that are used are expensive equipment, so these equipment have to be protected if the DSP controller fails. The main component on the protection interface card (see Figure 5.16) is an EPLD (Electronic Erasable Logic Device). This ensures that dead time can be programmed on this board. Figure 5.16 shows that four signals are measured and compared with reference values. The three-phase currents and the dc-bus voltage of the inverter are measured. If one of the three-phase currents exceeds a maximum, a fault (Trip) signal is set and all the IGBTs are switched-off by the EPLD. This ensures that the inverter and machine are protected against over current.

The protection board also monitors the dc-bus voltage for an over voltage condition. An over voltage condition can occur when the motor regenerates and there is a failure in the dynamic brake. In this case the IGBTs are also switched-off, protecting them against over voltage.

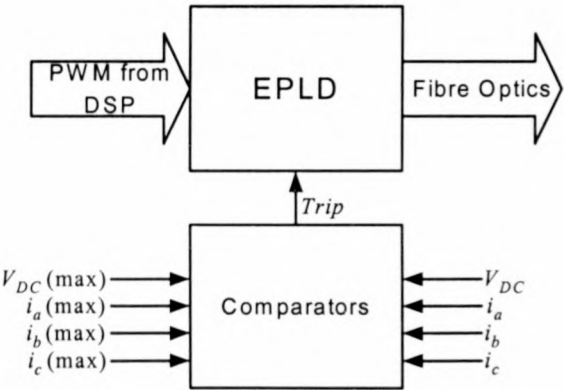


Figure 5.16: Block diagram of the protection interface

Chapter 6

6 Practical evaluation of the voltage injection position sensorless control technique

In this chapter the results are presented of various test that were done on both RSM drives to practically evaluate the voltage injection position sensorless control technique. On the 5.5 kW RSM drive, standstill and running tests were conducted comparing the estimated and actual positions. On the 110 kW RSM drive only a running test was conducted.

6.1 Practical evaluation on the 5.5 kW RSM drive

Consoli [10] used a 15 V high frequency voltage signal for estimating the rotor position. A 15 V, 610 Hz 3-phase voltage was applied to the stator of the 5.5 kW RSM and a maximum phase current of only 0.2 A_(peak-peak) was measured. The reduction ratio of the LEM current modules is 2500:1, and with the use of a 68Ω termination resistor, the input voltage to the 610 Hz bandpass filter is only 5.5 mV. This small voltages makes the measurement very noise susceptible. By increasing the amplitude of the high frequency voltage the high frequency current flowing in the stator increases and the current measurement becomes much less noise susceptible.

It was further found that for a dc-bus voltage of more than 300 V, the switching noise was becoming too much, and influencing the position estimation. Therefore a dc-bus of 300 V was used. The 300 V dc-bus has to supply the high frequency voltage and the normal power supply or working voltage. For the 5.5 kW RSM drive, 40V was used for the high frequency voltage supply. This voltage was large enough so that noise did not influence the measurement.

6.1.1 Standstill tests

With this test the rotor of the 5.5 kW RSM was clamped, and with a loadcell the generated torque was measured. The standstill tests were conducted for both constant d-axis current control and constant current angle control. Table 6.1 shows the results that were measured with constant d-axis current control. The I_d and I_q values in Table 6.1 are reference values that were used in the DSP and is not the actual d- and q- axis currents. The amplitude of the current vector, I_{sref} , is calculated from the dq current values. Table 6.2 shows the measured results using constant current angle control. Figure 6.1 shows the graphs of the measured results of Tables 6.1 and 6.2.

I_q	I_d	I_{sref}	T(sensor) (N-m)	T(sensorless) (N-m)
0	9	9	0	0
2	9	9.22	0.6	0.4
4	9	9.85	3	1.6
6	9	10.82	5	4
8	9	12.04	7	6.8
10	9	13.45	10	10
12	9	15	11.5	12
14	9	16.64	12	13
16	9	18.36	14.5	16
18	9	20.12	15.5	18
20	9	21.93	18.5	19
22	9	23.77	19	20
24	9	25.63	21	23
26	9	27.51	22	24
28	9	29.41	24	26

Table 6.1: Measured torque, with constant d-axis current control

I_{sref}	T(sensor) (N-m)	T(sensorless) (N-m)
0	0	0
1	0.4	1.6
2	1.8	6
3	6.8	10
4	11.5	14
5	16	18
6	20	22
7	24	26

Table 6.2: Measured torque with constant current angle control

Figure 6.1 shows that for the two different current control strategies there is in general a good agreement between the generated torque with sensor and sensorless control. One reason for the difference maybe is that the resolver's zero was not tuned exactly to the q-axis of the RSM. Secondly the slotted air-gap causes a huge torque ripple, which can also cause the difference in the two measurements. This could cause the estimated angle to be closer to the RSM q-axis than the resolver's output, causing the sensorless drive to produce more torque than the sensor drive. Further it is explained in Chapter 4 that cross magnetisation has an effect on the sensorless position estimation.

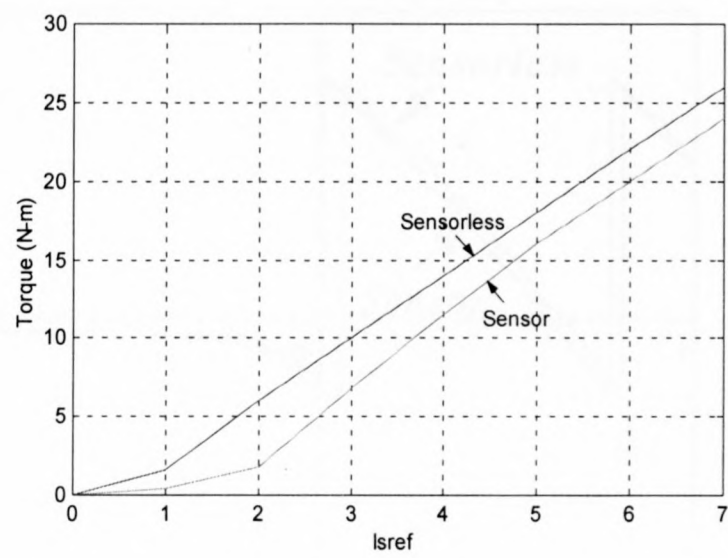


Figure 6.1a: Measured torque with constant current angle control

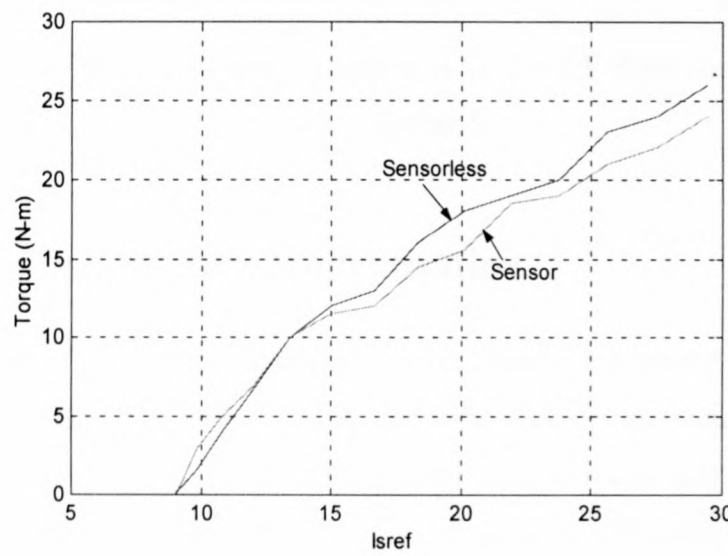


Figure 6.1b: Measured torque with constant d-axis current control

6.1.2 Acceleration from standstill

In Figure 6.2 the 5.5 kW RSM accelerates from zero speed. The figure shows the position measured by the resolver and the estimated position. The estimated position compares well with the resolver position except for the phase shift. The phase shift is because of cross magnetisation as discussed in Chapter 4.

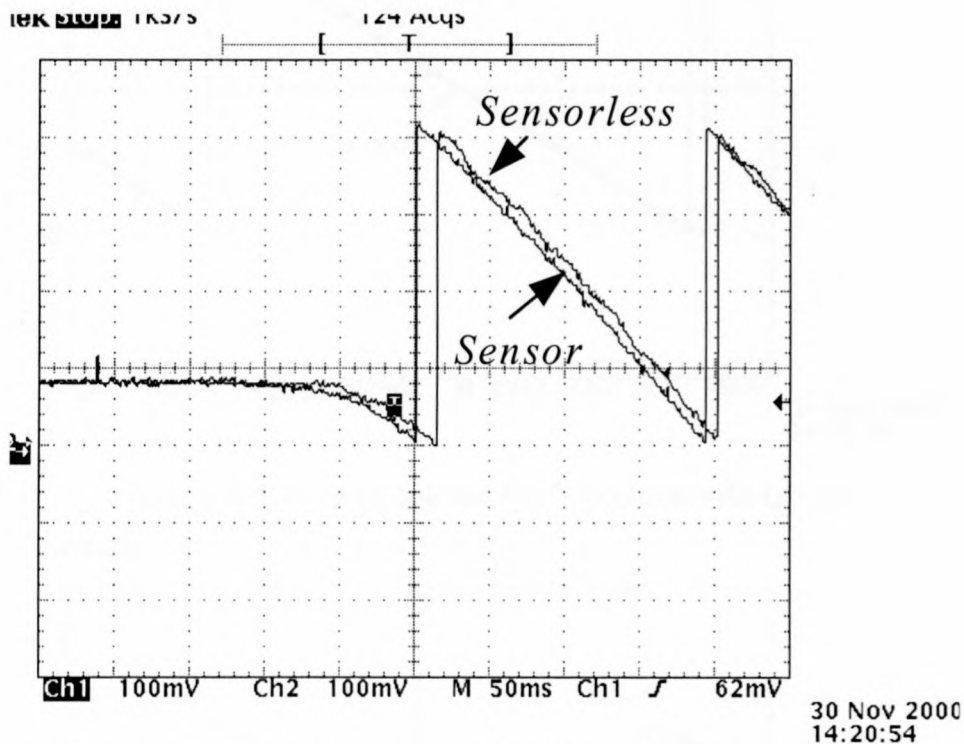


Figure 6.2: Resolver and estimated position of the 5.5 kW RSM accelerating from standstill

6.1.3 The effect of cross magnetisation

Figures 6.3 and 6.4 are measurements taken while the motor was controlled sensorless. In Figure 6.3, with $I_d = 1$ A, the two positions are almost the same. To observe the effect of cross magnetisation, the d-axis current must be increased as discussed in Chapter 4. In Figure 6.4, with $I_d = 3$ A, and it can clearly be seen that the difference between the two positions is more than in the first graph, confirming the simulations done in Section 4.2.2. The q-axis current was tuned so that the machine speeds were almost the same for the two cases.

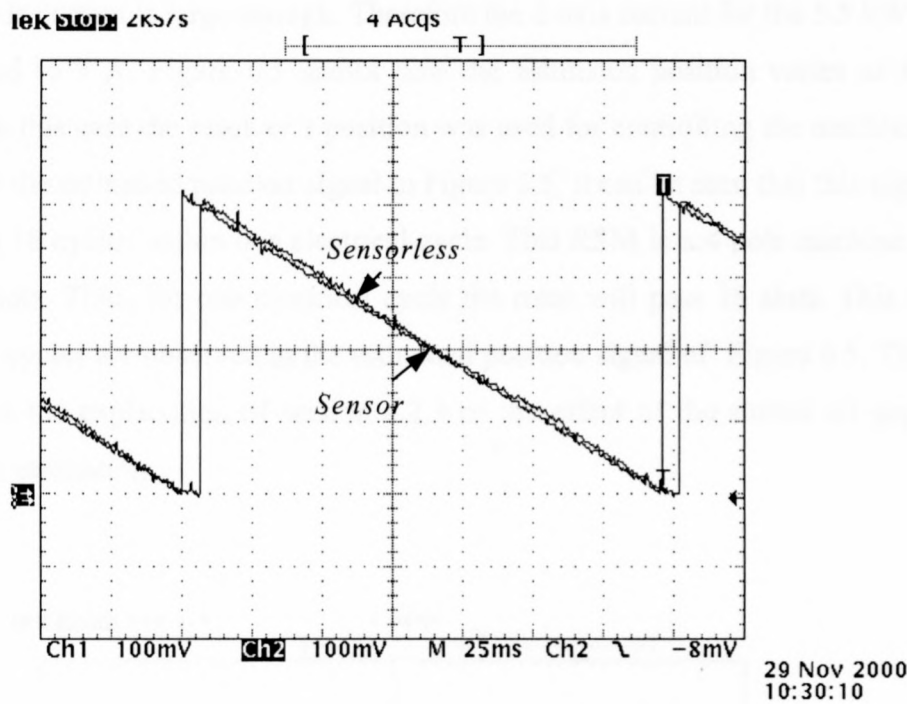


Figure 6.3: Estimated and resolver's position with $I_d = 1\text{ A}$

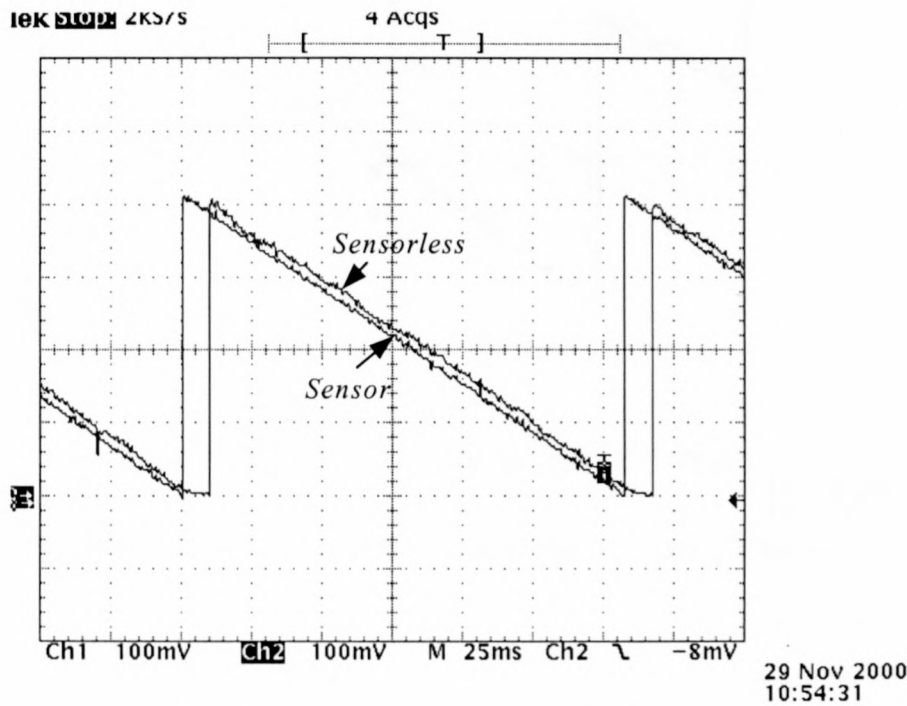


Figure 6.4: Estimated and resolver's position with $I_d = 3\text{ A}$

6.1.4 The effect of a slotted air-gap

In Chapter 4 the simulations showed that the effect of a slotted air-gap can be seen if the d-axis current is large enough. Therefore the d-axis current for the 5.5 kW RSM is increased to 7 A. Figure 6.5 shows how the estimated position varies as the rotor turns. In this case the resolver's position was used for controlling the machine. If one looks at the estimated position signal in Figure 6.5, it can be seen that this signal goes through 18 cycles within one electrical cycle. This RSM is a 4 pole machine with 36 stator slots. Thus, for one electrical cycle the rotor will pass 18 slots. This explains why 18 cycles are observed in the estimated position signal of Figure 6.5. This result confirms the explanation of section 4.2.3 of the effect of the slotted air-gap on the position estimation.

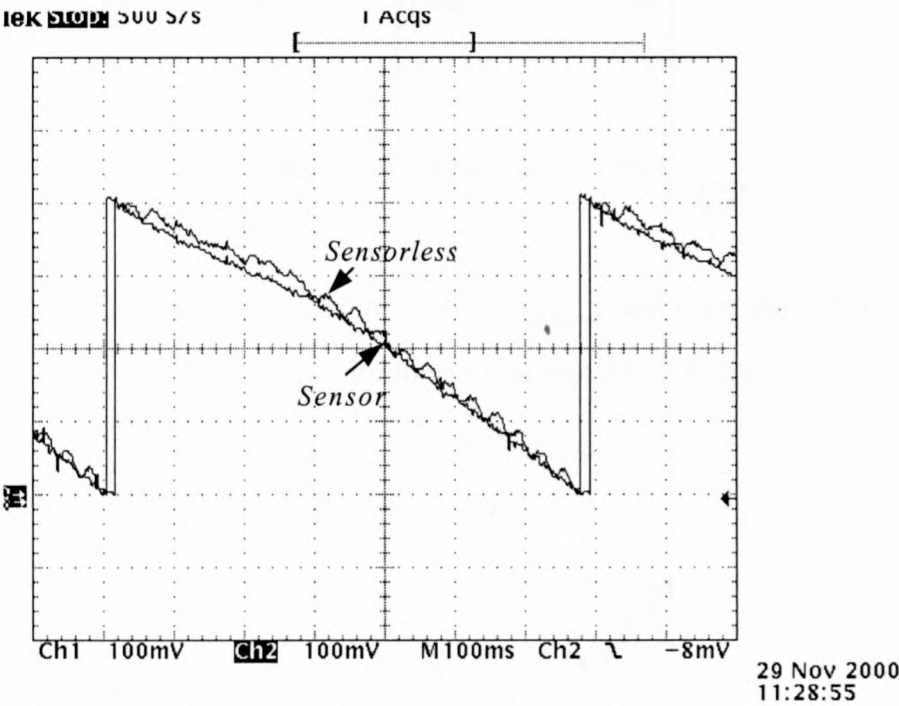


Figure 6.5: Estimated and resolver position with $I_d = 7\text{A}$ and I_q low

6.1.5 Position sensorless control using two different control strategies

In section 5.2.4 two different control strategies for the RSM drive were discussed namely the constant current angle and constant d-axis current control strategies. These two strategies were implemented together with the position sensorless control technique, and the measured results (phase A current and estimated position) are shown in Figures 6.6 and 6.7. In Figure 6.7 the current waveform seems to contain a lot of noise, but this is actually the 610 Hz high frequency current component.

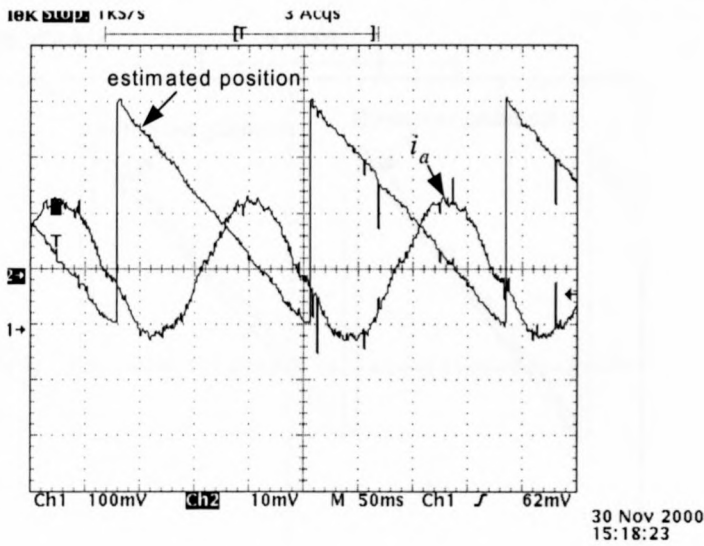


Figure 6.6 : Constant d-axis current control ($\theta_{estimated}$ and i_a are shown). The grid intervals for the current signal is 2 A/div

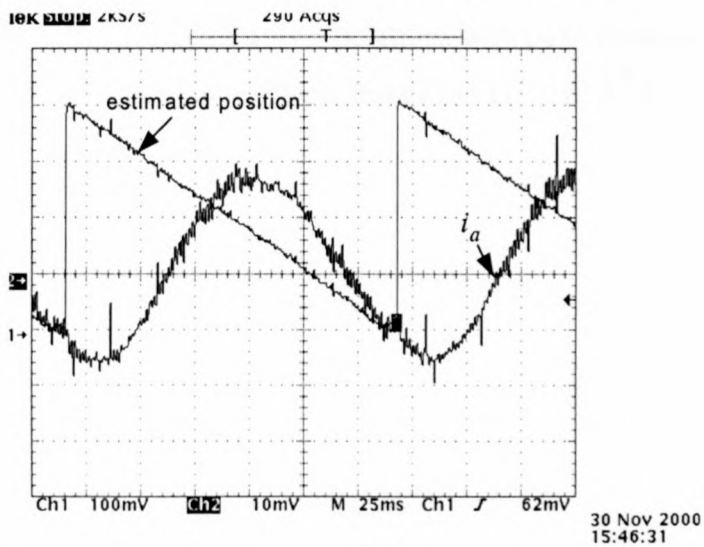


Figure 6.7 : Constant current angle control ($\theta_{estimated}$ and i_a are shown)). The grid intervals for the current signal is 0.5 A/div

6.2 Practical evaluation of the 110 kW RSM drive

The voltage injection technique was also implemented on the 110 kW RSM. For this drive system the dc-bus voltage is 900 v and a 60 V high frequency 3-phase voltage was applied to the stator of the RSM for position estimation. With position sensorless constant current angle control the result in Figure 6.8 was obtained. For this medium power drive good agreement is found between the estimated and actual positions, however, a phase shift between the two position signals is observed again.

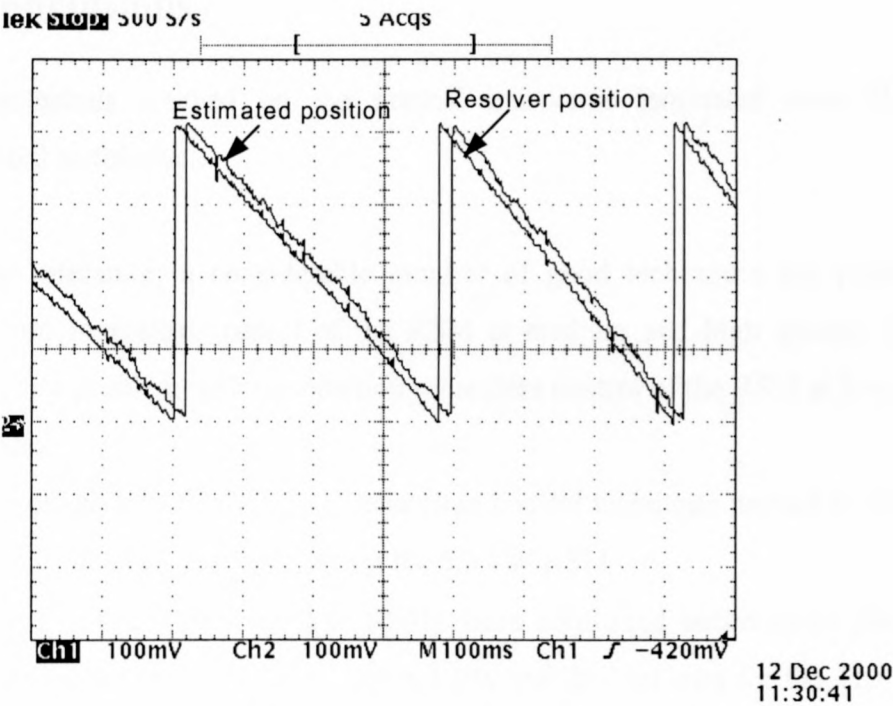


Figure 6.8 : The estimated and resolver positions with position sensorless constant current angle control of the 110 kW RSM

Chapter 7

7 Conclusions and recommendations

The conclusions reached are based on a literature study of the various position sensorless control techniques of the RSM and the investigation and implementation of one of these techniques, namely the so-called voltage injection technique. Recommendations are given to improve this specific technique.

7.1 Conclusions

The conclusions reached on the normal transverse laminated rotor RSM, are summarised as follows:

- In the literature, a considerable number of good techniques are proposed for position sensorless control of the RSM at medium and high speeds. However, there is a problem with the position sensorless control of the RSM at low and zero speeds.
- The voltage injection position sensorless control technique proved to work quite well at standstill as was shown on the 5.5 kW RSM.
- The 5.5 kW and the 110 kW RSMs were controlled successfully also at low speeds (about 500 rev/min for the 5.5 kW and 200 rev/min for the 110 kW) and low stator currents by using the voltage injection position sensorless technique. Therefore this technique proved to work at low speeds and low stator currents.
- In the literature the voltage injection technique is investigated by assuming the d- and q- axis inductances as constants. It is shown in this thesis that these inductances vary with the d- and q-axis currents, due to saturation. However the effect of saturation is shown to have no effect on the estimation of the rotor position.
- Cross magnetisation however, as shown, can cause a large error in estimating the rotor position. It is shown that the error becomes more as the current increases, especially the d-axis current.

- The slotted air-gap of the RSM together with the unskewed rotor, causes the position estimation to vary as the rotor rotates. This variation is about 15° for the 5.5 kW RSM
- The TMS320F240 DSP machine controller work well for general-purpose machine control. The rotor position can be determined much faster and more accurate with separate analogue and digital circuitry, that only supplies the estimated position to the DSP. Therefore a dedicated board was designed for estimating the rotor position.

7.2 Recommendations

The following recommendations are made with respect to the voltage injection position sensorless control technique of the transverse laminated and axially laminated rotor RSM:

- It is possible to compensate for the error in the position estimation caused by cross magnetisation. This error is constant if the stator currents are constants, or else, the error is a function of the d-and q-axis currents. Therefore, by measuring the currents and using this function, the error can be obtained and compensated for.
- The error in the position estimation, caused by the slotted air-gap is almost impossible to compensate for, but skewing the rotor should cause this error to become very small or even disappear. It should be noticed that the position estimation of the axially laminated rotor RSM is also effected by the slotted air-gap, but these rotors can not be skewed. Therefore it is still a problem to overcome.
- The hardware can be improved by designing very low noise filters so that the position estimation isn't effected by the switching noise of the inverter.

8 References

1. JJ Germishuysen – “*Comparative study of Reluctance Synchronous and Induction Machine Drives for Rail Traction*”, M.Sc.Eng dissertation, University of Stellenbosch, March 2000.
2. I. Boldea – “*Reluctance Synchronous Machines and Drives*”, Clarendon Press, Oxford, 1996.
3. AE Fitzgerald, C Kingsly and SD Umans – “*Electric Machinery*”, McGraw-Hill Book Company, London, 1992.
4. P. Vas – “*Sensorless Vector and Direct Torque Control*”, Oxford University Press, 1998.
5. S.K Jackson – “*An Investigation of Position Sensorless Control using a Medium Power Reluctance Synchronous Machine*”, M.Sc.Eng dissertation, University of Stellenbosch, March 1999.
6. S. Bolognani – “*Torque Angle Calculator for Sensorless Reluctance Machine Drives*”, EPE Firenze, pp4-013-4-017, 1991.
7. M.S. Arefeen, M. Ehsani and T.A Lipo – “*Sensorless Position Measurement in Synchronous Reluctance Motor*”, IEEE Trans on Power Electronics, Vol 9, pp 624-630, November 1994.
8. L Kreindler, A Testa, T.A Lipo – “*Position Sensorless Synchronous Reluctance Motor Drive using the Stator Phase Voltage Third Harmonic*”, Conference Record of IEEE IAS Annual Meeting, pp679-686, 1993.
9. A Consoli, C Cavallaro, G Scarcella, A Testa – “*Sensorless torque control of Syncrel motor drives*”, IEEE Transactions on Power Electronics, Vol. 15, No. 1, pp 28-35, January 2000.

10. A Consoli, F Russo, G Scarcella, A Testa – “*Low and zero speed sensorless control of synchronous reluctance motors*”, IEEE Transactions on Industrial Applications, Vol. 35, No. 5, pp 1050-1057, September 1999.
11. E Capecci, P Guglielmi, M Pastorelli, A Vagati – “*Position sensorless control of transverse-laminated synchronous reluctance motors*”, IEEE Transactions on Industrial Applications, October 2000.
12. Jun Hu and Bin Wu – “*New Integration Algorithms for Estimating Motor Flux over a Wide Speed Range*”, IEEE Transactions on Power Electronics, Vol. 13 No. 5, pp 969-977, September 1998.
13. MJ Kamper, AT Mackay – “*Optimum control of the reluctance synchronous machine with a cageless flux-barrier rotor*”, Transactions of the South African Institute of Electrical Engineers, Vol. 86, No. 2, June 1995, pp. 49-56.
14. MJ Kamper, RA Trubenbach – “*Vector control and performance of a reluctance synchronous machine with flux barrier rotor*”, ICEM September 1992, pp 547-551.
15. D Miljavec, P Jereb – “*Can a reluctance synchronous motor be compared with a induction motor?*”, Industrial Applications in Power Systems, Computer Science and Telecommunications Proceedings of the Mediterranean Conference – MELCON Vol. 1, 1996, pp. 317-320.
16. MJ Kamper, FS Van der Merwe, S Williamson – “*Direct finite element design optimization of the cageless reluctance synchronous machine*”, IEEE Transactions on Energy Conversion Vol. 11, No. 3, September 1996, pp. 547-555.
17. A Vagati, M Pastorelli, F Scapino, G Franceschini – “*Impact of cross saturation in Synchronous Reluctance Motors or the transverse-laminated type*”, IEEE Transactions on Industrial Applications, Vol. 36, No. 4, July/August 2000, pp 1039-1045.

18. MJ Kamper, AF Volschenk – “*Effect of rotor dimensions and cross magnetisation on L_d and L_q inductances of reluctance synchronous machine with cageless flux barrier rotor*”, IEE Proc.-Electr. Power Appl., Vol. 141, No. 4, July 1994, pp .
19. TMS320 DSP Development Support, Digital Signal Processing Solutions, 1997.
20. JTAG/MPSD Emulation, Technical Reference, 1994.
21. Clarke and Park transformation on the TMS320C2xx, Application Report, Literature Number: BPRA048, 1997.
22. TMS320C24x DSP Controllers, Peripheral Library and Specific Devices, Reference Set, Digital Signal Processing Solutions, 1997.
23. TMS320C240, TMS320F240 DSP Controllers, Data Sheets, 1997.
24. TMS320F20x/F24x DSP Embedded Flash Memory, Technical Reference, Literature Number SPRU282, September 1998.
25. TMS320C2xx User’s Guide, Literature Number SPRU127B, January 1997.
26. A. Vagati and T.A Lipo – “*Synchronous Reluctance Motors and Drives: A New Alternative*,” IEEE Industry Applications Society Tutorial Course, 94TH8018, 1994.
27. λ_d and λ_q data of the 5.5 kW RSM obtained with the finite element method by M.J Kamper.

Appendix A

C-code for constant current angle control


```

/*****
/* RSM control program, tested without load, with 11kVA */
/* Inverter and 50A 1:1000 LEM modules */
/* Remember to include table2.obj in RUN.CMD */
*****/
#include "math.h"
#include "F240.h"

volatile unsigned int *T1CON = (volatile unsigned int *) 0x7404;
volatile unsigned int *T2CON = (volatile unsigned int *) 0x7408;
volatile unsigned int *ACTR = (volatile unsigned int *) 0x7413;
volatile unsigned int *DBTCN = (volatile unsigned int *) 0x7415;
volatile unsigned int *COMPR1 = (volatile unsigned int *) 0x7417;
volatile unsigned int *COMPR2 = (volatile unsigned int *) 0x7418;
volatile unsigned int *COMPR3 = (volatile unsigned int *) 0x7419;
volatile unsigned int *COMCON = (volatile unsigned int *) 0x7411;
volatile unsigned int *GPTCON = (volatile unsigned int *) 0x7400;
volatile unsigned int *Dataout = (volatile unsigned int *) 0x8000;
volatile unsigned int *Datain = (volatile unsigned int *) 0x8001;
volatile unsigned int *EVIMRA = (volatile unsigned int *) 0x742C;
volatile unsigned int *SCMPR1 = (volatile unsigned int *) 0x741A;
volatile unsigned int *SACTR = (volatile unsigned int *) 0x7414;
int i, k, ia, ib, ic, afset, refa, refb, refc, posisie, temp, torch;
int hoeka, hoekb, hoekc, test;
int hoek1, hoek2, hoek3;
int refha, refhb, refhc;
int cmp1, cmp2, cmp3;
int Hoek, n, Hoekold, Hoeknew, Speed, posisieold;
int Hoekest, temp;
extern int sine();

main()
{
    *EVIMRA |= 0x0001;

    ADCTRL2 -> ADCPSCALE = 0; /* Prescale value = 0 */
    ADCTRL2 -> ADCEVSOC = 0;
    ADCTRL2 -> ADCEXTSOC = 0;

    ADCTRL1 -> ADCIMSTART = 0;
    ADCTRL1 -> ADCINTEN = 0; /* disable interrupt */
    ADCTRL1 -> ADCCRNRUN = 0; /* single conversion */
    ADCTRL1 -> ADC2EN = 1; /* en/dis(0)-able ADC2 */
    ADCTRL1 -> ADC1EN = 1; /* enable ADC1 */

    ADCTRL1 -> suspend_free = 0; /* */
    ADCTRL1 -> suspend_soft = 1; /* complete conversion before halting */

    *OCRA = 0x0FFFF; /* Stel ADCIN0-1 aktief */
    *SYSCR &= 0xFF3F; /* Maak IOPC1 'n IO Pin */

    *PCDATDIR = 0x0303; /* Maak IOPC1(FREEZE) = 1 */
    *PCDATDIR &= 0xFFFD; /* Maak IOPC1(FREEZE) = 0 */
    *PCDATDIR &= 0xFFFE; /* Maak IOPC0(ENABLE) = 0 */
    i = *Datain;
    *PCDATDIR = 0x0303; /* Maak IOPC1(FREEZE) = 1 */
                      /* Maak IOPC0(ENABLE) = 1 */

```

```

*PCDATDIR |= 0xC0C0;

afset = i>>4;
afset &= 0x0FFF;
*ACTR = 0x0666; /* Maak PWM pin Aktief hoog en enkel
tweede Aktief laag */
*SACTR = 0x002A;
*DBTCN = 0x78E7;
*T1PR = 0x800; /* f = 4,88kHz */
*COMCN = 0x0387;
*COMCN = 0x8387;
*T1CNT = 0x0;

*T1CN = 0x0A802;
*T1CN = 0x0A842;

*T2PR = 4095;
*T2CN = 0x9302;
*T2CN = 0x9342;

*SCMPR1 = 2048;
n = 0;
for(;;)
{
while (*T1CNT>5)
{

*PCDATDIR &= 0xFFFD; /* Maak IOPC1(FREEZE) = 0 */
*PCDATDIR &= 0xFFFE; /* Maak IOPC0(ENABLE) = 0 */
posisie = *Datain;
*PCDATDIR |= 0x0303; /* Maak IOPC1(FREEZE) = 1 */
/* Maak IOPC0(ENABLE) = 1 */

ADCTRL1 -> ADC1CHSEL = 7;
ADCTRL1 -> ADC2CHSEL = 7;
ADCTRL1 -> ADCSOC = 1;
while (ADCTRL1 -> ADCINTFLAG == 0);
ADCTRL1 -> ADCINTFLAG = 1;
i = *ADCFIFO1; /* Groen draad */
ia = i>>6;
ia &= 0x03FF;
i = *ADCFIFO2; /* Geel draad */
ib = i>>6;
ib &= 0x03FF;

ADCTRL1 -> ADC2CHSEL = 0;
ADCTRL1 -> ADCSOC = 1;
while (ADCTRL1 -> ADCINTFLAG == 0);
ADCTRL1 -> ADCINTFLAG = 1;
i = *ADCFIFO2;
torch = i>>6;
torch &= 0x03FF;
torch = torch/64; /* Getal tussen 0 - 16 */

ADCTRL1 -> ADC2CHSEL = 5;

```

```

ADCTRL1 -> ADCSOC = 1;
while (ADCTRL1 -> ADCINTFLAG == 0);
    ADCTRL1 -> ADCINTFLAG = 1;
i = *ADCFIFO2;
Hoek = i>>6;
Hoek &= 0x03FF;

posisie = posisie>>4;
posisie &= 0x0FFF;
posisie = 2*posisie; /* Met Resolver */
if (posisie>4095)
    {posisie = posisie - 4095;}
n = n + 1;
if (n==7)
    {Spoed = posisie - posisieold;
    posisieold = posisie;
    Spoed = Spoed/8;
    n = 0;}

Hoekest = 4.95*Hoek;

/* Hoekest = Hoekest+Spoed; */
/* test = Hoekold + 4*Spoed; */
/*if (Hoek>test) */
/* { Hoekest = Hoek;} */
/* Hoekold = Hoek; */

Hoekest = Hoekest + 0;
if (Hoekest>4095)
    {Hoekest = Hoekest - 4095;}

ia = -4*(ia-512);
ib = -4*(ib-512);
ic = -ia - ib;

hoeka = posisie; /* Sensorloos */
if (hoeka>4095)
    { hoeka = hoeka-4095;}

hoek1 = *T2CNT;
hoek2 = hoek1 + 1365;
    if (hoek2>4095)
        {hoek2 = hoek2 - 4095;}
hoek3 = hoek1 + 2730;
    if (hoek3>4095)
        {hoek3 = hoek3 - 4095;}

refha = sine(hoek1)/16;
refhb = sine(hoek2)/16;
refhc = sine(hoek3)/16;

hoeka = hoeka-740; /* Q-as op Magnetiese A-as */
    if (hoeka<0)
        { hoeka = hoeka + 4095;}

```



```

hoekb = hoeka + 1365;
    if (hoekb>4095)
        { hoekb = hoekb - 4095;}

hoekc = hoeka + 2730;
    if (hoekc>4095)
        { hoekc = hoekc - 4095;}

refa = torch*(sine(hoeka)/64); /* getal tussen -2047 -
2047 */

    temp = 4*(refa-ia);
    if (temp>896)
        {cmpr1 = 896;
        goto J1;}
    if (temp<-896)
        {cmpr1 = -896;}
    else
        {cmpr1 = temp;}

J1:
*COMPR1 = cmpr1+refha + 1024;

test = *COMPR1;
refb = torch*(sine(hoekb)/64);

    temp = 4*(refb-ib);      /* K = 4 */
    if (temp>896)
        {cmpr2 = 896;
        goto J2;}
    if (temp<-896)
        {cmpr2 = -896;}
    else
        {cmpr2 = temp;}

J2:
*COMPR2 = cmpr2+refhb + 1024;

refc = torch*(sine(hoekc)/64);

    temp = 4*(refc-ic) ;
    if (temp>896)
        {cmpr3 = 896;
        goto J3;}
    if (temp<-896)
        {cmpr3 = -896;}
    else
        {cmpr3 = temp;}

J3:
*COMPR3 = cmpr3+refhc + 1024;

*PCDATDIR &= 0xFF7F;    /*DAC1*/
*Dataout = Hoekest;
*PCDATDIR |= 0x0080;

*PCDATDIR &= 0xFFBF;    /*DAC2*/

```

```
*Dataout = posisie;  
*PCDATDIR |= 0x0040;
```

```
}
```

```
}
```

Appendix B

C-code for constant d-axis current control


```

/*****
/* RSM control program, tested without load, with 11kVA */
/* Inverter and 50A 1:1000 LEM modules */
/* Remember to include table2.obj in RUN.CMD */
*****/
#include "math.h"
#include "F240.h"

volatile unsigned int *T1CON = (volatile unsigned int *) 0x7404;
volatile unsigned int *T2CON = (volatile unsigned int *) 0x7408;
volatile unsigned int *ACTR = (volatile unsigned int *) 0x7413;
volatile unsigned int *DBTCN = (volatile unsigned int *) 0x7415;
volatile unsigned int *COMPR1 = (volatile unsigned int *) 0x7417;
volatile unsigned int *COMPR2 = (volatile unsigned int *) 0x7418;
volatile unsigned int *COMPR3 = (volatile unsigned int *) 0x7419;
volatile unsigned int *COMCON = (volatile unsigned int *) 0x7411;
volatile unsigned int *GPTCON = (volatile unsigned int *) 0x7400;
volatile unsigned int *Dataout = (volatile unsigned int *) 0x8000;
volatile unsigned int *Datain = (volatile unsigned int *) 0x8001;
volatile unsigned int *EVIMRA = (volatile unsigned int *) 0x742C;
volatile unsigned int *SCMPR1 = (volatile unsigned int *) 0x741A;
volatile unsigned int *SACTR = (volatile unsigned int *) 0x7414;
int i, k, ia, ib, ic, afset, refa, refb, refc, posisie, temp, torch;
int hoeka, hoekb, hoekc, test;
int hoek1, hoek2, hoek3;
int refha, refhb, refhc;
int cmp1, cmp2, cmp3;
int Hoek, n, Hoekold, Hoeknew, Speed, posisieold;
int Hoekest, temp;
int the, thec, the12n, the12nc, the12p, the12pc;
int idref, iqref;
int idmeas, iqmeas;
int iderr, iqerr;
int erra, errb, errc;
int meas1, meas2;
int teller;
extern int sine();

main()
{
*EVIMRA |= 0x0001;

ADCTRL2 -> ADCPSCALE = 0; /* Prescale value = 0 */
ADCTRL2 -> ADCEVSOC = 0;
ADCTRL2 -> ADCEXTSOC = 0;

ADCTRL1 -> ADCIMSTART = 0;
ADCTRL1 -> ADCINTEN = 0; /* disable interrupt */
ADCTRL1 -> ADCCONRUN = 0; /* single conversion */
ADCTRL1 -> ADC2EN = 1; /* en/dis(0)-able ADC2 */
ADCTRL1 -> ADC1EN = 1; /* enable ADC1 */

ADCTRL1 -> suspend_free = 0; /* */
ADCTRL1 -> suspend_soft = 1; /* complete conversion before halting */

*OCRA = 0x0FFFF; /* Stel ADCIN0-1 aktief */
*SYSCR &= 0xFF3F; /* Maak IOPC1 'n IO Pin */

```

```

*PCDATDIR = 0x0303; /* Maak IOPC1(FREEZE) = 1 */
*PCDATDIR &= 0xFFFD; /* Maak IOPC1(FREEZE) = 0 */
*PCDATDIR &= 0xFFFE; /* Maak IOPC0(ENABLE) = 0 */
i = *Datain;
*PCDATDIR = 0x0303; /* Maak IOPC1(FREEZE) = 1 */
/* Maak IOPC0(ENABLE) = 1 */
*PCDATDIR |= 0xC0C0;

afset = i>>4;
afset &= 0x0FFF;
*ACTR = 0x0666; /* Maak PWM pin Aktief hoog en enkel
tweede Aktief laag */
*SACTR = 0x002A;

*T1PR = 0x800; /* f = 4,88kHz */
*COMCON = 0x0387;
*COMCON = 0x8387;
*T1CNT = 0x0;

*T1CON = 0x0A802;
*T1CON = 0x0A842;

*T2PR = 4095;
*T2CON = 0x9302;
*T2CON = 0x9342;

*SCMPR1 = 2048;
n = 0;
teller = 0;
for(;;)
{
while (*T1CNT>5)
{

*PCDATDIR &= 0xFFFD; /* Maak IOPC1(FREEZE) = 0 */
*PCDATDIR &= 0xFFFE; /* Maak IOPC0(ENABLE) = 0 */
posisie = *Datain;
*PCDATDIR |= 0x0303; /* Maak IOPC1(FREEZE) = 1 */
/* Maak IOPC0(ENABLE) = 1 */

ADCTRL1 -> ADC1CHSEL = 7;
ADCTRL1 -> ADC2CHSEL = 7;
ADCTRL1 -> ADCSOC = 1;
while (ADCTRL1 -> ADCINTFLAG == 0);
ADCTRL1 -> ADCINTFLAG = 1;
i = *ADCFIFO1; /* Groen draad */
ia = i>>6;
ia &= 0x03FF;
i = *ADCFIFO2; /* Geel draad */
ib = i>>6;
ib &= 0x03FF;

ADCTRL1 -> ADC2CHSEL = 0;

```

```

ADCTRL1 -> ADCSOC = 1;
while (ADCTRL1 -> ADCINTFLAG == 0);
    ADCTRL1 -> ADCINTFLAG = 1;
i = *ADC_FIFO2;
torch = i>>6;
torch &= 0x03FF;
torch = torch/64; /* Getal tussen 0 - 16 */

ADCTRL1 -> ADC2CHSEL = 5;
ADCTRL1 -> ADCSOC = 1;
while (ADCTRL1 -> ADCINTFLAG == 0);
    ADCTRL1 -> ADCINTFLAG = 1;
i = *ADC_FIFO2;
Hoek = i>>6;
Hoek &= 0x03FF;

posisie = posisie>>4;
posisie &= 0x0FFF;
posisie = 2*posisie; /* Met Resolver */
if (posisie>4095)
    {posisie = posisie - 4095;}
n = n + 1;
if (n==7)
    {Spoed = posisie - posisieold;
    posisieold = posisie;
    Spoed = Spoed/8;
    n = 0;}

Hoek = 4.95*Hoek;
if (Hoek>4095)
    {Hoek = Hoek - 4095;}

Hoekest = Hoek;

/*Hoekest = Hoekest+Spoed; */
/*test = Hoekold + 4*Spoed; */
/*if (Hoek>test) */
/*      { Hoekest = Hoek;} */
/*Hoekold = Hoek; */

ia = -1*(ia-512)/8; /* 16 A max */
ib = -1*(ib-512)/8;
ic = -ia - ib;

the = Hoekest;
thec = the + 1023;
if (thec>4095)
    {thec=thec-4095;}
the12n = the - 1365;
if (the12n<0)
    {the12n = the12n + 4095;}
the12p = the + 1365;
if (the12p>4095)
    {the12p = the12p-4095;}
the12nc = the - 1365 + 1023;
if (the12nc<0)

```



```

        {the12nc = the12nc+4095;}

the12pc = the + 1365 + 1023;
if (the12pc>4095)
    {the12pc=the12pc-4095;}

idref = 2; /* 64-volstroom 18 = 10 A */
iqref = -2*torch;

iqmeas = (ia*(sine(thec)/4))/512 +
(ib*(sine(the12pc)/4))/512 + (ic*(sine(the12nc)/4))/512;
idmeas = (ia*(sine(the)/4))/512 + (ib*(sine(the12p)/4))/512
+ (ic*(sine(the12n)/4))/512;

iqmeas = (2*iqmeas)/3;
idmeas = (2*idmeas)/3;

iderr = idref - idmeas/4;
iqerr = iqref - iqmeas/4;

erra = (iqerr*(sine(thec)/4))/512 +
(iderr*(sine(the)/4))/512;
errb = (iqerr*(sine(the12pc)/4))/512 +
(iderr*(sine(the12p)/4))/512;
errc = (iqerr*(sine(the12nc)/4))/512 +
(iderr*(sine(the12n)/4))/512;
erra = 8*erra;
errb = 8*errb;
errc = 8*errc;

hoek1 = *T2CNT;
hoek2 = hoek1 + 1365;
    if (hoek2>4095)
        {hoek2 = hoek2 - 4095;}
hoek3 = hoek1 + 2730;
    if (hoek3>4095)
        {hoek3 = hoek3 - 4095;}

refha = sine(hoek1)/16;
refhb = sine(hoek2)/16;
refhc = sine(hoek3)/16;

refa = torch*(sine(hoeka)/64); /* getal tussen -2047 -
2047 */

temp = erra;
if (temp>896)
    {cmpr1 = 896;
    goto J1;}
if (temp<-896)
    {cmpr1 = -896;}
else
    {cmpr1 = temp;}

J1:
*COMPR1 = cmpr1+refha + 1024;

```

```

test = *COMPR1;
refb = torch*(sine(hoekb)/64);

```

```

    temp = errb;
    if (temp>896)
        {cmpr2 = 896;
         goto J2;}
    if (temp<-896)
        {cmpr2 = -896;}
    else
        {cmpr2 = temp;}

```

```

J2:
*COMPR2 = cmpr2+refhb + 1024;

```

```

refc = torch*(sine(hoekc)/64);

```

```

    temp = errc;
    if (temp>896)
        {cmpr3 = 896;
         goto J3;}
    if (temp<-896)
        {cmpr3 = -896;}
    else
        {cmpr3 = temp;}

```

```

J3:
*COMPR3 = cmpr3+refhc + 1024;

```

```

*PCDATDIR &= 0xFF7F;    /*DAC1*/
*Dataout = Hoekest;
*PCDATDIR |= 0x0080;

*PCDATDIR &= 0xFFBF;    /*DAC2*/
*Dataout = posisie;
*PCDATDIR |= 0x0040;

```

```

}

```

```

}

```

Appendix C

**Schematic diagram of Measurement and Position Estimation
Card**

1

2

3

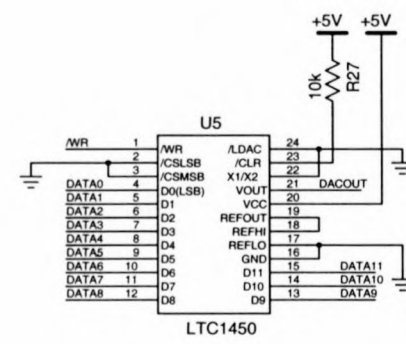
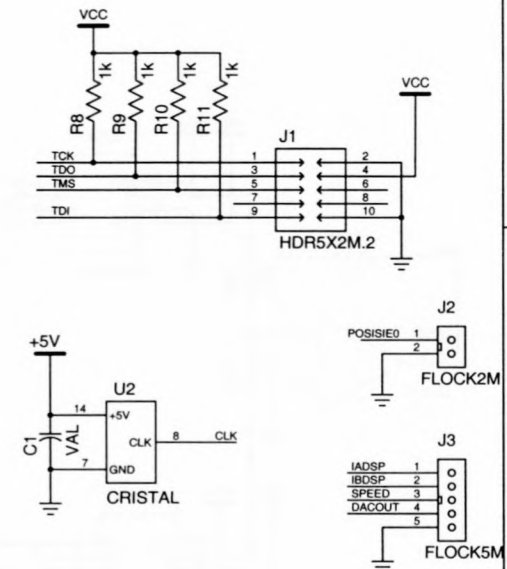
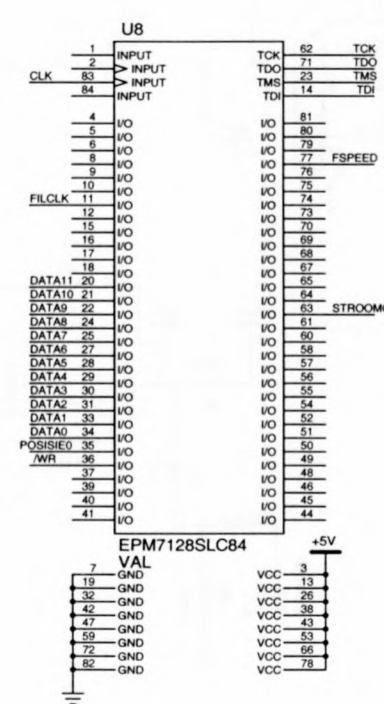
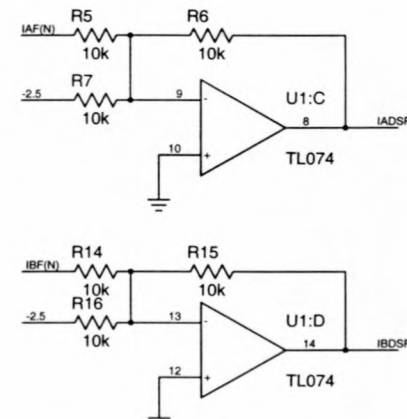
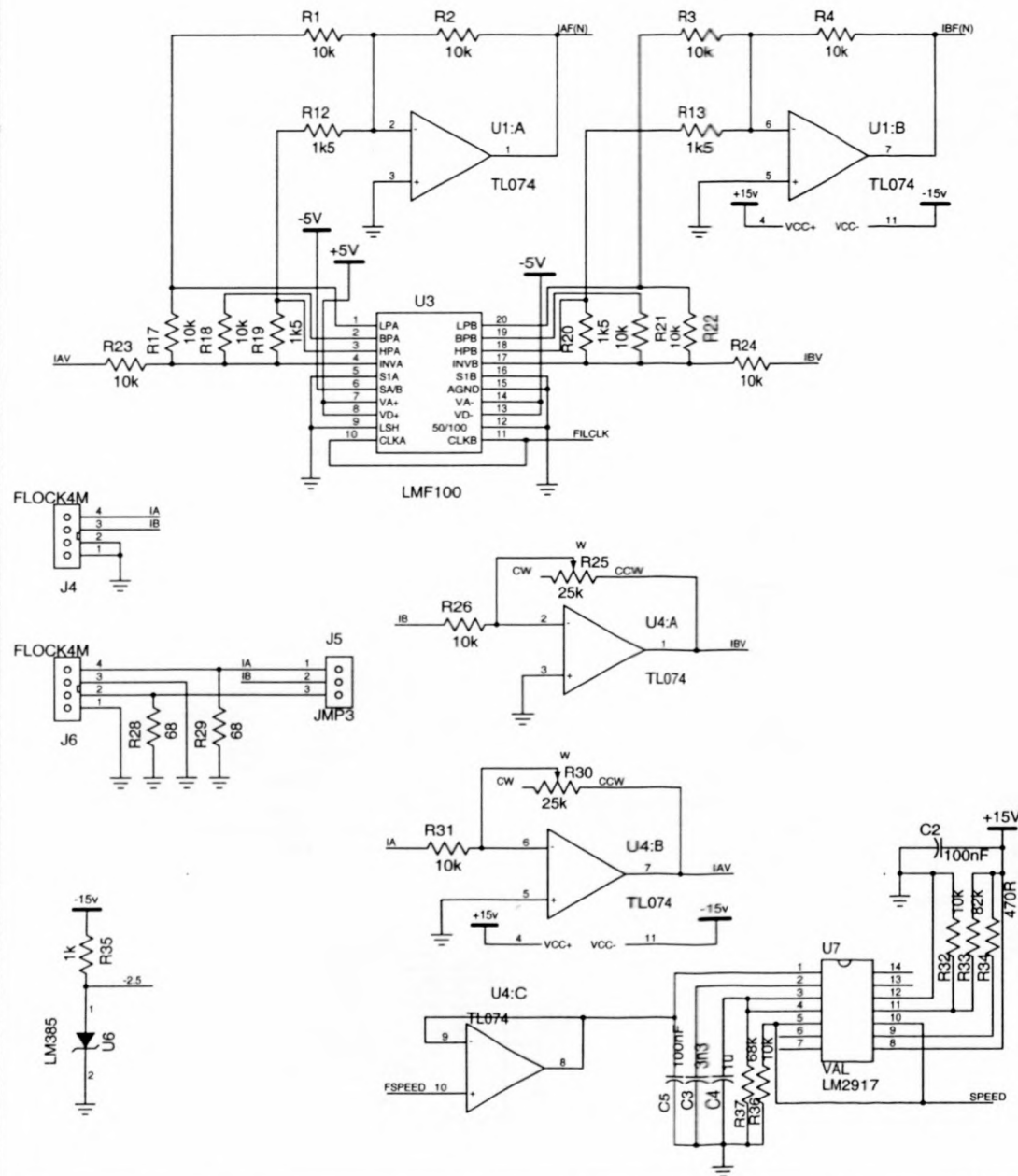
4

1

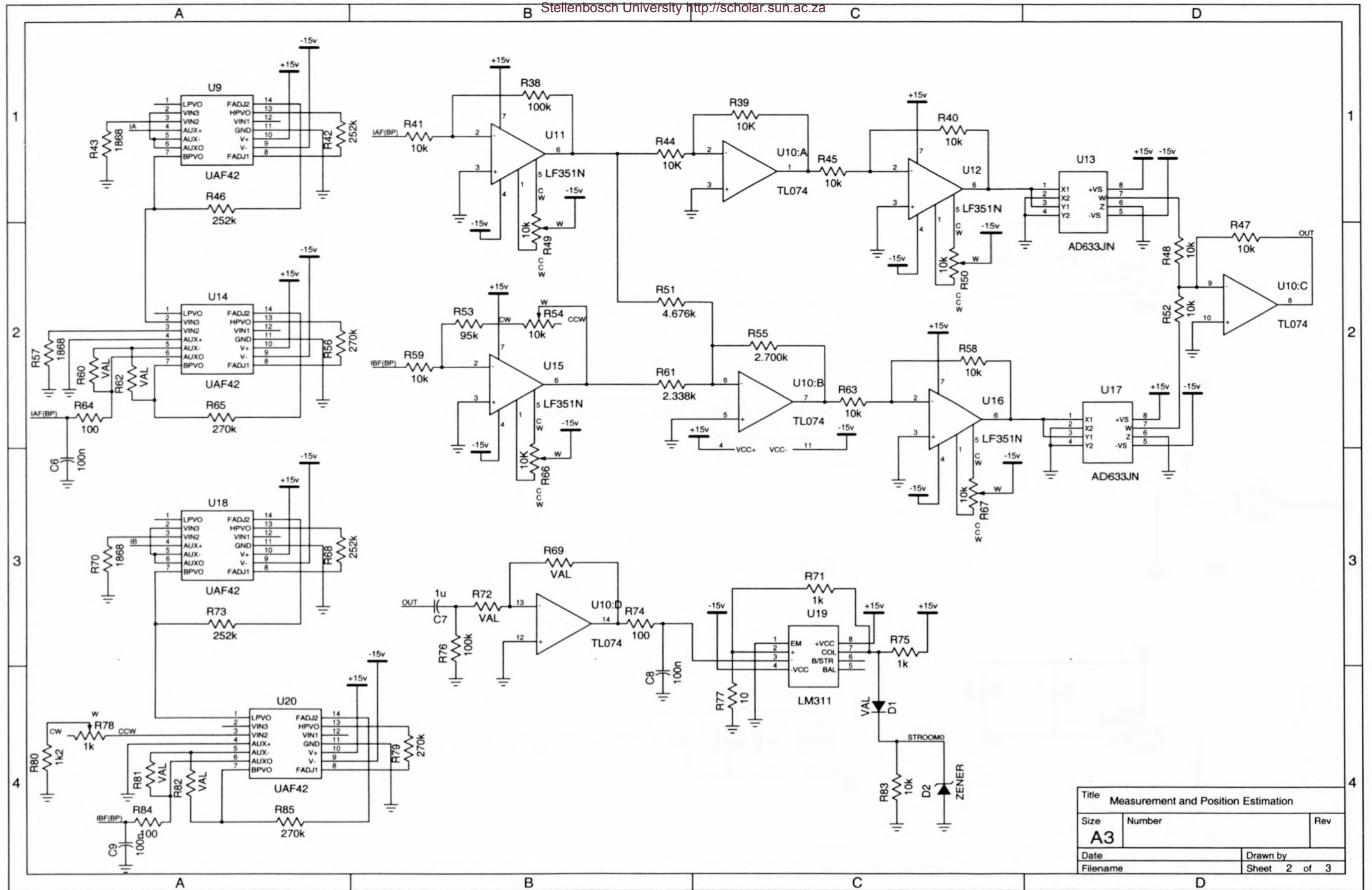
2

3

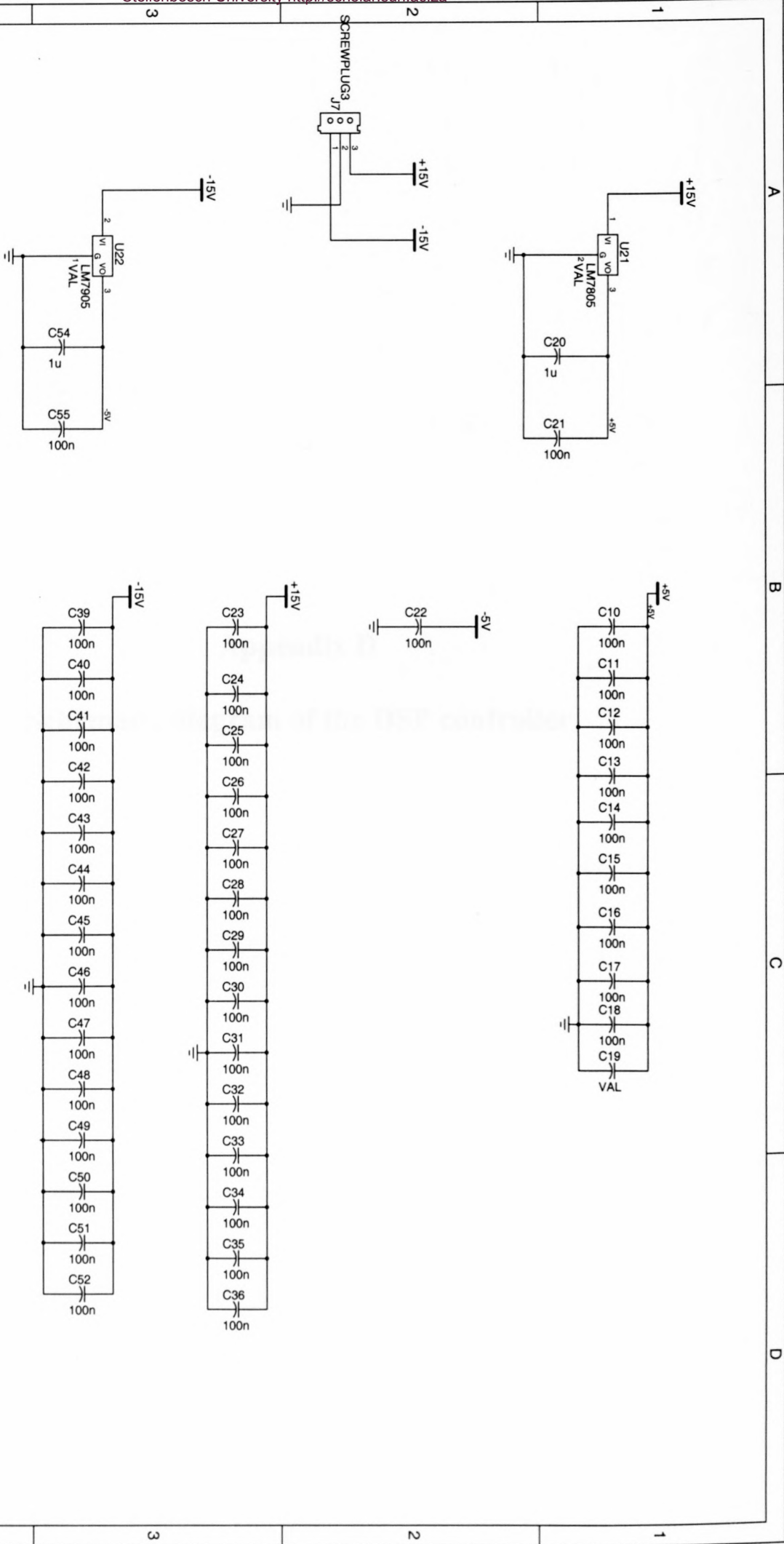
4



Title Measurement and Position Estimation		
Size A3	Number	Rev
Date	Drawn by	
Filename	Sheet	1 of 3



Title Measurement and Position Estimation		
Size A3	Number	Rev
Date	Drawn by	
Filename	Sheet 2 of 3	



Title
Measurement and Position Estimation

Size
A3

Number

Rev

Date

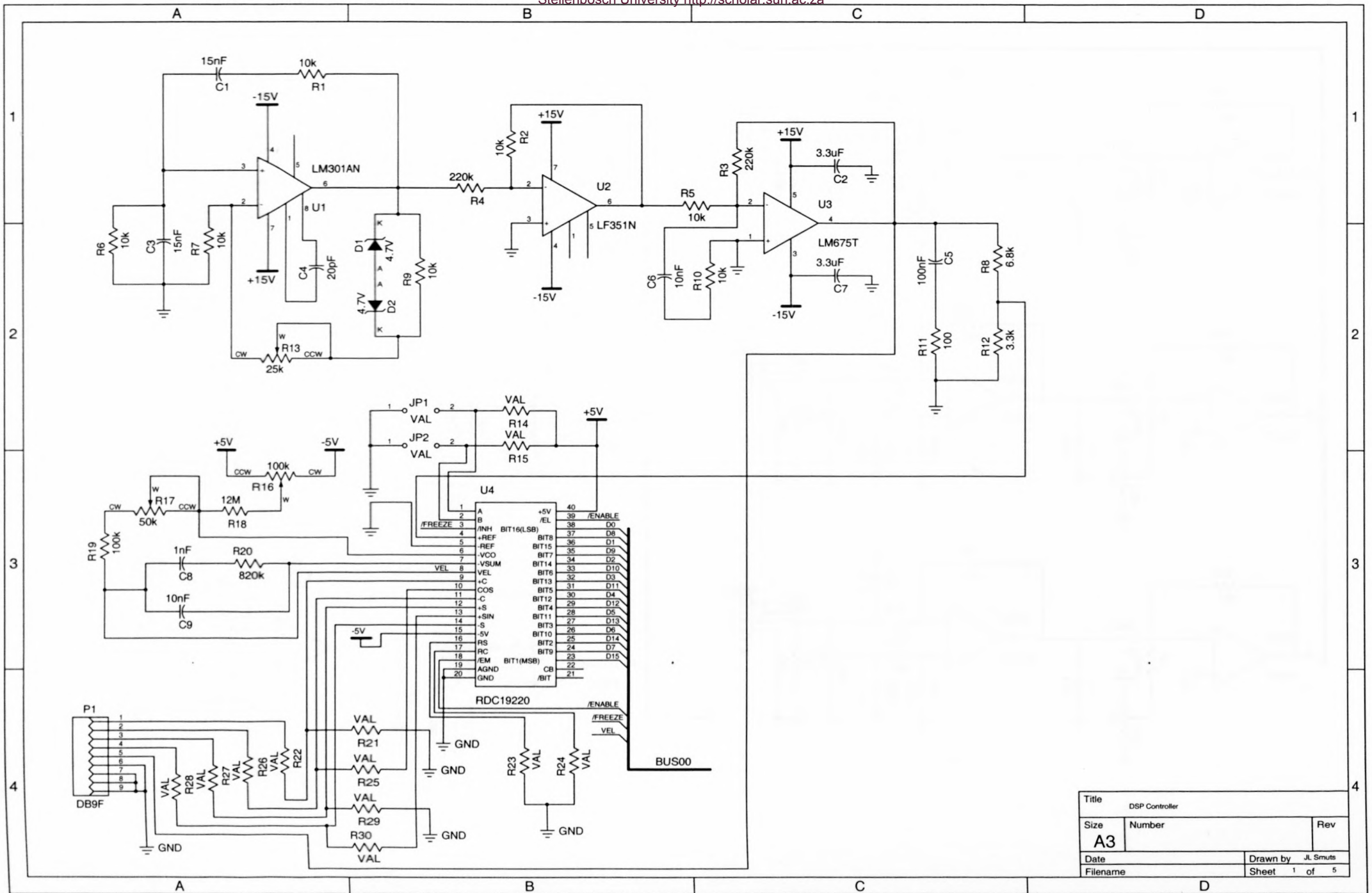
Filename

Drawn by

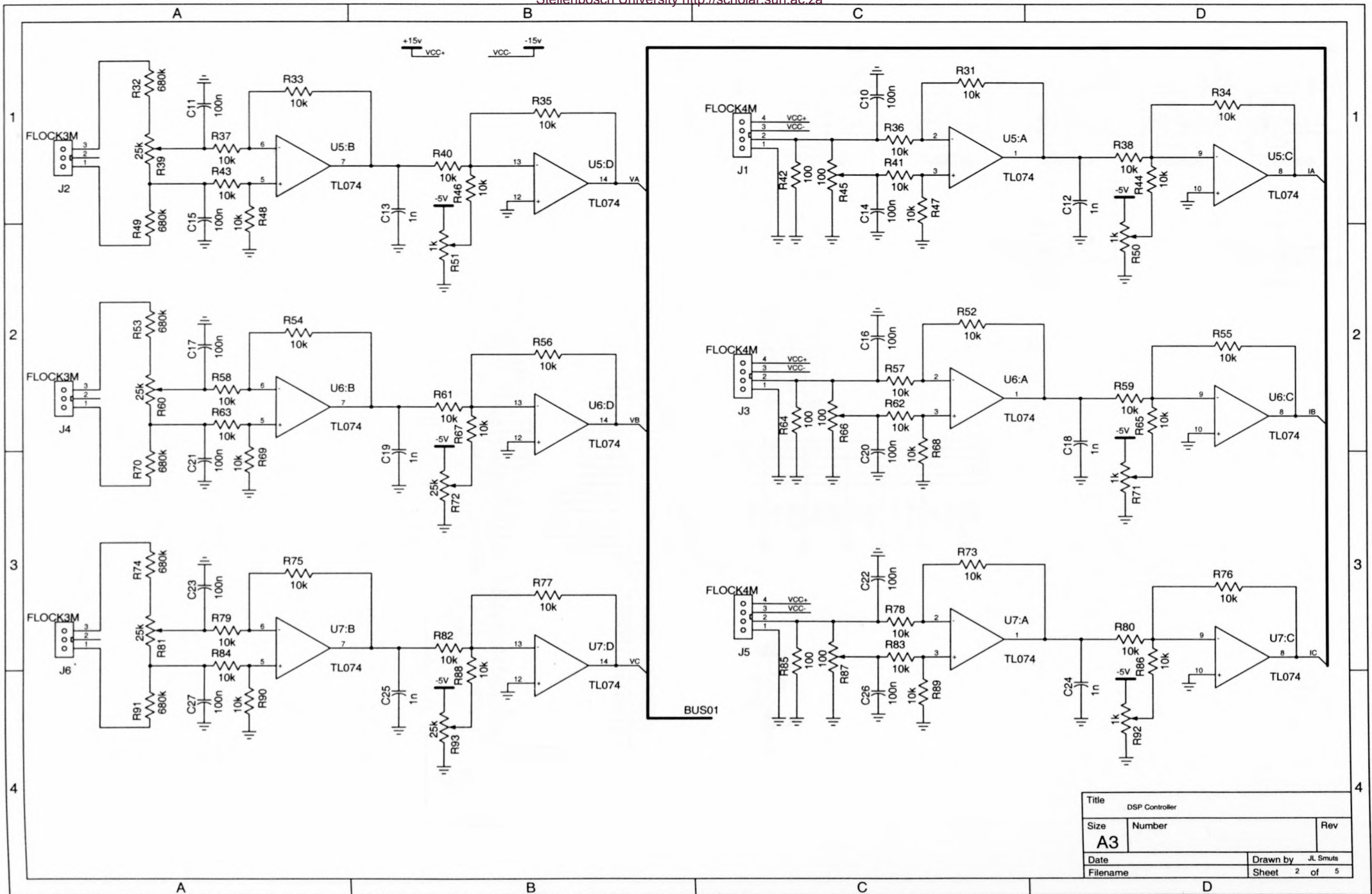
Sheet 3 of 3

Appendix D

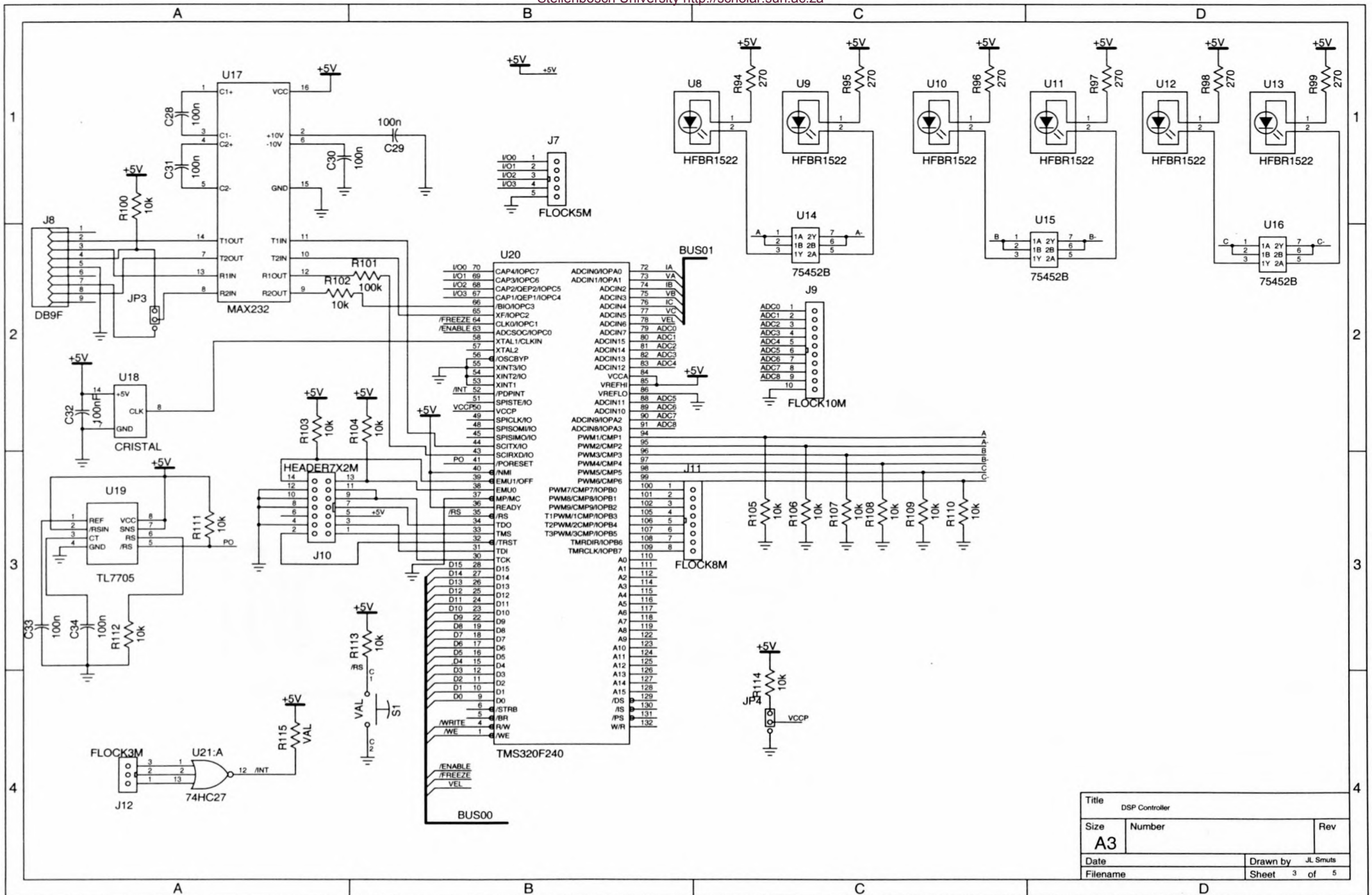
Schematic diagram of the DSP controller



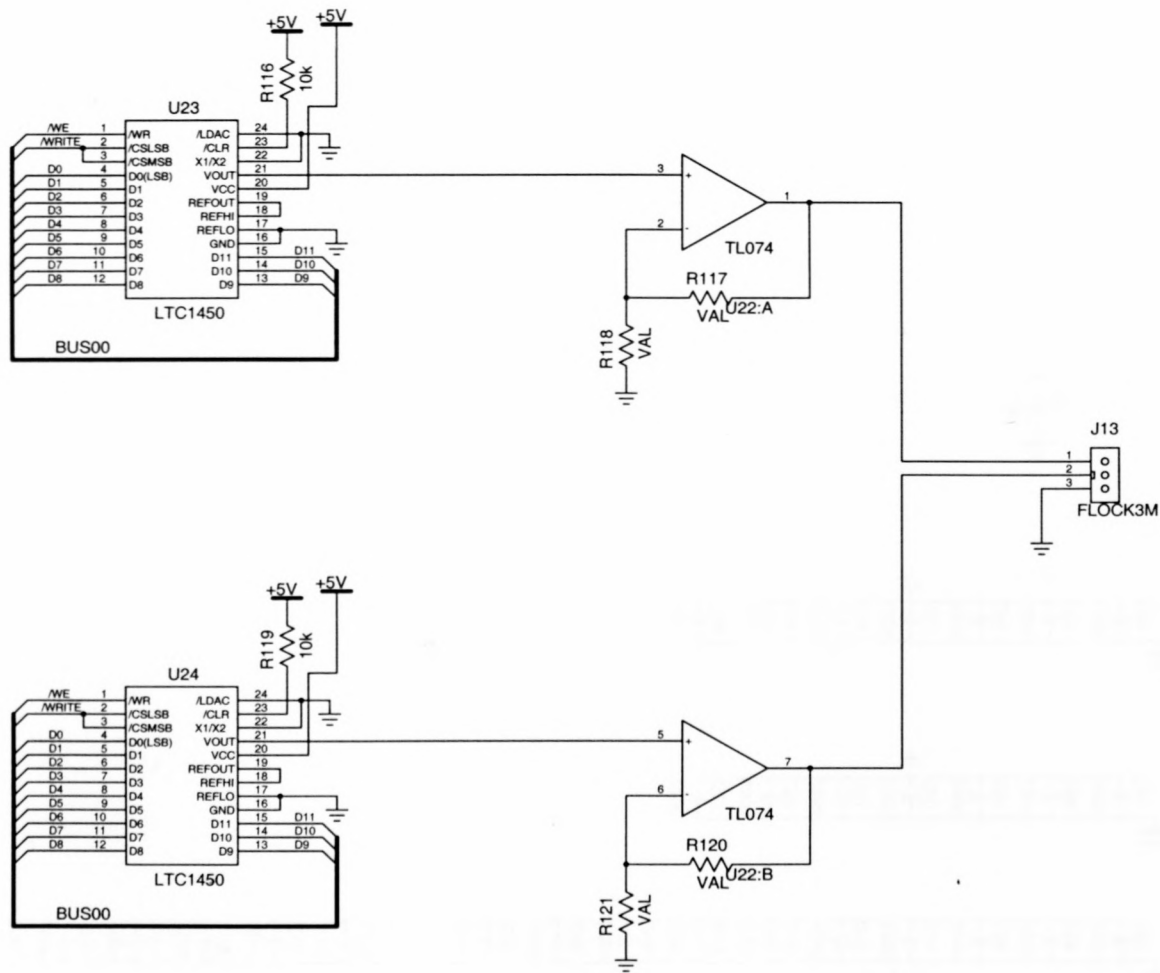
Title DSP Controller		
Size A3	Number	Rev
Date	Drawn by JL Smuts	
Filename	Sheet	1 of 5



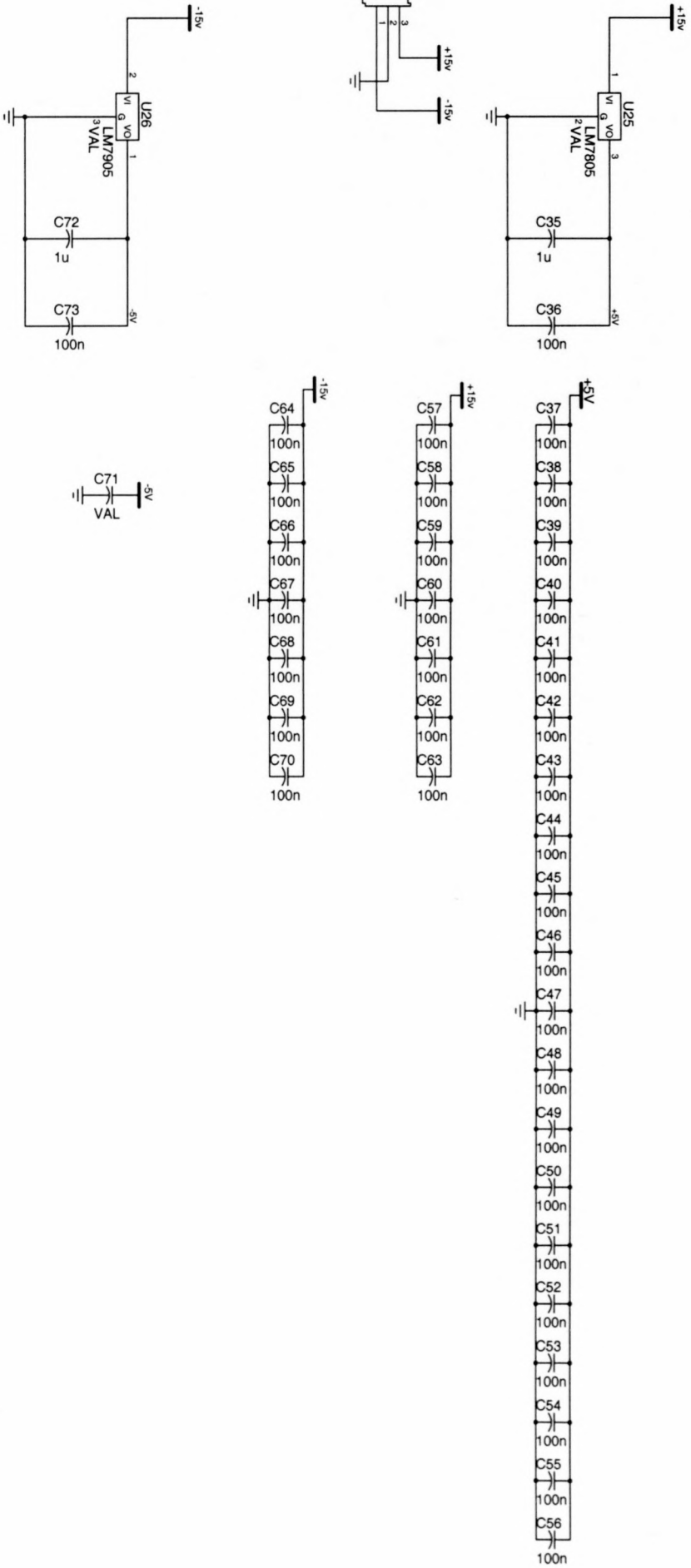
Title	DSP Controller		
Size	Number	Rev	
A3			
Date	Drawn by		JL Smuts
Filename	Sheet		2 of 5



Title DSP Controller			
Size A3	Number		Rev
Date		Drawn by	JL Smuts
Filename		Sheet 3	of 5



Title DSP Controller		
Size A3	Number	Rev
Date	Drawn by JL Smuts	
Filename	Sheet 4 of 5	



Title		DSP Controller	
Size	Number	Rev	
A3			
Date	Drawn by J. Smuts		
Filename	Sheet	5	of 5



smuts_critical_2001

1871
1872
1873

1874
1875
1876

1877
1878
1879
1880
1881
1882
1883
1884
1885
1886
1887
1888
1889
1890
1891
1892
1893
1894
1895
1896
1897
1898
1899
1900